Dual-comb spectroscopy with high coherence and high repetition rate

Dissertation zur Erlangung des Doktorgrades an der
Fakultät für Mathematik, Informatik und
Naturwissenschaften Fachbereich Physik der
Universität Hamburg

vorgelegt von

Thibault Voumard

Hamburg

2023

Declaration on oath

I hereby declare in lieu of oath that I have written this dissertation myself and that I have not used any auxiliary materials or sources other than those indicated.

Hamburg, 21.10.2023

Abstract

With the technological advent of optical frequency combs providing low-noise, well-defined and equidistantly spaced spectral references over a broad bandwidth, unprecedented opportunities for optical precision metrology arose. One elegant spectroscopic technique combines two optical frequency combs to achieve scan-less spectroscopy via massively multiplexed heterodyning. This technology, aptly named dual-frequency comb spectroscopy, relies on the mixing of a probing comb with a second comb of slightly different repetition rate for the down-conversion of an optical signature to the radio frequency domain. Attractive characteristics of dual-comb spectroscopy are comb-based precision and accuracy, high signal-to-noise ratio, broadband operation, fast acquisition times and absence of moving parts. One of the key challenges in dual-comb spectroscopy is to establish coherence between the two optical frequency combs over time scales exceeding the measurement times. Systems with high mutual coherence in combination with high repetition rate lasers create new opportunities for high bandwidth, fast spectroscopy at high optical resolution.

This thesis focuses on the demonstration of the potency of high repetition rate, high mutual coherence dual-comb spectrometers through multiple experiments. The high coherence of a 1 GHz dual-electro-optic comb spectrometer is used to demonstrate mapping and compression of optical spectra by 8 orders of magnitude from the hundreds of THz to the kHz range and below. Leveraging this compression from optical to acoustic frequencies, we show the first demonstration of photo-acoustic dual-comb spectroscopy, which combines the assets of broadband dual-comb spectroscopy with the high sensitivity of a photo-acoustic detection scheme. The technique can operate background-free in the entire electromagnetic spectrum, and weak absorption features of acetylene are rapidly and precisely sampled as an example.

Secondly, pushing the use of the system's high mutual coherence even further, real-time dual-comb hyperspectral imaging is realized based on a fast infrared detector array, providing high spectral and spatial resolution hyperspectral movies of a sample. A neural network is trained to achieve real-time treatment of the 16'384 pixels' data recorded at kHz rate based on 30 spectral channels, providing gas concentration imaging with a 10 Hz refresh rate.

To overcome the bandwidth limitations inherent to electro-optic combs, a dual-comb spectrometer based on 1 GHz Erbium oscillators is built. High mutual coherence between the combs on the seconds scale is established via a fully

digital locking scheme implemented in field-programmable gate arrays. The potential for the system to provide simultaneously fast and broadband measurements is demonstrated by performing water vapor spectroscopy around 1375 nm, as well as, by acquiring narrow gas absorption features across 0.6 THz in only 5 μs.

Using this spectrometer, a new calibration technique for astronomical spectrographs is demonstrated. By performing dual-comb spectroscopy of a Fabry-Pérot calibrator, the cavity's spectrum can be measured and linked to an atomic time standard with comb precision. The calibration lines resulting from the filtering of a white-light source by the cavity can then be linked back to the atomic time standard, providing properly conditioned, absolutely known calibration markers for astronomical spectrographs. This novel technique importantly provides astronomical spectrograph calibration based on lasers with repetition rates in the tens of MHz to a few GHz, circumventing the need for so-called astrocombs with repetition rates in the tens of GHz and their associated challenging operation.

Finally, to fully leverage the potential of high repetition rate, high mutual coherence dual-comb spectrometers, a software for simulating and optimizing supercontinuum generation from mixed and cascaded nonlinearities is presented. Via this software, extension paths of dual-comb spectroscopy to e.g. the mid-infrared for molecular absorption fingerprint spectroscopy or to the astronomy-critical visible and ultraviolet regions can be investigated and designed. The software is an open-source python package called *pychi* and simulates the propagation of short pulses in media exhibiting quadratic, cubic, mixed and cascaded nonlinearities. A dedicated solver is developed for fast computational times, as well as, an anti-aliasing technique preventing spurious spectral contamination from the finite bandwidth of the simulation. The simulations are shown to quantitatively agree with experimental results, enabling the use of the software not only for crystal and fiber-based simulations, but importantly in highly nonlinear chip-integrated waveguides.

Zusammenfassung

Mit dem technologischen Aufkommen optischer Frequenzkämme, die geringes Rauschen, gut definierte und gleichmäßig beabstandete spektrale Referenzen über eine breite Bandbreite bieten, eröffnen sich beispiellose Möglichkeiten für die optische Präzisionsmetrologie. Eine elegante Präzisionsspektroskopietechnik kombiniert zwei optische Frequenzkämme, um über massiv gemultiplexte Heterodyne Detektion eine Spektroskopietechnik frei von beweglichen Bauteilen zu ermöglichen. Diese Technologie, die passenderweise als Zwei-Kamm-Spektroskopie bezeichnet wird, basiert auf der Mischung eines Referenzkamms mit einem zweiten Kamm geringfügig unterschiedlicher Repetitionsrate zur Herunterkonvertierung eines optischen Signals in den Radiofrequenzbereich. Attraktive Merkmale der Zwei-Kamm-Spektroskopie sind Präzision, ein hohes Signal-Rausch-Verhältnis, extreme breitbandiger Betrieb, schnelle Signal Erfassung ohne bewegliche mechanische Bauteile. Eine der zentralen Herausforderungen in der Zwei-Kamm-Spektroskopie besteht darin, die Kohärenz zwischen den beiden optischen Frequenzkämmen für den gesamten Messzeitraum zu gewährleisten. Systeme mit hoher gegenseitiger Kohärenz in Kombination mit Lasern hoher Repetitionsrate schaffen neue Möglichkeiten für eine Hochband-breiten- und schnelle Spektroskopie bei hoher optischer Auflösung.

Diese Arbeit konzentriert sich auf die Demonstration der Leistungsfähigkeit von Zwei-Kamm-Spektrometern mit hoher Repetitionsrate und hoher Kohärenz durch mehrere Experimente. Die hohe Kohärenz eines 1 GHz elektro-optischen Zwei-Kamm-Spektrometers wird genutzt, um die Abbildung und Kompression optischer Spektren um 8 Größenordnungen von Hunderten von THz bis in den kHz-Bereich und darunter zu demonstrieren. Durch die Nutzung dieser Kompression von optischen hin zu akustischen Frequenzen zeigen wir die erste Demonstration der fotoakustischen Zwei-Kamm-Spektroskopie, die die Vorteile der breitbandigen Zwei-Kamm-Spektroskopie mit der hohen Empfindlichkeit eines fotoakustischen Detektionsschemas kombiniert. Die Technik kann im gesamten elektromagnetischen Spektrum untergrundfrei arbeiten, und schwache Absorptionsmerkmale von Acetylen werden beispielhaft schnell und präzise erfasst.

Weiterhin wird durch die Ausnutzung der hohen gegenseitigen Kohärenz des Systems die Echtzeit-Zwei-Kamm-Hyperspektralbildgebung auf der Grundlage eines schnellen Infrarot-Detektorarrays realisiert. Ein neuronales Netzwerk wird darauf trainiert, die in kHz-Rate aufgenommenen Daten von 16'384 Pixeln

basierend auf 30 spektralen Kanälen in Echtzeit zu verarbeiten und Gaskonzentrationsbildgebung mit einer Bildwiederholrate von 10 Hz zu ermöglichen.

Um die Bandbreitenbeschränkungen von elektrooptischen Kämmen zu überwinden, wird ein Zwei-Kamm-Spektrometer auf der Grundlage von 1 GHz Erbium-Oszillatoren gebaut. Die hohe gegenseitige Kohärenz zwischen den Kämmen im Sekundenbereich wird durch ein vollständig digitales Regelsystem auf Basis von Field-Programmable Gate Arrays hergestellt. Das Potenzial des Systems, gleichzeitig schnelle und breitbandige Messungen durchzuführen, wird durch die Durchführung von Wasserdampfspektroskopie bei 1375 nm sowie durch die Erfassung schmaler Gasabsorptionsmerkmale über 0.6 THz in nur 5 μs demonstriert.

In einem weiteren Experiment, wird mit diesem Spektrometer eine neue Kalibrationstechnik für astronomische Spektrografen demonstriert. Durch die Durchführung von Zwei-Kamm-Spektroskopie eines Fabry-Pérot-Frequenzstandards, wird dieses direkt mit dem hochpräzisen optischen Frequenzkamm verknüpft. Die Kalibrationslinien, die durch die Filterung einer Weißlichtquelle durch die Kavität entstehen, können dann auf die atomare Zeitskala zurückgeführt werden und liefern optimal konditionierte, absolut bekannte Kalibrationsmarker für astronomische Spektrografen. Diese neue Technik ermöglicht die Kalibrations von astronomischen Spektrografen basierend auf Lasern mit Repetitionsraten im Bereich von zehn MHz bis zu einigen GHz und umgeht so die Notwendigkeit sogenannter Astrocombs mit Wiederholungsraten im Bereich oberhalb von zehn GHz und deren damit verbundene anspruchsvolle Bedienung.

Schließlich, um das Potenzial von Zwei-Kamm-Spektrometern mit hoher Wiederholfrequenz und hoher Kohärenz voll auszuschöpfen, wird eine Software zur Simulation und Optimierung der Superkontinuum-Erzeugung aus gemischten und kaskadierten Nichtlinearitäten präsentiert. Mit dieser Software können spektrale Erweiterungen der Zwei-Kamm-Spektroskopie z.B. in den mittleren Infrarotbereich für die molekulare Absorptions-Fingerprint-Spektroskopie oder in die, für die Astronomie wichtigen, sichtbaren und ultravioletten Bereiche untersucht und gestaltet werden. Die Software ist ein Open-Source-Python-Paket namens *pychi* und simuliert die Propagation kurzer Pulse in Medien mit quadratischen, kubischen, gemischten und kaskadierten Nichtlinearitäten. Ein dedizierter Solver wurde für schnelle Berechnungszeiten entwickelt, sowie eine Anti-Aliasing Technik, die parasitäre spektrale Komponenten verhindert, die durch die endliche Bandbreit der Simulation verursacht werden können. Die Simulationen stimmen quantitativ mit experimentellen Ergebnissen überein und ermöglichen die Verwendung der Software nicht nur für Kristall- und Faser-basierte Simulationen, sondern auch für hoch-gradig nichtlineare, chip-integrierte Wellenleiter.

This abstract was translated from the English abstract with the help of ChatGPT.

First author publications

1. **Photo-acoustic dual-frequency comb spectroscopy**
   Thibault Wildi [†], *Thibault Voumard* [†], *Victor Brasch, Gürkan Yilmaz, and Tobias Herr*
   Nature Communications volume 11, Article number: 4164, Published 20 August 2020
   [†] These authors contributed equally.

2. **AI-enabled real-time dual-comb molecular fingerprint imaging**
   Thibault Voumard [†], *Thibault Wildi* [†], *Victor Brasch, Raúl Gutiérrez Álvarez, Germán Vergara Ogando, and Tobias Herr*
   Optics Letters Vol. 45, Issue 24, pp. 6583-6586, Published 3 December 2020
   [†] These authors contributed equally.

3. **1-GHz dual-comb spectrometer with high mutual coherence for fast and broadband measurements**
   Thibault Voumard, John Darvill, Thibault Wildi, Markus Ludwig, Christian Mohr, Ingmar Hartl, and Tobias Herr
   Optics Letters Vol. 47, Issue 6, pp. 1379-1382, Published 7 March 2022

4. **Simulating supercontinua from mixed and cascaded nonlinearities**
   Thibault Voumard, Markus Ludwig, Thibault Wildi, Furkan Ayhan, Victor Brasch, Luis Guillermo Villanueva, and Tobias Herr
   APL Photonics 8, 036114, Published 28 March 2023

5. **Dual-frequency comb assisted astronomical spectrograph calibrator**
   Thibault Voumard, Thibault Wildi, Markus Ludwig, François Bouchy, and Tobias Herr
   Manuscript in preparation

Publications as contributing author

1. **Visible blue-to-red 10 GHz frequency comb via on-chip triple-sum-frequency generation**
   Ewelina Obrzud, Victor Brasch, Thibault Voumard, Anton Stroganov, Michael Geiselmann, François Wildi, Francesco Pepe, Steve Lecomte, and Tobias Herr
   Optics Letters Vol. 44, Issue 21, pp. 5290-5293, Published 28 October 2019

2. **Dual-comb cavity-mode width and shift spectroscopy**
   Dominik Charczun, Akiko Nishiyama, Grzegorz Kowzan, Agata Cygan, Thibault Voumard, Thibault Wildi, Tobias Herr, Victor Brasch, Daniel Lisak, and Piotr Masłowski
   Measurement Vol. 188, 110519, Published November 2021

3. **Dual-comb cavity ring-down spectroscopy**
   Daniel Lisak, Dominik Charczun, Akiko Nishiyama, Thibault Voumard, Thibault Wildi, Grzegorz Kowzan, Victor Brasch, Tobias Herr, Adam J. Fleisher, Joseph T. Hodges, Roman Ciuryło, Agata Cygan, and Piotr Masłowski
   Scientific Reports volume 12, Article number: 2377, Published 11 February 2022

4. **Dissipative Kerr solitons in integrated Fabry–Perot microresonators**
   Thibault Wildi, Mahmoud A. Gaafar, Thibault Voumard, Markus Ludwig, and Tobias Herr
   Optica Vol. 10, Issue 6, pp. 650-656, Published 23 May 2023

5. **Ultraviolet astronomical spectrograph calibration with laser frequency combs from nanophotonic waveguides**
   Markus Ludwig, Furkan Ayhan, Tobias M. Schmidt, Thibault Wildi, Thibault Voumard, Roman Blum, Zhichao Ye, Fuchuan Lei, François Wildi, Francesco Pepe, Mahmoud A. Gaafar, Ewelina Obrzud, Davide Grassani, François Moreau, Bruno Chazelas, Rico Sottile, Victor Torres-Company, Victor

Brasch, Luis G.Villanueva, François Bouchy, and Tobias Herr
Preprint on arXiv, 23 June 2023

6. **Sideband injection locking in microresonator frequency combs**
Thibault Wildi, Alexander Ulanov, Nicolas Englebert, <u>Thibault Voumard</u>, and Tobias Herr
Preprint on arXiv, 19 October 2023

List of conference presentations

1. **Dual-frequency comb hyperspectral imaging by massively parallelized infrared detection and machine learning**
   Thibault Voumard, Thibault Wildi, Victor Brasch, Raul Gutierrez Alvarez, Germán Vergara Ogando, and Tobias Herr
   Optics and Photonics for Sensing the Environment 2020, Vancouver, British Columbia, Canada
   Nominated as finalist for the OSA Student Paper Award

2. **Dual-comb spectroscopy with photoacoustic detection**
   Thibault Wildi, Thibault Voumard, Victor Brasch, Gürkan Yilmaz, and Tobias Herr
   Optics and Photonics for Sensing the Environment 2020, Vancouver, British Columbia, Canada

3. **Artificial intelligence for real-time dual-frequency comb hyperspectral imaging** *Thibault Voumard, Thibault Wildi, Victor Brasch, Raul Gutierrez Alvarez, German Vergara Ogando, and Tobias Herr*
   CLEO: Science and Innovations 2020, Washington, DC, United States

4. **Dual-comb photoacoustic spectroscopy**
   Thibault Wildi, Thibault Voumard, Victor Brasch, Gürkan Yilmaz, and Tobias Herr
   CLEO: Science and Innovations 2020, Washington, DC, United States

5. **Dual-comb hyperspectral imaging with a high-framerate infrared detector array**
   Thibault Voumard, Thibault Wildi, Victor Brasch, Raul Gutierrez Alvarez, German Vergara Ogando, and Tobias Herr
   CLEO: Science and Innovations 2020, Washington, DC, United States

6. **Efficient simulation of supercontinua from cubic, quadratic and cascaded nonlinearities**
   Thibault Voumard, Markus Ludwig, Thibault Wildi, and Tobias Herr
   Conference on Lasers and Electro-Optics/Pacific Rim 2022, Sapporo, Japan

7. **1 GHz Erbium-doped mode-locked laser dual-frequency comb spectrometer**
   Thibault Voumard, John Darvill, Thibault Wildi, Markus Ludwig, Christian Mohr, Ingmar Hartl, and Tobias Herr
   CLEO: Applications and Technology 2022, San Jose, CA, United States

8. **Dual-comb spectroscopy for astronomical spectrograph calibration**
   Thibault Voumard, Markus Ludwig, Thibault Wildi, Bruno Chazelas, François Wildi, François Bouchy, Francesco Pepe, and Tobias Herr
   CLEO: Science and Innovations 2022, San Jose, CA, United States

9. **Efficient simulation of supercontinua from mixed and cascaded nonlinearities**
   Thibault Voumard, Markus Ludwig, Thibault Wildi, and Tobias Herr
   CLEO: Science and Innovations 2023, San Jose, CA, United States

Acknowledgements

I express my deepest gratitude to my supervisor Prof. Dr. Tobias Herr for his continued help, availability and everlasting optimism. Your guidance and unlimited amount of ideas proved invaluable all along my PhD, while your extensive scientific knowledge and perspicacity made conversations we had enriching. I am glad I took this train to the Big North with you.

Many thanks go to my colleagues and friends Thibault, Markus, Felix, Mahmoud, Weichen, Alexander, Bastian, Roland, Giulio, Fabian and Miguel, Tobi and Erwin. You have all been a source of inspiration and a pleasure to work with. I have fond memories of lunch and coffee times, as well as, some after-conference expeditions.

I want to deeply thank Thibault for all the time we spent together and for "levitating the ceiling" of science with me. I enjoyed being mistaken for you and inversely, and playing on this from time to time. Your company in the office and the lab, but also in climbing, camping and more has always been a pleasure. As we say, GL&HF for the rest of your PhD.

Markus, I want to thank you for showing me that a little bit of curiosity can go a very long way. I appreciated sharing my thoughts with you and listening to yours. I am glad I found someone to enjoy the roller coasters of DOM along with (as well as candies).

My parents have my eternal recognition for their unalterable support, as do my brother and sister. I also want to thank my friends Antoine F., Benjamin, Jonas, Antonin, Romain, Adrian, Nicolò, Gabriel, Jona, Anne-Do, Charlène, Antoine G., Goratz, Anna and Benoît for existing between other specific things. I am looking forward to come back to all of you.

Finally, I can not express how much I thank Mathilde for her love, trust and support throughout all these years. You did not hesitate to join me in this adventure and it has been wonderful to live this life here with you. I can not wait to see what the future holds for us, as I know we will build it together.

Thibault Voumard   Autumn 2023

Contents

Chapter 1

Dual-frequency comb spectroscopy

Optical spectroscopy underpins countless applications of modern research by providing access to the spectral information of a sample [1, 2, 3]. The development of optical frequency combs, whose spectra consists of lines spaced equidistantly in frequency, provided unprecedented opportunities for radio frequency control of optical waveforms [4, 5, 6, 7, 8, 9]. Their introduction in optical spectroscopy led to the development of the dual-frequency comb spectrometer as an elegant, moving-part free alternative to Fourier transform spectrometers permitting fast and robust operation at high precision and accuracy [10, 11, 12, 13]. Fundamental to dual-comb spectroscopy, high mutual coherence between optical frequency combs of high repetition rate enables broadband operation at both high and low acquisition rates. This thesis focuses on the development and applications of high repetition rate, high mutual coherence dual-frequency comb spectrometers and their distinct advantages regarding acquisition rate and broadband spectral coverage through applications from molecular spectroscopy to astronomical spectrograph calibration.

We start here with the technical aspects underlying dual-frequency comb spectroscopy. At first, optical frequency combs and their defining features are discussed. Building upon this, dual-frequency comb spectroscopy is presented. Key characteristics of dual-comb spectrometers are discussed in detail, as is the prominent role of high mutual coherence between the frequency combs, as well as, the advantages brought by using high repetition rate frequency combs. Finally, the author's publications are presented and discussed in the context of the immediate research field and beyond.

1.1 Optical frequency combs and optical spectroscopy

Optical spectroscopy is the study of the electromagnetic spectra resulting from the interaction of light and matter. It represents a fundamental tool in the exploration of the composition and structure of matter at various levels, providing insights to the macroscopic, molecular, electronic or atomic structure of a sample. In its basic form, a sample to be studied is probed by a light source covering a certain range of the electromagnetic spectrum. The radiations resulting from this photonic excitation are recorded by a device capable of discriminating different spectral regions, yielding a frequency- (or wavelength-) dependent quantity related to the properties of the sample under study.

Optical spectroscopy enables an extensive variety of technologies, measurements and characterizations [1, 2, 3]. For instance, astronomy leverages precision spectroscopy for the study of stellar spectra, permitting the detection of exoplanets through the radial velocity method, as well as, the monitoring of the cosmological constant [14]. The fields of chemistry and material science depend on spectroscopy to unveil the molecular composition of certain gases, liquids and solids. Optical spectrometers are far from confined to laboratory environment, as they find wide use in industry and field applications, enabling process control, quality measurements and environmental monitoring [15]. Spectroscopy also finds numerous applications in medical imaging and medicine in general, permitting non-invasive, advanced medical diagnosis even through tissues [16]. Historically, spectroscopy has played a vital role in the development of quantum mechanics through the study of the absorption lines of the Hydrogen atom and the well-known ultraviolet catastrophe. As an enabling measurement technique, optical spectroscopy represents in and of itself an entire area of research in modern optics.

In recent years, so-called optical frequency combs have revolutionized the field of optical spectroscopy by providing a coherent link from the radio frequency domain to the optical domain, permitting unprecedented control of optical waveforms. The spectra of optical frequency combs, consisting of bright optical lines equidistantly spaced in frequency (see Fig 1.1), add perfect spectral rulers to the experimentalist's toolbox and permit frequency measurements traceable to SI standards. In particular, they enabled e.g. optical clocks, highly nonlinear optics, waveform synthesis, radio frequency control of optical waveforms, as well as, breakthroughs in the spectral coverage, sensitivity, precision and accuracy of optical spectrometers [4, 5, 6, 7, 8, 9, 17].

1.1.1 Generation of frequency combs

Optical frequency combs can be obtained from laser sources leveraging different physical mechanisms, including:

The optical spectrum of *mode-locked lasers* are frequency combs relying on an intra-cavity saturable absorber to establish low-noise, pulsed operation of a
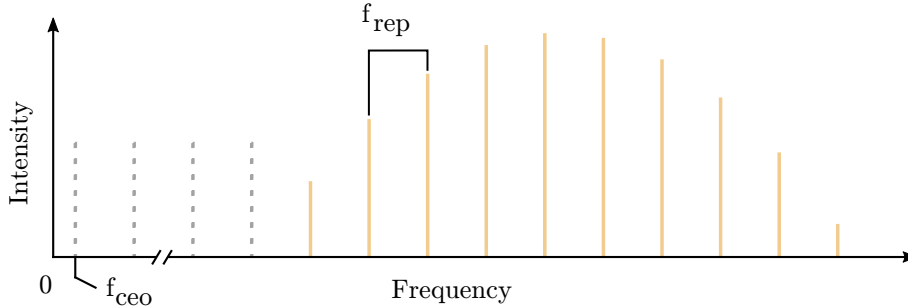
Figure 1.1: Illustration of an optical frequency comb. Its spectrum consists of equidistant lines spaced by its repetition rate f_{rep}, while the offset from zero frequency is given by f_{ceo}.

laser [5, 4]. They typically operate over a range of repetition rates covering a few kHz to a GHz. Robust mode-locked lasers using different gain materials are commercially available, notably with mature and cost effective options in the telecommunication region around 1550 nm.

Electro-optic frequency combs rely on phase- and intensity-modulation of a continuous wave laser to generate equidistantly spaced spectral side bands [18]. Such optical frequency combs are directly driven by radio frequency signals for their generation, rendering their use convenient and flexible. They can operate with repetition rates up to tens of GHz, however have typically low peak power, which hinders their spectral extension to a broadband coverage.

The emerging *microresonator-based frequency combs* represent novel opportunities to generate optical frequency combs with repetition rates up to the THz range [19, 20]. They rely on the formation of soliton-like pulses inside chip-integrated resonators, stemming from the balance between intra-cavity dispersion and nonlinearity. These sources however are still challenging to operate in a reliable, continuous manner.

The electric field of a frequency comb can be written as [6, 7, 8]

$$E(t) = \Re \left[\sum_n A_n e^{2\pi i (n f_{rep} + f_{ceo}) t} \right], \tag{1.1}$$

where f_{rep} represents the spacing between adjacent comb lines, n runs over all positive integers, f_{ceo} is the offset of the $n = 0$ comb line from DC and A_n is the complex spectral envelope of the comb. f_{rep} is the repetition rate of the oscillator, i.e. the number of light pulses emitted per second. The offset f_{ceo} equivalently corresponds to the time derivative of the successive phase slippage between the optical carrier of pulses and their temporal envelope, which led to its common denomination being the 'carrier-envelope offset frequency'.

A perfect frequency comb thus exhibits light only at well defined, equidistantly spaced frequencies $\nu_n = n f_{rep} + f_{ceo}$, each with a delta-peak lineshape. Crucially, while ν_n are optical frequencies, f_{rep} and f_{ceo} are radio frequencies
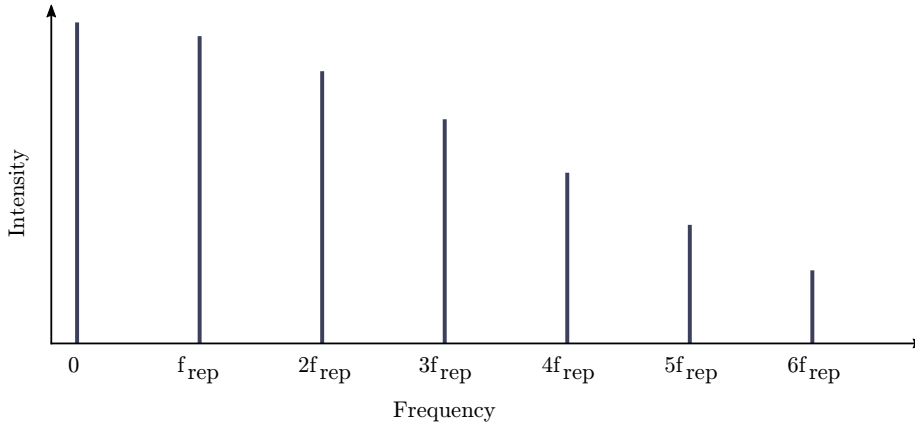
Figure 1.2: Radio frequency spectrum resulting from the self-heterodyning of a frequency comb. The repetition rate of the comb can be easily detected and monitored, providing a coherent optical to radio frequency link.

on the order of 1 kHz to tens of GHz, with $|f_{ceo}| \leq f_{rep}/2$. Actuating these two parameters in the radio frequency domain thus unambiguously acts on the optical lines of the comb and inversely via Eq. 1.1, permitting the control of an optical waveform with radio frequency signals and providing a direct and coherent bridge from radio frequencies to optical frequencies.

1.1.2 Radio-to-optical frequency link

When a frequency comb illuminates a photodetector, the resulting photocurrent is proportional to

$$i_{LFC}(t) \propto |E(t)|^2 = \sum_n \sum_m A_n A_{n-m}^* e^{2\pi i m f_{rep} t}, \tag{1.2}$$

corresponding to a radio frequency comb with a line spacing of f_{rep}, as depicted in Fig. 1.2. The repetition rate of a frequency comb is easily measured by tracking any of these radio frequency beatnotes. Control of the repetition rate can then be achieved e.g. by implementation of feedback loops via standard electronics, which for mode-locked lasers typically actuate the laser cavity length via piezo-electric components. However, this optical-to-radio frequency mapping is ambiguous, as distinct optical lines will be down-converted to the same frequency (take m fixed and n varying). This prevents a direct reconstruction of the optical lines' amplitudes from the radio signal.

Eq. 1.2 not containing f_{ceo} also demonstrates that more involved techniques need to be employed for the detection of the carrier envelope offset frequency. One of these techniques is the so-called f-2f interferometry, which relies on the detection of a beatnote between a frequency comb and a frequency doubled part of its spectrum [21, 22]. The spectrum of the frequency comb is first extended

4

to an octave via supercontinuum generation in a cubic nonlinear medium. The low frequency part of the spectrum is then frequency doubled using a quadratic nonlinear medium, often a periodically poled crystal. This frequency doubling results in light with a carrier envelope offset frequency twice that of the original comb. It overlaps in frequency with the high frequency part of the broadened original spectrum. When shining the combined light on a photodetector, one gets (keeping only the mixed terms)

$$i_{f-2f}(t) \propto \sum_n \sum_m A_n e^{2\pi i (n f_{rep} + f_{ceo})t} B_m^* e^{-2\pi i (m f_{rep} + 2 f_{ceo})t}, \qquad (1.3)$$

where B is the amplitude of the frequency doubled part of the spectrum. Looking at the $n = m$ part of this expression, one gets

$$i_{f-2f}(t)|_{n=m} = \sum_m A_m B_m^* e^{-2\pi i f_{ceo}t}, \qquad (1.4)$$

which oscillates at the frequency f_{ceo}. An f-2f interferometer consequently provides an elegant way to measure the offset frequency of an optical comb. The orders with $n \neq m$ provide additional access to the offset frequency, added or removed from multiples of the repetition rate. Similarly to the repetition rate, feedback loops can be implemented on standard electronics to control and stabilize the offset frequency. For mode-locked lasers, the pump current is often used as the actuator. Alternatively, intra-pulse difference frequency generation can be used to generate combs free of offset frequency, although this approach has its own associated challenges.

Achieving control of both the repetition rate and the offset frequency of a comb provides the experimenter with a set of controllable optical lines with known frequencies and establishes a direct link from radio to optical frequencies. Similarly, the reciprocal optical-to-radio frequency link enables the generation of low noise radio frequency signals and is the workhorse of optical clocks [23]. Importantly, the optical comb's repetition rate and offset frequency can be referenced to an SI frequency standard, permitting absolute spectroscopic measurements.

1.2   Dual-comb spectroscopy

Combining two optical frequency combs with different repetition rates elegantly emulates a scanning interferometer comparable to the well-known Fourier transform spectrometers [10, 11, 12, 13]. Being purely comb-based, this technique of dual-frequency comb spectroscopy benefits from the precision and accuracy offered by frequency combs and can easily be linked to an SI time standard for absolute calibration. The absence of moving parts opens the way to short acquisition times and robust operation, across a wide spectral span and with high optical resolution.
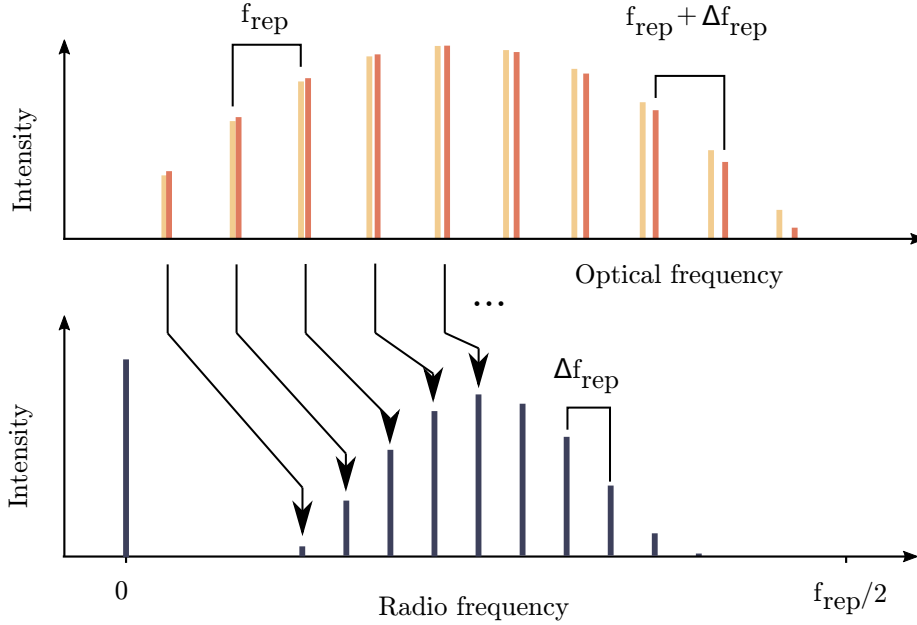
Figure 1.3: Multi-heterodyning of two optical frequency combs, resulting in down-conversion and compression of the optical information to the radio frequency domain.

1.2.1 Concept

When mixing two optical frequency combs on a photodetector, fully unambiguous down-conversion of the combs to the radio frequency domain can be achieved, providing the basis for dual-comb spectroscopy. If one denotes quantities akin to the second comb with a prime (i.e. E', with repetition rate f'_{rep} and offset frequency f'_{ceo}), the measured photocurrent will be

$$i_{DCS}(t) \propto |E(t) + E'(t)|^2 = |E(t)|^2 + |E'(t)|^2 + 2\Re\left[E^*(t)E'(t)\right]. \qquad (1.5)$$

Eq. 1.2 provides the form of the first two terms, yielding radio frequency combs with zero offset and repetition rates f_{rep} and f'_{rep} respectively. The mixed term takes the form

$$E^*(t)E'(t) = \sum_n \sum_m A_n^* A'_m e^{2\pi it(mf'_{rep} - nf_{rep} + f'_{ceo} - f_{ceo})}. \qquad (1.6)$$

Denoting $f'_{ceo} = f_{ceo} + \Delta f_{ceo}$ and $f'_{rep} = f_{rep} + \Delta f_{rep}$,

$$E^*(t)E'(t) = \sum_n \sum_m A_n^* A'_m e^{2\pi it(m\Delta f_{rep} + \Delta f_{ceo})} e^{2\pi it(m-n)f_{rep}}. \qquad (1.7)$$

Fundamental to dual-frequency comb spectroscopy, Eq. 1.7 shows that each

pair (m, n) of comb lines gets uniquely mapped to the heterodyne radio frequency

$$m\Delta f_{rep} + \Delta f_{ceo} + (m - n)f_{rep} \qquad (1.8)$$

with amplitude proportional to the product of the optical lines' amplitudes. Focusing first on the case where $m = n$, the photocurrent

$$i_{DCS}(t)|_{m=n} \propto \sum_n A_n^* A_n' e^{2\pi i t(n\Delta f_{rep} + \Delta f_{ceo})}, \qquad (1.9)$$

which is a frequency comb with repetition rate Δf_{rep} and offset frequency Δf_{ceo}, as exemplified in Fig. 1.3. As Δf_{rep} can be several orders of magnitude smaller than f_{rep}, the technique provides a coherent compression of the optical domain down to the radio frequency domain, resulting in a signal that can be captured with modern electronics. The compression ratio $f_{rep}/\Delta f_{rep}$ can be defined to give a measure of the system's capabilities to down-convert information from the optical domain to the radio frequency domain.

In the time domain, this radio frequency comb is an interferogram that typically consists of a center burst with a carrier frequency that is the weighted average of its spectral components, in analogy with the optical pulses of a mode-locked laser, as exemplified in Fig. 1.4.

Via Fourier transformation of the recorded photocurrent, the experimenter can retrieve the amplitudes $A_n^* A_n'$ of the radio frequency signal. To perform spectroscopy, the measurement is repeated with a sample to be studied in the beam path of the second comb. The sample will absorb and delay the comb depending on the optical frequency with a complex transfer function $S(f)$, leading to modified optical amplitudes $A_n' S(n f'_{rep} + f'_{ceo})$. In this case, the photocurrent is a radio frequency comb with accordingly modified amplitudes $A_n^* A_n' S(n f'_{rep} + f'_{ceo})$. By comparing the results of the two experiments, one recovers the optical transfer function $S(n f'_{rep} + f'_{ceo})$, i.e. the sample's spectroscopic properties.

To ensure a one-to-one mapping from optical to radio frequencies, certain criteria need to be fulfilled by the dual-comb spectrometer. Eq. 1.7 with $m > n$ reveals additional radio frequency combs, offset by $(m - n)f_{rep}$ from the lowest radio frequency comb. When $m < n$, the resulting comb is 'reflected' around multiples of f_{rep}, at frequencies $(n - m)f_{rep} - \Delta f_{ceo} - m\Delta f_{rep}$, as illustrated in Fig. 1.5. Two radio frequency combs are thus generated per f_{rep} interval and Δf_{rep} must be small enough to prevent overlap between these combs. For an optical bandwidth $\Delta\nu$ of the combs, the number of optical lines per comb is given by $N = \Delta\nu/f_{rep}$. From Eq. 1.7, each radio frequency comb also possesses N lines, mapped from the optical domain. The requirement

$$N\Delta f_{rep} \leq f_{rep}/2 \qquad (1.10)$$

ensures that these combs have a limited radio frequency bandwidth, thus giving the opportunity to avoid ambiguous frequency overlap. This equation is usually referred to as the Nyquist criterion and written in terms of the optical bandwidth
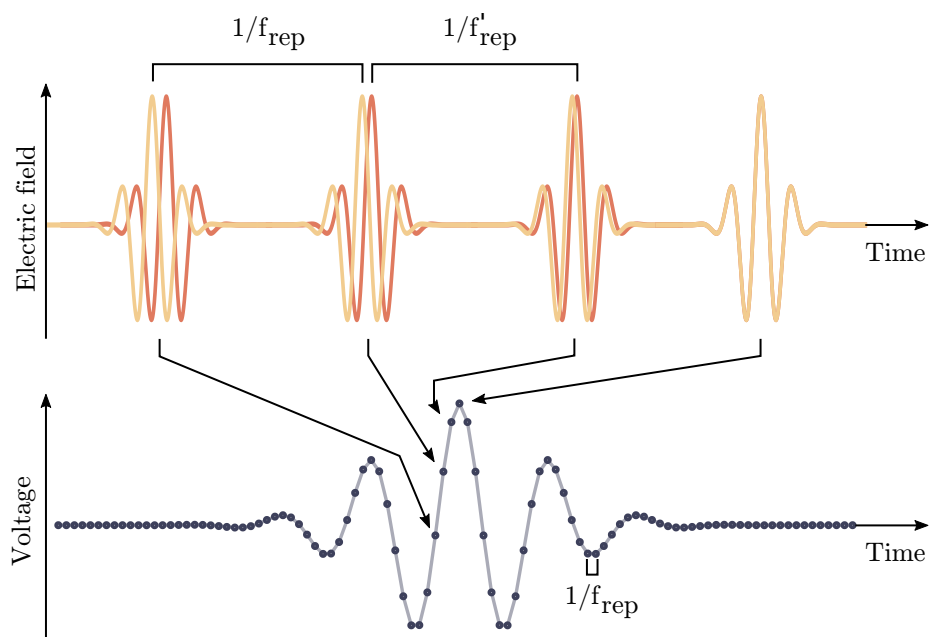
Figure 1.4: Time-domain picture of the multi-heterodyning of two optical frequency combs. As the combs' pulses scan through each other due to their slightly different repetition rate, a photodetector samples the corresponding interferogram.
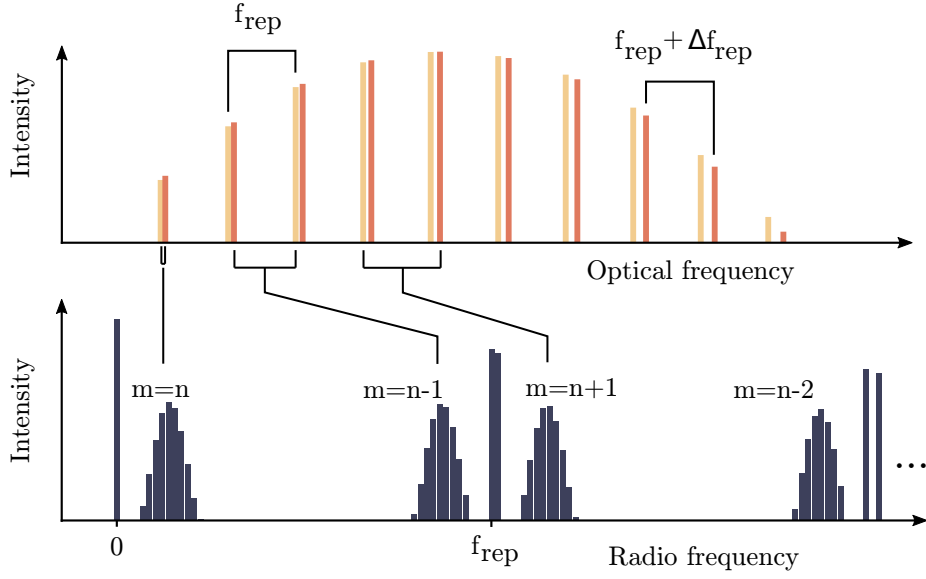
Figure 1.5: Detailed structure of the radio frequency signal resulting from the multi-heterodyning of two optical frequency combs. Multiple radio frequency combs are generated, whose frequencies depend on the mode number (m, n) of the optical lines mixing.

as

$$\Delta \nu \leq \frac{f_{rep}^2}{2\Delta f_{rep}}. \tag{1.11}$$

If the Nyquist criterion is fulfilled, overlap can be prevented by choosing Δf_{ceo} appropriately. The safest choice is to ensure that the center of the first radio frequency comb is located at $f_{rep}/4$. For the aforementioned case of $m = n$, this provides the condition

$$\bar{m}\Delta f_{rep} + \Delta f_{ceo} = \frac{f_{rep}}{4}, \tag{1.12}$$

where $\bar{m}$ is the mode number at the optical center of the frequency combs.

In practice, Δf_{rep} does not have to saturate Eq. 1.11, which also alleviates the requirement on Δf_{ceo}. However, Δf_{rep} can not be made arbitrarily small. While a perfect optical frequency comb exhibits spectral lines with delta-peak lineshapes, a real frequency comb exhibits a certain phase noise. This results in a broadening of the optical lines of the comb, whose linewidths typically stand in the tens of kHz or more. In a dual-comb spectrometer, the phase noise of the multi-heterodyne radio frequency signal corresponds to the fluctuations in the phase difference between the optical lines of the comb, as read from Eq. 1.7. If the combs' noises are uncorrelated, the radio frequency phase noise is approximately $\sqrt{2}$ times the optical phase noise of one comb, leading to linewidths in

the tens of kHz. To properly distinguish the radio frequency comb lines, their spacing needs to be greater than their linewidth, i.e. Δf_{rep} needs to be large enough, which limits the operating space given by Eq. 1.11.

To maximize the opportunities provided by a dual-comb spectrometer, it is then necessary to reduce the linewidths of the radio frequency comb lines. This is achieved by establishing mutual coherence between the optical frequency combs. With a high level of mutual coherence, both the repetition rate and offset frequency noise of each comb become highly correlated and cancel in the multi-heterodyning process, leading to potentially sub-Hz linewidths radio frequency beatnotes. In turn, Δf_{rep} can be made accordingly small, extending the boundary provided by Eq. 1.11.

Depending on the comb technology at hand, different methods can lead to high mutual coherence. For electro-optic combs, sharing the pump laser is extremely beneficial. For mode-locked lasers, control loops are usually employed to lock the combs together. Alternative approaches using multiplexed mode-locked lasers are now emerging as sources with natively high mutual coherence [24].

1.2.2   Applications

First proposed in 2002 by S. Schiller [12] and experimentally demonstrated in 2004 by F. Keilmann et al. [13], dual-frequency comb spectroscopy has since seen tremendous developments and numerous applications. Extensions of the technique to regions with prominent molecular spectral signatures have been demonstrated [25, 26, 27], as well as, its adaptation to nonlinear spectroscopy via stimulated Raman scattering spectroscopy [28], anti-Stokes Raman spectroscopy [29] and two-photon spectroscopy [30]. The technique has been used to perform e.g. broadband near-infrared spectroscopy [31], precision spectroscopy of molecular absorption lines, monitoring of greenhouse gases [32] and spectral lidar measurements [33]. Combination with well-established spectroscopic enhancement tools such as multi-pass cells and enhancement cavities have been shown [34]. Applications such as dual-comb cavity mode shift and width spectroscopy [35], dual-comb cavity ringdown spectroscopy [36], dual-comb ptychoscopy [37], dual-comb holography [38], dual-comb photothermal spectroscopy [39], dual-comb ranging [40], entanglement-enhanced dual-comb spectroscopy [41] and time-resolved dual-comb spectroscopy [42] have been demonstrated. The field of dual-frequency comb spectroscopy benefits from a consequent and sustained interest of the scientific community in general, with around 300 publications per year on or strongly connected to the subject.

1.3   Role of mutual coherence and repetition rate

As uncovered by Eq. 1.11, the opportunities provided by a dual-comb spectrometer depend on two fundamental characteristics: the repetition rate of the frequency combs and the mutual-coherence between the optical frequency combs.

These characteristics affect the maximal and minimal acquisition rate, the optical bandwidth, the resolution and the signal-to-noise ratio of the spectrometer.

1.3.1 Acquisition rate

The acquisition rate of a full spectrum is given by the repetition rate difference between the two frequency combs. From a time domain perspective, the acquisition time needed to record a full spectrum is the time required for the two optical frequency comb pulse trains to scan through each other, i.e. $\tau_{min} = 1/\Delta f_{rep}$. In the frequency domain, this minimal acquisition time is necessary to resolve the radio frequency comb lines, which are spaced by Δf_{rep}. The Nyquist criterion limits the maximal acquisition rate for a given optical bandwidth according to

$$\Delta f_{rep} \leq \frac{f_{rep}^2}{2\Delta\nu},\tag{1.13}$$

showing a beneficial quadratic scaling of the acquisition rate with the repetition rate. An alternative to achieving high acquisition rate is to limit the optical bandwidth of the spectrometer, which could be useful in specific cases.

As dual-frequency comb spectrometers do not rely on any mechanical moving parts, they can attain extremely high acquisition rates with applications in e.g. high-throughput screening, plasma physics and combustion monitoring. Repetition rate differences in the hundreds of kHz lead to acquisition times for full spectra in the μs range, providing high single-shot temporal resolution. In a scanning Fourier transform interferometer providing the same spectral information, such an acquisition rate would require a mirror scanning speed of around 100 km/s, which is approximately ten times the escape velocity of Earth.

On the other hand, operating at low Δf_{rep} provides a higher optical-to-radio frequency compression factor (limited by the combs' mutual coherence), enabling the usage of slow, high signal-to-noise ratio or specialty detectors.

1.3.2 Optical bandwidth

A spectrometer's spectral coverage is a central characteristics determining its potential applications. The Nyquist criterion imposes a limit on the optical bandwidth that can be covered by a dual-comb spectrometer according to

$$\Delta\nu \leq \frac{f_{rep}^2}{2\Delta f_{rep}}.\tag{1.14}$$

The maximal optical bandwidth thus scales quadratically with the repetition rate, while reducing Δf_{rep} provides a linear improvement. Broadband operation is then strongly facilitated in systems with high repetition rates and high mutual coherence operating at low repetition rate difference.

1.3.3 Spectral sampling and resolution

The optical resolution is a critical parameter of a spectrometer, as it must be high enough to properly sample the optical features of interest. A dual-comb spectrometer probes a sample at discrete frequencies, corresponding to the frequencies of the comb interrogating the sample. Consequently, the spacing of the optical sampling points is given by the repetition rate, a higher repetition rate leading to an inversely lower density of sampling points. To resolve narrow spectroscopic features such as gas-phase absorption fingerprints, the repetition rate should be kept lower than a few GHz. Alternatively, the density of optical sampling points can be increased by scanning the combs' parameters, at the cost of acquisition speed and technical complexity. With such technique, the ultimate limit on the optical resolution of the spectrometer is given by the optical linewidth of the comb lines.

1.3.4 Signal-to-noise ratio

When operating in a regime with sufficient optical power, linearity of the photodetector dictates the overall usable power. For a given spectral bandwidth, the number of comb lines is inversely proportional to the repetition rate; the optical power per comb line thus scales linearly with the repetition rate. In consequence, the signal-to-noise ratio scales linearly with the repetition rate of the oscillators [43].

In addition, the signal-to-noise ratio of a dual-comb spectrometer also depends indirectly on the mutual coherence between the frequency combs. When one acquires multiple subsequent interferograms, optimal signal-to-noise ratio is only achieved for the time of mutual coherence between the two combs. On longer time scales, phase drifts lead to destructive interference between interferograms that reduce the signal-to-noise ratio. Artificial elongation of the coherence time can be achieved via numerical phase correction techniques (see Appendix B), although noise at frequencies higher than Δf_{rep} can not be removed, favoring systems with high mutual coherence and high Δf_{rep}. Systems thus require a certain initial degree of mutual coherence for phase correction algorithms to be effective and maximize the signal-to-noise ratio.

1.4 High-coherence and high-repetition rate dual-comb spectroscopy

The quadratic scaling of the achievable optical coverage, as well as, the acquisition speed with the repetition rate creates a strong incentive to build dual-comb spectrometers with high repetition rate optical frequency combs. Furthermore, the signal-to-noise ratio scales linearly with the repetition rate. At the same time, the density of optical sampling points is inversely proportional to the repetition rate, pushing towards lower repetition rates. In practice, an excellent choice of repetition rate is 1 GHz, which still provides enough sampling points to

resolve narrow gas-phase molecular absorption features. This thesis explores the prospects presented by high repetition rate, high mutual coherence dual-comb spectrometers.

1.4.1 Opportunities and challenges

Dual-comb spectroscopy with 1 GHz-high repetition rate lasers permits fast and broadband spectroscopy with high optical resolution, as it leads to a hundred-fold improvement of the Nyquist criterion (Eq. 1.11) over more standard architectures based on 100 MHz or lower repetetion rate oscillators. However, high repetition rate sources come with an inherently lower peak power, which complicates self-referencing and spectral broadening. Another noteworthy challenge comes in the form of the large amount of data generated by a high repetition rate dual-comb spectrometer. To properly resolve the multi-heterodyne signal and fully benefit from the high repetition rate advantages, a sampling rate in excess of 1 GHz must be achieved and the resulting high data rate must be properly handled for optimal operation.

The compression ratio measuring the system's capability to down-convert information from the optical domain to the radio frequency domain is ultimately limited by the mutual coherence between the combs. Mutual coherence also dictates the time for which a dual-comb signal can be coherently averaged, as this time is limited by the radio frequency comb's phase noise. The fundamental challenge in dual-comb spectroscopy is thus to establish a high mutual coherence between the two optical frequency combs. Dual-comb spectrometers with high mutual coherence can push broadband operation further, while also permitting operation at low acquisition rates and lower noise, paving the way towards fascinating applications relying on slow, specialty detectors.

This thesis demonstrates novel opportunities for molecular sensing, rapid broadband optical spectroscopy and fundamental astronomical precision measurements using two different kinds of 1 GHz repetition rate, high mutual coherence dual-comb spectrometers.

1.4.2 1 GHz electro-optic dual-comb spectrometer

The first two publications presented in this thesis leverage the high mutual coherence of a frequency-agile dual-comb spectrometer based on electro-optic modulation of a single tunable continuous wave laser [44]. Such systems are highly re-configurable and convenient to use, as basic electronics directly dictate the combs' repetition rates and offsets, providing simple access to the repetition rate difference and offset frequency difference that govern the evolution of the multi-heterodyne signal. In particular, combs with a repetition rate of 1 GHz are quite easily implemented in electro-optic systems by using appropriate radio frequency signal generators. While the low peak powers typically associated with electro-optic combs driven in the GHz range limit the spectral coverage of the spectrometer, this shortcoming is alleviated by the frequency agility provided by the tunable seed laser. The operating wavelength can be chosen according to

the application and dual-comb spectroscopy at high spectral resolution can be performed in the region of interest. The high mutual coherence of this system is derived from the use of a single continuous wave laser as a shared seed for the two electro-optic combs, resulting in a coherence time longer than a second. In accordance, the necessary acquisition rate for the recording of the heterodyne signal can be reduced to sub-Hz level, which enables the use of slow, exotic detection techniques with impressive applications, two of which are explored here.

1.4.3   Photo-acoustic dual-comb spectroscopy

The first experiment presented in Chapter 2 demonstrates a novel application enabled by the high coherence electro-optic dual-comb spectrometer: photo-acoustic dual-comb spectroscopy. This technique leverages the achievable high compression ratio to down-convert optical frequencies to acoustic frequencies. The frequency combs are sent on an sample which absorbs, heats and expands periodically, giving rise to acoustic waves whose amplitudes directly depend on the absorbed intensity of the comb light. In analogy with Eq. 1.7, these acoustic waves carry the multi-heterodyne signal of the dual-comb interferometer imprinted with the absorptive optical features of the sample. Provided a high down-conversion compression ratio is reached, a sensitive microphone can record the acoustic signal and give access to the sample's optical spectrum. As the technique is based on the detection of the acoustic waves rather than of a weak attenuation of the optical signal, it is background-free and permits extremely high sensitivities to be reached. Importantly, the detection scheme is not limited by the bandwidth of an optical detector, enabling in principle highly sensitive, broadband measurements across the whole electromagnetic spectrum at high resolution and can be directly applied to gases, liquids, solids and even to opaque samples. In this demonstration, narrow absorption features of acetylene gas are measured and the retrieved spectra are in excellent agreement with the HITRAN database with acquisition times as short as 8 ms, demonstrating the exciting potential of the technique for fast, background-free measurements with comb accuracy and precision at high signal-to-noise ratios in any spectral region.

1.4.4   Dual-comb hyperspectral imaging

The second experiment presented in this thesis in Chapter 3 pushes the use of the high mutual coherence of the electro-optic dual-comb spectrometer even further by demonstrating real-time dual-comb hyperspectral imaging. An imaging detector array with ∼16'000 pixels is used to record a dual-comb signal traversing an absorbing gas jet, permitting a high resolution hyperspectral image of the sample to be reconstructed. The detector array's frame rate of 1 kHz implies that the heterodyne signal must be contained in the radio frequency band from DC to 500 Hz to be properly resolved, necessitating an extremely dense packing of the radio frequency beatnotes with Hz-level separation. High compression

ratios from the optical domain to the radio frequency of 10^8 are used in this experiment, with a refresh rate of the hyperspectral images of 10 Hz over 30 spectral channels. When combining the information of the different spectral channels to retrieve the spatial concentration of the interrogated sample, conventional data analysis fails to keep up with the volume of data generated by the massively multiplexed spatial and spectral measurement. For this reason, a neural network is trained to achieve data reduction in fast fashion, enabling realtime dual-comb hyperspectral imaging of an acetylene gas jet. The technique has potentially far-reaching applications in bio-medical imaging, combustion monitoring, leak detection or identification of hazardous substances.

1.4.5   1 GHz mode-locked laser dual-comb spectrometer

High repetition rate dual-comb spectroscopy is appealing due to the advantages it exhibits in signal-to-noise ratio, acquisition speed and spectral coverage. However, most systems aiming at broadband coverage rely on low repetition rate ($\lesssim$ 100 MHz) lasers. In the third publication of this thesis in Chapter 4, we demonstrate for the first time the conception of a high mutual coherence, 1 GHz repetition rate dual-comb spectrometer built upon Erbium-based mode-locked lasers, capable of broadband and fast acquisitions. The performances of the system are showcased by performing broadband measurements of the vibrational spectrum of water vapor, as well as, fast, single shot measurements of the acetylene absorption spectrum in few μs acquisition times, both in regimes unattainable by 100 MHz-based spectrometers. The system's high mutual coherence is established via versatile FPGA-based control loops and opens new opportunities for broadband infrared spectroscopy at high and low acquisition rates.

1.4.6   Dual-comb astronomical spectrograph calibration

Astronomical precision spectroscopy enables the search for exoplanets and the monitoring of fundamental constants of physics. To detect Earth-like exoplanets via the radial velocity method, astronomical spectrographs need to be able to detect optical frequency shifts as small as tens of kHz over typical time spans of a year. Consequently, a regular, precise and accurate calibration of astronomical spectrographs is necessary. An ideal light source for calibration would provide a series of markers to the spectrograph known with comb precision with a frequency spacing matched to the spectrograph's resolution. Laser frequency combs with repetition rates in the tens of GHz (astrocombs) can deliver appropriate calibration markers, although are held back by their high cost and their challenging day-to-day operation [45, 46, 47, 48, 49, 50]. Alternatively, a Fabry-Pérot-filtered white-light supercontinuum can robustly and cost-effectively deliver calibration markers to an astronomical spectrograph, although the technique lacks the desirable comb accuracy [51, 52, 53, 54, 55].

In Chapter 5, a novel calibration method for astronomical spectrographs based on the combination of a Fabry-Pérot calibrator and the previously devel-

oped dual-comb spectrometer is presented. It leverages the broadband coverage offered by the high mutual coherence dual-comb spectrometer to perform cavity mode spectroscopy of an astronomical Fabry-Pérot cavity over a large spectral bandwidth. This information is used to link the generated calibration markers to an atomic time standard, providing absolutely-known, precise and accurate calibration light for astronomical spectrographs. Using this calibration light, Doppler shifts as low as state-of-the-art 25 cm/s are expected to be detectable. This technique has the important advantages of circumventing the need for frequency combs with repetition rates in the tens of GHz and is based on mature and robust technology.

1.4.7 Simulating mixed and cascaded nonlinearities

Inherent to 1 GHz high-repetition rate lasers, relatively low peak powers render spectral extension of the sources challenging, potentially limiting the spectral coverage of the spectrometer. Similarly, wavelength conversion towards visible and far-infrared via quadratic or cascaded nonlinear processes is hard to achieve. Towards these ends, the last publication of this thesis presented in Chapter 6 is dedicated to the development of an open-source software for simulating the propagation of short pulses in nonlinear media exhibiting quadratic, cubic, mixed and cascaded nonlinearities. This tool permits the optimization of supercontinuum generation and frequency conversion inside waveguide-like structures, providing a path towards ultra-broadband spectroscopy and its extension to the visible, mid- and far-infrared ranges. In particular, the field of integrated optics holds great promises to achieve ultra-broadband spectroscopy thanks to high nonlinearities, tight confinement of light and dispersion that can be engineered.

This software provides the basis for extending this thesis' demonstrations to new spectral regions, for exciting applications. Follow-up research on photo-acoustic dual-comb spectroscopy, as well as, real-time dual-comb hyperspectral imaging in the mid- and far-infrared where spectral signatures of molecules are strong can be envisioned. The novel method for astronomical spectrograph calibration could be transferred in the critical visible and ultraviolet ranges.

In addition to the field of broadband spectroscopy, this software is generally useful for the simulation of any spatially co-linear nonlinear propagation process. As such, it can be used to optimize supercontinuum generation in waveguides, fibers, gases, as well as, frequency conversion in crystals or periodically poled structures, among others. It has been written in python with ease-of-use in mind, so that the optics community in general can benefit from it.

1.4.8 Organization of this thesis

This thesis is organized as follows.

Chapter 2 demonstrates dual-comb spectroscopy with a photo-acoustic detection scheme, yielding background-free measurement of molecular absorption fingerprints for any wavelength of light.

Chapter 3 showcases real-time, high spectral resolution dual-comb hyperspectral imaging in the infrared with a detector array.

In Chapter 4, the challenge of building a 1 GHz mode-locked laser-based dual-comb spectrometer with high mutual coherence is undertaken, permitting broadband dual-comb spectroscopy at high acquisition rates, based on mature and commercially available technologies.

In Chapter 5, a novel calibration method for astronomical spectrographs based on the combination of a Fabry-Pérot calibrator with the developed dual-comb spectrometer is presented.

Chapter 6 is dedicated to the development of an open-source software for simulating the propagation of short pulses in nonlinear media exhibiting quadratic, cubic, mixed and cascaded nonlinearities to facilitate the spectral broadening of high repetition rate lasers.

Chapter 2

Photo-acoustic dual-frequency comb spectroscopy

Thibault Wildi[1,2,†], **Thibault Voumard**[1,2,†], **Victor Brasch**[1], **Gürkan Yilmaz**[1], **Tobias Herr**[1,2]

[1] *Swiss Center for Electronics and Microtechnology (CSEM), Rue de l'Observatoire 58, 2000 Neuchâtel, Switzerland*
[2] *Center for Free-Electron Laser Science (CFEL), Deutsches Elektronen-Synchrotron (DESY), Notkestr. 85, 22607 Hamburg, Germany*
[†] *These authors contributed equally.*

Context

Photo-acoustic dual-comb spectroscopy is a first demonstration of the potency of high mutual coherence dual-frequency comb spectroscopy with high repetition rate combs. The high compression ratio provided by the electro-optic dual comb spectrometer permits a dense packing of the heterodyne beatnotes, enabling the use of a kHz-bandwidth microphone as a transducer. The advantages of the technique manifest themselves in the agnosticism of the detection system to the probing wavelength, background-free operation and high signal-to-noise ratio.

Author contribution

The author and T. Wildi jointly conceived and built the setup, conducted the data acquisition and data analysis. The author conducted additional data acquisition and data analysis. The author and T. Herr jointly wrote the manuscript.

Photo-acoustic dual-frequency comb spectroscopy

Photo-acoustic spectroscopy (PAS) is one of the most sensitive non-destructive analysis techniques for gases, fluids and solids. It can operate background-free at any wavelength and is applicable to microscopic and even non-transparent samples. Extension of PAS to broadband wavelength coverage is a powerful tool, though challenging to implement without sacrifice of wavelength resolution and acquisition speed. Here we show that dual-frequency comb spectroscopy (DCS) and its potential for unmatched precision, speed and wavelength coverage can be combined with the advantages of photo-acoustic detection. Acoustic wave interferograms are generated in the sample by dual-comb absorption and detected by a microphone. As an example, weak gas absorption features are precisely and rapidly sampled; long-term coherent averaging further increases the sensitivity. This novel approach of dual-frequency comb photo-acoustic spectroscopy (DCPAS) generates unprecedented opportunities for rapid and sensitive multi-species molecular analysis across all wavelengths of light.

2.1   Introduction

In PAS [56, 57, 58, 59], optical absorption of a modulated light source leads to periodic heating of a sample and the generation of an acoustic wave that can be detected by a microphone or an equivalent transducer (Figure 2.1a). As the detection relies on the acoustic waves (rather than a weak attenuation of an optical signal), photo-acoustic detection can be background-free, with high signal-to-noise ratio (SNR), and importantly, works at any wavelength of light. These unique properties have established PAS in environmental studies, solid state physics, chemical process control, medical application and life science, including for instance absorption measurements in atto-liter droplets [60], real-time monitoring of an ant's respiration [61] and in-vivo tomographic imaging [62]. Quartz-enhanced photo-acoustic spectroscopy (QEPAS)[63, 64, 65] and cantilever-enhanced photo-acoustic spectroscopy (CEPAS) [66, 67] have enabled ultra-sensitive trace gas detection below the part-per-trillion-level[68, 69].

Usually, PAS is performed at one single probing laser wavelength not ideal for the study of multiple species or studies in the presence of uncontrolled background absorption. Multiple laser sources can alleviate this problem to some extent, however, remain constraint to specific use cases. Therefore, in order to achieve broadband wavelength coverage, photo-acoustic detection has been combined with Fourier-transform infrared spectrometers (FTIR-PAS) [70]. The achievable resolution is determined by the scan range of the interferometer, which can reach several meters for high resolution instruments. In addition to temporally incoherent light sources, such as super-continua [71], coherent broadband spectra (unresolved optical frequency combs) have also been used to improve the overall performance [72, 73], and might allow adopting techniques for sub-nominal resolution [74] in the future. As such FTIR-PAS represents a powerful tool for broadband photo-acoustic spectroscopy. However, FTIR-PAS

relies on a mechanical scan, which can limit its resolution and acquisition speed and requires mechanically stable setups.

Here, we show that the resolution and speed limitations in broadband PAS can be overcome by combining the concept of dual-frequency comb spectroscopy (DCS)[10, 11, 12, 13, 75] with photo-acoustic detection resulting in the new technique of dual-frequency comb photo-acoustic spectroscopy (DCPAS). Photo-acoustic dual-comb multi-heterodyne detection enables the rapid and scan-free acquisition of absorption features with high resolution and precision (traceable to the SI-time standard), thereby enabling background-free, broadband spectroscopy of gases, liquids and solids at any wavelength of light.

2.2   Results

2.2.1   Concept

Figure 2.1b illustrates the concept of DCPAS. Similar to conventional DCS, two frequency combs are used in our demonstration whose optical frequency components $\nu_n^{(i)}$ are described by

$$\nu_n^{(i)} = n \cdot f_{\text{rep}}^{(i)} + \nu_0^{(i)} \,, \tag{2.1}$$

$f_{\text{rep}}^{(i)}$ and $\nu_0^{(i)}$ denote the repetition rate (i.e. the comb line spacing) and the combs' optical offset frequencies, respectively. The index $i = 1, 2$ distinguishes the two combs, and $n = 0, \pm1, \pm2, ..$ are the comb line indices. The combs' repetition rates and offsets differ only by small amounts $\Delta f_{\text{rep}} = \left| f_{\text{rep}}^{(1)} - f_{\text{rep}}^{(2)} \right| \ll f_{\text{rep}}^{(1,2)}$, and $\Delta\nu_0 = \left| \nu_0^{(1)} - \nu_0^{(2)} \right| \ll f_{\text{rep}}^{(1,2)}$, so that pairs of optical comb lines $\nu_n^{(1)}$ and $\nu_n^{(2)}$ are only separated by acoustic frequencies. When both combs are optically combined, this can be interpreted as a single frequency comb

$$\tilde{\nu}_n = n \cdot \tfrac{1}{2} \left(f_{\text{rep}}^{(1)} + f_{\text{rep}}^{(2)} \right) + \tfrac{1}{2} \left(\nu_0^{(1)} + \nu_0^{(2)} \right) \,, \tag{2.2}$$

whose n^{th} optical line is modulated in optical power according to $1 + \cos\left(2\pi f_n t + \phi_n \right)$ with frequency

$$f_n = \left| \nu_n^{(1)} - \nu_n^{(2)} \right| = n \cdot \Delta f_{\text{rep}} + \Delta\nu_0 \tag{2.3}$$

and a phase ϕ_n. Exposing the sample to the dual combs, it experiences periodic heating with frequency f_n if light at the optical frequency $\tilde{\nu}_n$ is absorbed. The periodic heating will lead to the generation of heterodyne acoustic waves in function of the absorbed power. Note that different from conventional DCS, the heterodyning does not happen on an external photo-detector, but indeed in and by the sample itself. The superposition of all acoustic waves results in a series of interferograms, each with a duration of $\Delta f_{\text{rep}}^{-1}$, that is detectable by a microphone or an equivalent transducer, provided all acoustic frequencies f_n respect the bandwidth limitation of the transducer.
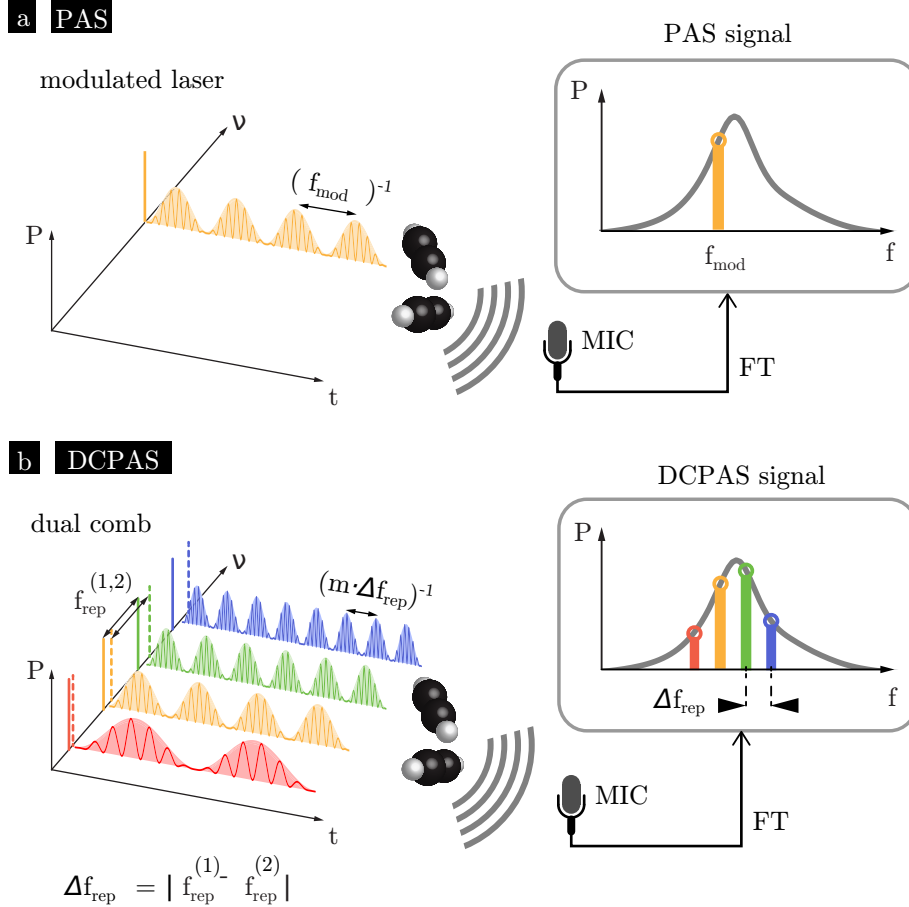
Figure 2.1: **Dual-frequency comb photo-acoustic spectroscopy.** **a** In photo-acoustic spectroscopy (PAS), absorption of a modulated laser results in acoustic waves that are recorded by a microphone (MIC). The acoustic spectrum (after Fourier transformation, FT) contains the PAS signal tone at the modulation frequency f_{mod} that indicates the strength of the optical absorption. **b** Dual-frequency comb photo-acoustic spectroscopy (DCPAS) uses broadband dual-frequency combs, whose repetition rates $f_{\mathrm{rep}}^{(1)}$ and $f_{\mathrm{rep}}^{(2)}$ differ by a small amount Δf_{rep}. The DCPAS signal is comprised of multiple heterodyne acoustic tones that simultaneously sample the optical absorption spectrum at multiple optical frequencies. (P: power; ν and f: optical and acoustic frequencies; t: time.)

2.2.2 Setup

Key to our demonstration are dual-frequency combs with high mutual coherence that enable dense packing of the acoustic multi-heterodyne beatnotes f_n within the microphone's bandwidth. Dual combs with high mutual coherence have been implemented in various ways based on mode-locked lasers or electro-optic modulation [76, 77, 31, 44, 78, 79, 80, 81, 82, 83, 84, 85], and have also been extended to the infrared molecular fingerprint regime [86, 87, 88, 89].

In this proof-of-concept demonstration, we use two near-infrared electro-optic combs as shown in (Figure 2.2a) with a tunable central wavelength around 1535 nm and each with approximately 40 comb lines, spaced by $f_{\mathrm{rep}}^{(1)} = 1$ GHz and $f_{\mathrm{rep}}^{(2)} = f_{\mathrm{rep}}^{(1)} + 125$ Hz, respectively. The combs' relative central offset is adjusted to $\Delta\nu_0 = 4$ kHz as further explained in the Methods section. Combined, both combs deliver 20 mW of average power for photo-acoustic detection.

The combs are sent through a sample cell (see Methods for details) in an 8-fold multi-pass configuration and an off-the-shelf digital micro-electro-mechanical system (MEMS) microphone with 20 kHz bandwidth is used to record the acoustic signal. The repetition rate difference of $\Delta f_{\mathrm{rep}} = 125$ Hz was chosen so that all acoustic multi-heterodyne beatnotes would be within 2 to 6 kHz and well within the microphone's bandwidth. Given the combs' high mutual coherence (sub-Hz multi-heterodyne beatnotes), we note that more beatnotes (i.e. more optical sampling points) could readily be accommodated by lowering Δf_{rep}.

A small fraction of the comb light is sent to a photo-detector that provides a reference for normalization of the photo-acoustic signal and also enables an enhancement of the combs' mutual coherence in post-processing, as we detail below. In a wavelength regime where suitable photo-detectors may not be available, the reference detector could be implemented by photo-acoustic detection of black-body absorption. Both the microphone as well as the photo-detector signals are sampled.

2.2.3 Measurements

As a spectroscopic target we choose acetylene gas (C_2H_2) at atmospheric pressure and lab temperature as it provides well-known, precisely defined and interference-free absorption features uniquely suitable for validating the new DCPAS method. In a first experiment, the absorption cell is filled with acetylene gas and probed at 1536.71 nm (spectral line strength of $4.882 \cdot 10^{-21}$ cm/molecule), giving rise to the heterodyne acoustic interferogram signal shown in Figure 2.2b. Figure 2.3a shows two examples of the heterodyne acoustic spectra after Fourier-transformation [90] (DCPAS signal) for acquisitions with durations of 80 ms (10 interferograms) and 800 ms (100 interferograms), respectively. As expected, a longer acquisition time yields a higher SNR in the DCPAS signal. The absence of a DCPAS signal below 2.4 and above 5.6 KHz is due to the combined drop in the absorption feature and the comb lines intensity. Indeed, and in contrast to conventional DCS, photo-acoustic multi-heterodyne beatnotes are only gen-
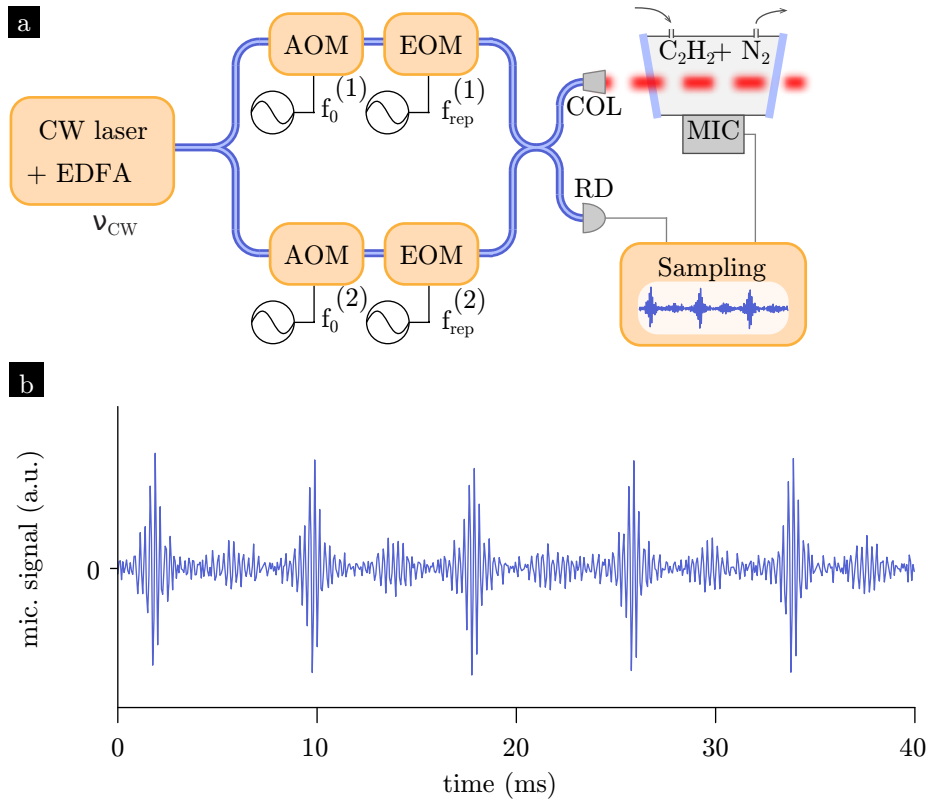
Figure 2.2: **Experimental setup. a** Experimental setup for the photo-acoustic detection of gaseous acetylene (C_2H_2). A tunable continuous-wave (CW) laser with optical frequency ν_{CW} is amplified by an erbium-doped fiber amplifier (EDFA) and used as a common seed for the generation of two optical frequency combs with repetition rates of $f_{rep}^{(1)}$ and $f_{rep}^{(2)}$ via electro-optic modulation (EOM). Acousto-optic modulation (AOM) of the CW laser with $f_0^{(1)}$ and $f_0^{(2)}$ controls the relative offset between both combs. (COL: free space collimator; PD: reference photo-detector MIC: low-noise MEMS microphone, see Methods for more details). **b** Acoustic multi-heterodyne signal recorded by the microphone (5 interferograms; after high-pass filtering) for an acetylene filled cell.

24
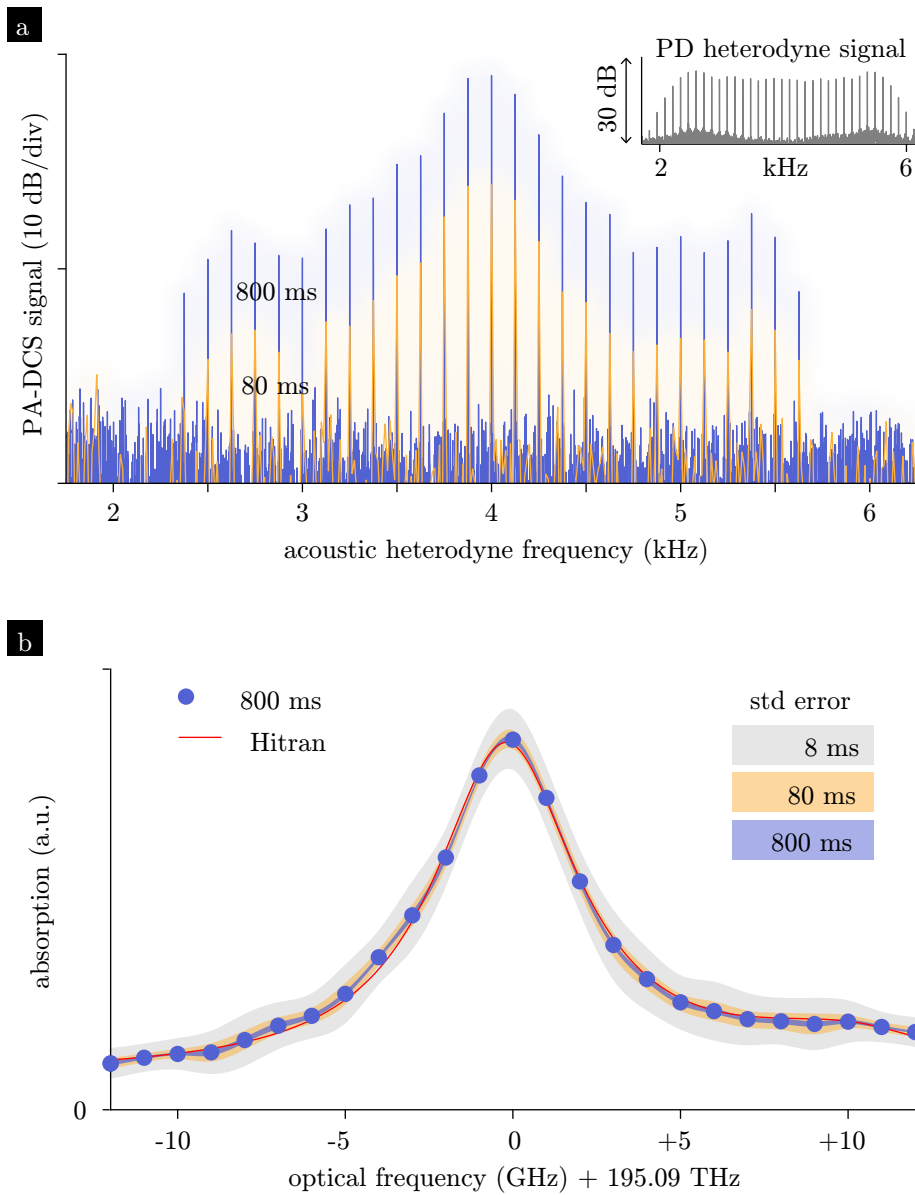
Figure 2.3: **Results. a** Spectrum of the acoustic multi-heterodyne signal for 80 ms and 800 ms long acquisitions. Inset: Multi-heterodyne reference spectrum as recorded by the reference photo-detector (over the same span). **b** Acetylene absorption signature obtained after normalizing the acoustic multi-heterodyne spectrum by the reference spectrum for an 800 ms acquisition duration (blue dots); shaded areas (grey, yellow, blue) represent the standard-error intervals for different acquisition durations (8 ms, 80 ms and 800 ms). The red line shows the HITRAN model for comparison.

erated in spectral regions where light is absorbed. Therefore, the number of photo-acoustic multi-heterodyne beatnotes is generally smaller than the number of comb lines. Although this does not allow for measurement of absolute absorption values without prior calibration, it avoids large (shot noise) background signals that can mask spectrally sparse or weak absorption features in conventional DCS [43].

In order to retrieve the true absorption profile, the acoustic multi-heterodyne beatnotes are normalized to account for the uneven spectral power envelope of the combs. Here, we accomplish this by dividing the DCPAS signal (Figure 2.3a) by the photo-detected multi-heterodyne reference beatnotes (inset in Figure 2.3a). The mapping of the acoustic to the optical frequency axis is described by Eqs. 2.2 and 2.3, implying a compression factor of $(f_{\mathrm{rep}}^{(1)} + f_{\mathrm{rep}}^{(2)})/(2\Delta f_{\mathrm{rep}}) \approx 8 \times 10^6$ between acoustic and optical frequency axes. The resulting C_2H_2-absorption signature is shown and compared to the HITRAN model [91, 92] in Figure 2.3b: Blue dots show the absorption retrieved from an 800 ms long acquisition and shaded areas (grey, yellow, blue) represent the standard-error intervals for different durations of acquisition (8 ms, 80 ms and 800 ms). Excellent agreement between the HITRAN-model (red line) and the measured absorption profile is achieved, with the smallest residuals (below 3% relative to peak absorption) observed with an 800 ms long acquisition. The grey shaded area indicates that a fast, 8 ms long acquisition (i.e. a single interferogram) is sufficient to retrieve the coarse features of the absorption profile. The spectral resolution for each sampling point is given by the combs' absolute optical linewidth (here: ∼100 kHz), so that instrumental lineshape effects are negligible (resolution 5 orders of magnitude below the width of the absorption feature). Moreover, the frequency spacing of the sampling points (1.0000000675 GHz) is precisely defined by the mean repetition rate of the two combs (Eq. 2.2). The absolute frequency offset of the frequency combs is obtained by aligning the measured absorption feature with the HITRAN model, which is straightforward as the shape of the absorption line is recorded.

Next, we investigate the extent to which even longer recordings of time τ can increase the SNR. To explore this, the cell is filled with N_2-diluted C_2H_2 with a concentration of 1% and probed by combs centered at 1532.83 nm (spectral line strength of $1.035 \cdot 10^{-20}$ cm/molecule). Acquisitions of different duration are processed (similar to what is shown in Figure 2.3) and the SNR of the highest acoustic beatnote (at 4 kHz) is determined as a function of τ. Indeed, as Figure 2.4 shows, the SNR increases with τ (yellow trace), however, it markedly deviates from the $\tau^{1/2}$-scaling one would expect in a scenario with perfect noise-averaging. This deviation is due to small and slow length fluctuations in the non-common optical path of the combs that limits their mutual coherence on the time scale of few seconds or longer. These slow fluctuations manifest themselves as phase drifts in the multi-heterodyne beatnotes, which fortunately, can easily be tracked and corrected for numerically [77, 93, 28, 94, 95, 96, 97]. Here, we extract the phase drift (one phase value for all heterodyne beats) from the reference heterodyne signal and, after low-pass filtering (< 0.1 Hz), subtract it from the

phase of the heterodyne acoustic beatnotes. This a-posteriori phase-correction extends the effective mutual-coherence time of the combs by compensating for the slow path length fluctuations. As shown by the blue trace in Figure 2.4, phase correction results in an increase of the SNR close to the ideal scaling (black line) up to the maximal recording duration of 1 hour. This result suggests that even longer recordings could be leveraged to further increase the signal to noise ratio. A small deviation from the ideal scaling is observed for acquisitions longer than 300 s and attributed to residual differential phase drifts between the heterodyne beatnotes, which could be addressed by tracking the phase of each beatnote separately. To further illustrate the effect of phase correction, the inset in Figure 2.4 shows a zoom on the central heterodyne acoustic beatnote for a recording time of 1000 s. With phase correction applied (blue trace), a narrow 1 mHz linewidth heterodyne beatnote is detected. Without phase correction (yellow trace) the drifting beatnote has a reduced SNR. Generally, in photo-acoustic spectroscopy, the SNR depends on the used optical power, the absorption coefficient, the photo-acoustic cell design [98], the microphone, the surrounding matter, environmental conditions (pressure, temperature) as well as the recording duration. In the current proof-of-concept configuration, based on the SNR in Figure 2.4, we estimate a minimal detectable noise equivalent C_2H_2 concentration of 10 ppm for a recording time of 1000 s. This shows that coherent averaging can also be applied in DCPAS, providing additional opportunities for increasing the sensitivity.

2.3 Discussion

In conclusion, we have demonstrated dual-frequency comb photo-acoustic spectroscopy (DCPAS) as a novel broadband spectroscopic technique that can achieve high resolution, rapid acquisition (here: as short as 8 ms) and sensitive detection. While this demonstration is performed in the near-infrared wavelength range, the concept can readily be translated to any other wavelength range where suitable comb sources are available [9, 11]. Therefore, in the mid-infrared and other wavelength regimes where photo-detection is challenging, DCPAS can complement existing DCS approaches (e.g. those based on optical field sampling or up-conversion [25, 99]). Importantly, it can also operate on microscopic and even non-transparent samples. In this proof-of-concept demonstration, we have used a very basic photo-acoustic cell design. More elaborate designs with optimized geometries, leveraging optical and acoustic cavity enhancement, could be used to improve the sensitivity [100, 98, 101]. In addition, more powerful dual-comb laser sources, such as high power quantum-cascade laser combs [102, 103] could enhance the photo-acoustic signal. Further, broadband dual-comb spectra from mode-locked lasers with high-mutual coherence [76, 31] as well as sensitive multi-MHz bandwidth optical microphones [104, 105], and potentially opto-mechanical transducers [106, 107, 108] could be used to extend the spectral coverage. Particularly for those application where low spectral resolution is sufficient, e.g. in in-vivo hyperspectral tomographic imaging [62],
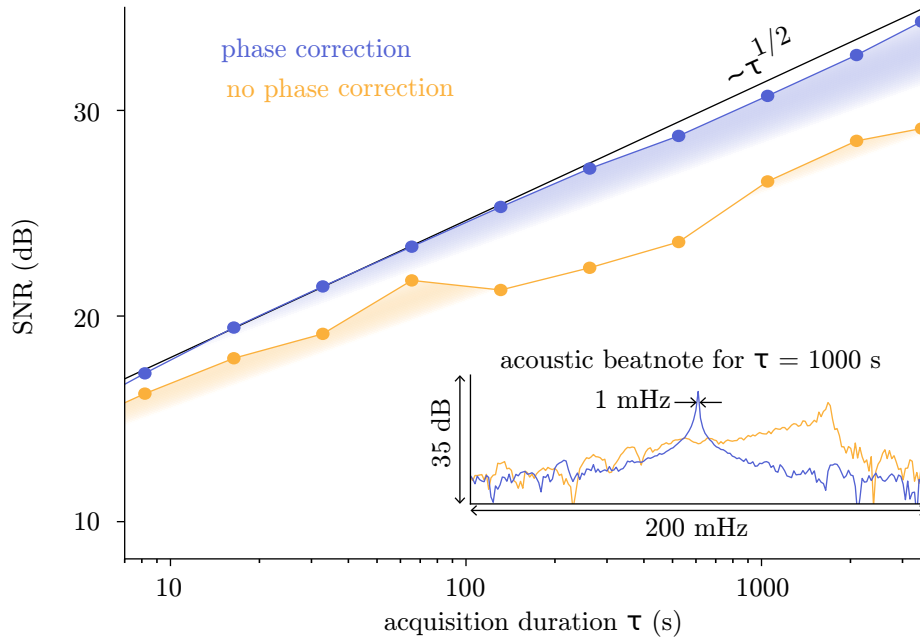
Figure 2.4: **Long-term acquisition.** Signal-to-noise ratio (SNR) with (blue) and without (yellow) phase correction as a function of acquisition duration τ. The black line indicates the ideal case where the SNR increases proportionally to $\tau^{1/2}$. Inset: Central heterodyne acoustic beatnote spectrum for $\tau =$1000 s with(blue) and without (yellow) phase correction.

low-noise high-repetition rate soliton microresonator combs [109, 110, 111] could enable very fast acquisition over a large spectral range. As such, our demonstration generates new opportunities for rapid, sensitive broadband, chemically specific analysis of gases, liquids and solids across all wavelengths of light. The authors would like to make the reader aware of recent parallel work demonstrating the novel method of DCPAS for polymer films [112], further highlighting the method's potential as a versatile analysis tool.

2.4 Methods

2.4.1 Dual-frequency comb source

In order to ensure high mutual coherence between both electro-optic combs, they are derived from a single, free-running continuous-wave (CW) tunable external cavity diode laser with optical frequency ν_{CW}. Using a free-running laser does not limit the precision of the absorption measurement as the full absorption line profile is recorded. The CW laser is amplified in an erbium-doped fiber amplifier (EDFA) and split into two beams, each traversing first an acousto-optic

modulator (AOM) where the laser frequencies are shifted by $f_0^{(1)} = 80$ MHz and $f_0^{(2)} = 80$ MHz + 4 kHz, respectively (i.e. $\nu_0^{(1,2)} = \nu_{\mathrm{CW}} + f_0^{(1,2)}$), to create a relative comb offset of $\Delta\nu_0 = 4$ kHz. Next, each beam passes through an electro-optic modulation (EOM) stage that includes one intensity and two phase modulators to generate a series of approximately 40 comb lines, spaced by $f_{\mathrm{rep}}^{(1)} = 1$ GHz and $f_{\mathrm{rep}}^{(2)} = f_{\mathrm{rep}}^{(1)} + 125$ Hz, respectively. All modulation sources are synchronized to a 10 MHz frequency standard to ensure precise sampling and coherence in the acquisition process.

2.4.2   Sample cell

An aluminum tube (diameter 4 mm, length 10 mm) whose ends are sealed by angled glass windows serves as the photo-acoustic sample cell. The multi-pass configuration of the comb light is achieved via two slightly tilted flat mirrors arranged around the cell. Attached to the sidewall of the tube and connected through a small hole is an off-the-shelf digital MEMS microphone (ICS-43434) with a sensitivity of -26 dBFS at 94 dB sound pressure level (SPL) and an equivalent input noise of 30 dBA SPL. A battery-powered amplifier and digitizer is used to record the acoustic signals for a memory limited duration of up to 1 hour.

Chapter 3

AI-enabled real-time dual-comb molecular fingerprint imaging

Thibault Voumard[1,†], **Thibault Wildi**[1,†], **Victor Brasch**[2], **Raúl Gutiérrez Alvarez**[3], **Germán Vergara Ogando**[3], **and Tobias Herr**[1]

[1] *Center for Free-Electron Laser Science, Deutsches Elektronen-Synchrotron, Notkestr. 85, 22607 Hamburg, Germany*
[2] *Time and Frequency, Centre Suisse d'Electronique et de Microtechnique (CSEM), Jaquet-Droz 1, 2000 Neuchâtel, Switzerland*
[3] *New Infrared Technologies (NIT), Calle Vidrieros 30, Boadilla del Monte, 28660 Madrid, Spain*
† *These authors contributed equally.*

Context

Harnessing the opportunities offered by the high mutual coherence, electro-optic dual-comb spectrometer even further than required for photo-acoustic spectroscopy, this experiment demonstrates real-time dual-comb hyperspectral imaging by using a detector array for dual-comb detection. The infrared detector array's frame rate of 1 kHz pushes towards extremely high down-conversion compression ratios, here reaching 10^8 and permitting the capture of hyperspectral images with 30 spectral channels, more than 16'000 pixels and a 10 Hz refresh rate. The high data rate of the system is processed in real-time through a dedicated artificial neural network.

Author contribution

The author and T. Wildi jointly conceived and built the setup, conducted the data acquisition and data analysis. The author conducted additional data acquisition and data analysis. The author conceived, built and trained the artificial intelligence for data analysis. The author and T. Herr jointly wrote the manuscript.

AI-enabled real-time dual-comb molecular fingerprint imaging

Hyperspectral imaging provides spatially resolved spectral information. Utilizing dual frequency combs as active illumination sources, hyperspectral imaging with ultra-high spectral resolution can be implemented in a scan-free manner when a detector array is used for heterodyne detection. Here, we show that dual-comb hyperspectral imaging can be performed with an uncooled near-to-mid-infrared detector by exploiting the detector array's high framerate, achieving 10 Hz acquisition in 30 spectral channels across 16'384 pixel. Artificial intelligence enables real-time data reduction and imaging of gas concentration based on characteristic molecular absorption signatures. Owing to the detector array's sensitivity from 1 to 5 µm wavelength, this demonstration lays the foundation for real-time versatile imaging of molecular fingerprint signatures across the infrared wavelength-regime with high-temporal resolution.

3.1 Introduction

Hyperspectral imaging extends traditional imaging approaches by providing detailed spectral information for each pixel in an image [113]. As a general method it has been employed with impressive success across scientific disciplines, including Earth remote sensing [114] and medical sciences [115]. Hyperspectral imaging instruments often rely on dispersive or filtering optics or scanning high-resolution spectroscopy. In such instruments, it can be challenging to achieve simultaneously fast real-time imaging and high-spectral resolution that is capable of resolving the narrow absorption lines of gases. Having the capability to rapidly image specific molecular species in real-time would unlock new opportunities for label-free bio-medical imaging, environmental monitoring or industrial applications, including leak detection, chemical process optimization and identification of hazardous substances. One attractive approach towards real-time and high-resolution imaging is combining dual-frequency comb spectroscopy[10, 11] with an imaging detector array [116, 117], where spatial and spectral multiplexing provides opportunities for rapid acquisition of high-resolution hyperspectral data without any moving mechanical parts.

Here, we demonstrate real-time dual-comb hyperspectral imaging of a narrow gas absorption feature with a high-frame rate uncooled lead-selenide (PbSe) 1-5 µm infrared detector array. The high 1 kHz frame rate of the detector permits heterodyne detection above the detector's technical flicker noise band and enables fast image acquisition. Hyperspectral images containing approximately 30 spectral channels in all 16'384 pixels are acquired at a rate of 10 Hz. Importantly, we show that the recorded data can be processed and gas concentration images can be derived in *real-time* by an artificial intelligence (AI) convolutional neural network (CNN) [118, 119, 120] on a personal computer. The AI-approach reduces the processing time by 4 orders of magnitude when compared to a conventional analysis and opens opportunities for real-time dual-comb hyperspec-

tral imaging.

3.2 Results

3.2.1 Concept

In dual-frequency comb spectroscopy [10, 11, 12, 13, 75], two optical frequency combs (1 and 2) are used. Each comb represents a well defined set of lasers lines spaced by their respective repetition rate $f_{\text{rep}}^{(1)}$ and $f_{\text{rep}}^{(2)} = f_{\text{rep}}^{(1)} + \Delta f_{\text{rep}}$ ($\Delta f_{\text{rep}} \ll f_{\text{rep}}^{(1,2)}$) with a relative central frequency offset $f_{\text{c}} \ll f_{\text{rep}}^{(1,2)}$ between both combs. Simultaneous photo-detection of both combs by a photo-detector results in a multi-heterodyne signal composed of interferograms, each with a duration of $\Delta f_{\text{rep}}^{-1}$. Fourier-transforming (at least one of) the interferograms yields the multi-heterodyne spectrum comprising beatnotes at frequencies $f_{\text{c}} + n \cdot \Delta f_{\text{rep}}$ ($n = 0, \pm 1, \pm 2, ...$). Effectively, the optical spectrum is compressed by a factor of $(f_{\text{rep}}^{(1)} + f_{\text{rep}}^{(2)})/(2\Delta f_{\text{rep}})$ and down-converted from the optical domain to multi-heterodyne frequencies around f_{c}. Dual-comb hyperspectral imaging is achieved when a dual-comb light source illuminates a sample and then is imaged on a 2-dimensional detector array where *each* pixel performs a multi-heterodyne detection[116]. In this way, massively multiplexed spatial and spectral information of the sample is simultaneously acquired at a high rate.

3.2.2 Experimental setup

In our setup, a dual-comb source with a central wavelength of 1536.7 nm illuminates a PbSe photo-detector array (Figure 3.1). The detector array is sensitive to light over the entire 1 to 5 μm wavelength range, which covers the characteristic spectral fingerprint domain of a large number of gas molecules. The array, consists of 128×128 pixels and can be read out with a maximal frame rate of 4 kHz. Between the dual-comb source and the detector, we arrange a series of small nozzles through which acetylene gas (C_2H_2) can be released, resulting in a jet of gas that is probed by the large diameter dual-comb beam. In this way, the spatial structure of the gas flow is projected onto the detector array, where the large number of pixels provides high spatial resolution and massively parallel acquisition.

Dense heterodyne encoding of spectral information in a given frequency interval requires dual-combs of high-mutual coherence (heterodyne beatnotes must be narrower than their frequency spacing Δf_{rep}). Such high-mutual coherence dual-combs have been demonstrated in the near- and mid-infrared based on mode-locked lasers, electro-optic modulation and optical parametric oscillators [76, 82, 83, 84, 86, 87, 85, 116, 117] . In this demonstration, two near-infrared-frequency combs are generated via electro-optic modulation [18] of a single continuous wave laser (see Supplement 1). Each comb consists of more than 30 comb lines spaced by $f_{\text{rep}}^{(1)} = 1$ GHz and $f_{\text{rep}}^{(2)} = f_{\text{rep}}^{(1)} + 10$ Hz respectively, so that narrow molecular absorption features (typical spectral width $\sim$10 GHz)
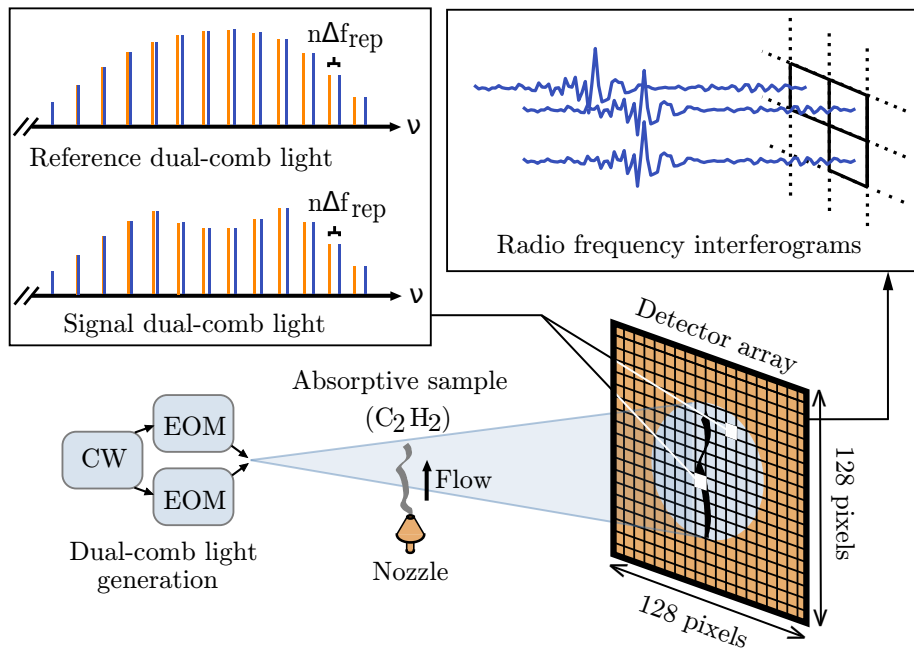
Figure 3.1: **Dual-comb hyperspectral imaging.** Dual-combs are generated by electro-optic modulation (EOM) of a single continuous (CW) wave laser. The dual-comb light is sent through a sample, here a flow of absorbing acetylene (C_2H_2) gas, and then detected by a high-frame rate near-to-mid-infrared detector array. Each pixel of the 128×128 detector array simultaneously digitises the dual-comb multi-heterodyne interferograms, which contain spectral information about the sample.

are well resolved and short acquisition duration down to $\Delta f_{\mathrm{rep}}^{-1} = 0.1$ s is possible. The relative central frequency offset Δf_{c} between both combs is chosen to be 250 Hz, so that all beatnotes are above 100 Hz. This choice is made possible by the detector's high-frame rate and avoids the frequency band below 100 Hz where uncooled PbSe detectors exhibit significant technical flicker noise (see Supplement 1). As all heterodyne beatnote frequencies are below 400 Hz, we operate the detector at a frame rate of 1 kHz, which could be increased to accommodate more spectral sampling points (i.e. more heterodyne beatnotes), without decreasing the acquisition rate.

3.2.3   Measurements

An example of several interferograms recorded by a *single* pixel of the detector array is shown in Figure 3.2a (after removal of low frequency components). Fourier-transformation of the raw interferogram trace yields the multi-heterodyne spectra, as shown in Figure 3.2b for different acquisition duration of 0.1 s, 1 s and 10 s (i.e. 1, 10 and 100 interferograms). The spectral envelope of the heterodyne beatnotes reflects the unabsorbed spectral envelope of the dual-combs. For the shortest acquisition time of 0.1 s (corresponding to 100 frames or a single interferogram), the spectral resolution of the heterodyne spectrum corresponds to the frequency spacing of the heterodyne beatnotes. Longer acquisition duration provide higher spectral resolution in the heterodyne spectrum and the heterodyne beatnotes show as narrow spectral peaks. As a higher spectral heterodyne resolution effectively rejects the incoherent white noise contribution, the signal-to-noise-ratio (SNR) of the heterodyne beatnotes grows proportionally with the square-root of the acquisition duration, which can however only be increased if the sample is evolving slowly. Importantly, already single-interferogram acquisition provides a useful SNR of approximately 10. Note that the high-mutual coherence of the combs would in principle permit longer acquisition durations [121], and phase-correction [77, 93, 28, 94, 95, 96, 97] can extend this well beyond 1000 s.

For a first test of hyperspectral imaging we probe the jet of C_2H_2 gas across the field-of-view. The dual-comb heterodyne signal is recorded for each pixel and Fourier-transformed to yield the heterodyne spectra. For each pixel, the transmittance of the dual-comb light on its specific path is obtained by normalizing the heterodyne spectrum by an unabsorbed reference heterodyne spectrum. In our case, the reference heterodyne spectrum is derived from 9 pixels in the top left corner of the detector (where essentially unabsorbed comb light is detected). Alternatively, a pre-recorded reference spectrum may be used. An example of the transmittance signature recorded by a single pixel is shown in (Figure 3.2c) for a 10 second long acquisition, showing very good agreement with the HITRAN database [91, 92] (residuals below 3%). Note that the instrument function is well approximated by a zero-width delta-function (width of a comb line and comb line separation at least 6 orders of magnitude narrower than the absorption feature). In addition, standard-error bands for shorter acquisition duration (0.1 s and 1 s) are shown, indicating that absorption on the
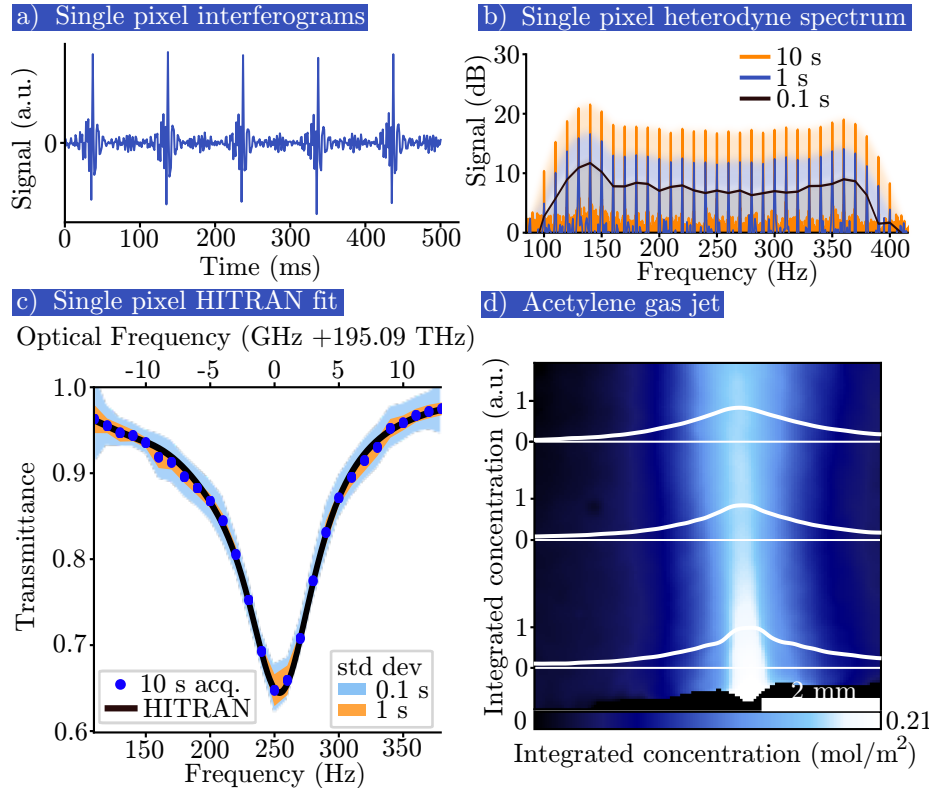
Figure 3.2: **Raw interferograms, spectrum, single-pixel transmittance spectrum, comparison with HITRAN and integrated concentration image. a.** Raw and unabsorbed dual-comb multi-heterodyne interferograms as recorded by a single pixel. **b.** Multi-heterodyne spectra obtained by Fourier-transforming the raw interferograms for different acquisition durations (10 s in orange, 1 s in blue, 0.1 s in black). **c.** Single pixel dual-comb absorption spectrum of acetylene (C_2H_2) retrieved from a 10 seconds acquisition (blue dots) compared to a HITRAN model (black line). The standard deviation of the absorption spectrum for acquisition times of 0.1 and 1 second is shown in light-blue and orange bands (centered around the 10 second based data points). **d.** Reconstructed integrated concentration image of an acetylene gas flow obtained by fitting a HITRAN model to the recorded transmittance for each pixel. Transverse absorption profiles are shown for three different positions along the gas flow (white curves).

few-percent level can already be detected based on single interferograms.

A natural measure for the number of absorbing molecules is their integrated concentration along the light path (cf. Supplement 1), which can be retrieved from a fit to a HITRAN model. It is computed for each pixel based on the 10 second recording (100 interferograms) and shown in (Figure 3.2d). The gas jet is imaged based on its infrared absorption signature, allowing retrieval of integrated concentrations as small as 0.015 mol/m^2. Profiles of the integrated concentration for different heights of the gas flow show a transverse expansion of the gas jet along its flow direction. While in our case only one gas species is imaged, the analysis can readily be generalized to multiple gas species.

Figure 3.2d demonstrates that hyperspectral imaging with the near-to-mid-infrared detector array is possible. However, the high data rate of approximately 35 MB/s and the necessity of performing the analysis on each pixel requires large memory size and result in long computations times, in our case 20 to 30 minutes on a desktop computer for one frame. Overcoming this data processing bottleneck is crucial in applications demanding fast feedback, such as leak detection, chemical process monitoring or bio-medical imaging.

3.2.4 AI based data processing

To reduce the data processing time we explore an AI based approach that bypasses the conventional analysis: A convolutional neural network (CNN) is used that *directly* processes the temporal interferograms. It is implemented using the Keras library running on a Tensorflow backend [122]. The response of the CNN is invariant against translation of the input data along the time axis; a dedicated trigger or temporal alignment of the input interferogram is therefore not required (any input of a duration of $\Delta f_{\mathrm{rep}}^{-1}$ is suitable). This property of CNN greatly simplifies the data analysis and results in better versatility (i.e. applicability to unknown data) compared to densely connected networks with a comparable number of parameters. The detailed architecture of the CNN is described in Supplement 1. While the capability of neural networks for fast data processing is widely recognized [123, 124, 125], the difficulty of obtaining a reliable *labelled* training data set (containing training input data as well as the correct analysis outcome) is often prohibitive to their use. Here, a training data set is rapidly built owing to the large amount of data generated by the setup. The details of this data set and its use in training the neural network are described in Supplement 1. Statistically, the trained CNN-based analysis differs by less than 3% of the maximum integrated concentration value from the results obtained through conventional analysis. As one can intuitively expect, a detailed analysis of the CNN's first layer weights shows that the CNN learns to focus its 'attention' on the heterodyne frequency components that encode the absorbed dual-comb frequencies (see Supplement 1).

To test the CNN's performance, we observe the dynamics when the gas flow is turned on. The multi-heterodyne data of each pixel are processed for each 100 ms time window (single interferogram), so that good temporal resolution is achieved. From the series of reconstructed gas images, three snapshot frames,
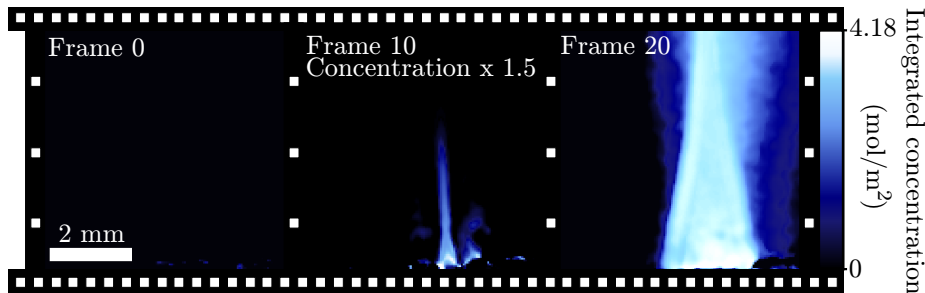
Figure 3.3: **AI-based imaging.** Three selected frames from a movie (cf. Visualization 1) that has been reconstructed in real-time by the neural network (frame rate 10 Hz). The frames show the dynamics of the C_2H_2 gas jet and are separated by 1 s each. The first frame is recorded before the gas jet is turned on, the second frame depicts the onset of gas emission and the last frame shows the established gas jet.

separated in time by 1 s, are shown in Figure 3.3. In frame 0 no C_2H_2 gas was released, in frame 10 the gas jet is emerging from one out of several nozzles, and in frame 20 the gas jet from several nozzles is fully developed. The results in Figure 3.3 show that the CNN can reliably work on single-interferograms (0.1 s acquisitions), permitting the observation of dynamic processes (also see Visualization 1). Importantly, the trained CNN can process the data at a rate that exceeds the raw data recording rate, therefore enabling *real-time* molecule specific imaging with a frame rate of $\Delta f_{\text{rep}}^{-1} = 10$ Hz. The CNN also alleviates the need for large memory storage by reducing the heterodyne raw data frame rate from 1000 down to 10 frames per second for the gas images. If desired, the neural network could be trained to output other parameters e.g. gas temperature (based on line shapes) or be extended to multi-species imaging by adding outputs on the last layer and adjusting the training accordingly.

3.3 Discussion

In summary, we have shown that real-time dual-comb hyperspectral imaging can be performed with a near-to-mid-infrared photo-detector array enabling imaging of a gas with molecular specificity based on its fingerprint absorption signature. Hyperspectral data has been simultaneously recorded in 16'384 pixels with 30 spectral channels and short acquisition times of 100 ms enabled observation of dynamic phenomena. Key to this demonstration is the high-frame rate of the detector array as well as the high-mutual coherence of the dual-comb illumination, which permits recording the heterodyne signal in a frequency band (here above 100 Hz) that does not suffer from technical low-frequency flicker noise. Hundreds of spectral channels could be implemented without reducing the acquisition rate by utilizing a higher detector frame rate. Importantly, we have

also shown that the high-data rate resulting from the massively parallelized hyperspectral data acquisition can be processed in real-time by a convolutional neural network, providing gas concentration images at 10 Hz rate. Built on direct processing of time-domain interferograms, this method adds to the AI toolbox for spectroscopy [126, 127, 128, 129, 130] and can readily be applied to other dual-comb spectroscopy schemes. As the detector array is sensitive across the entire 1 to 5 μm wavelength range, our demonstration can be extended to cover the characteristic molecular absorption fingerprints of a wide range of molecular species. Possible extensions of our demonstration include the use of high-repetition rate mid-infrared quantum cascade [102, 103], mid-infrared microresonator [131, 132] or mid-infrared electro-optic combs [133] for broadband spectral imaging of transparent condensed phase samples.

3.4 Supplementary information

Below is a supplemental document published alongside this Letter for additional information.

3.4.1 Dual-frequency comb source

The near-infrared dual-frequency combs are generated via electro-optic modulation [18] in a polarisation-maintaining fibre-based setup. A wavelength-tunable, free-running continuous wave (CW) laser is split into two parts from each of which a comb is derived; this method ensures high-mutual coherence between both combs. After splitting, the CW laser's frequency is shifted via acousto-optic modulation by 80 MHz and 80 MHz $+ \Delta f_c$ respectively, creating a relative frequency offset Δf_c between the centre frequencies of both combs. Next, optical combs with approximately 30 lines are generated from the shifted CW laser lines by electro-optic modulation [121]. As all modulation sources are referenced to a common 10 MHz clock, high-mutual coherence is readily achieved between both combs (heterodyne beatnote width < 10 mHz). By tuning the CW laser, the combs' central wavelength is chosen to coincide with an absorption line of C_2H_2 gas ($\sim$1536.7 nm; peak molar attenuation coefficient of $4.88 \cdot 10^{-21}$ cm$^2 \cdot$molecule^{-1}).

3.4.2 Detector noise

Analysis of the detector array's noise spectrum (Figure 3.4) reveals prohibitively high technical flicker noise at low frequencies (below 100 Hz), including in particular pixel dark-value fluctuations. However, following the idea of lock-in detection, the high frame-rate of the detector array provides access to a higher frequency band for heterodyne beatnote detection above 100 Hz that exhibits significantly lower noise. We therefore aim to arrange all heterodyne beatnotes above 100 Hz, thereby overcoming the challenge of low-frequency flicker noise.
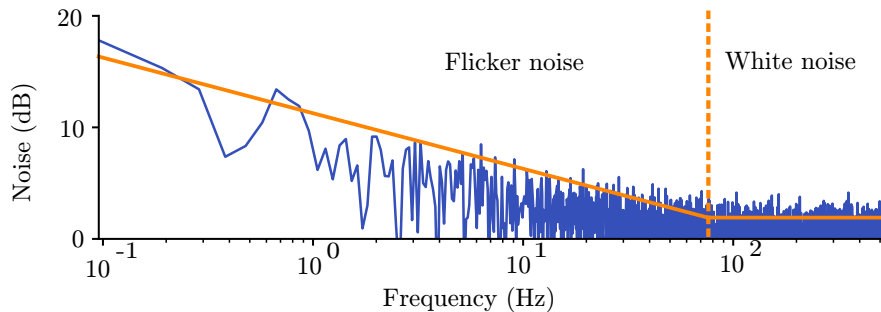
Figure 3.4: **Detector noise.** Single pixel noise spectrum of the near-to-mid-infrared detector array.

3.4.3 Integrated concentration

To image the spatial distribution of the C_2H_2 gas, the *integrated concentration* of C_2H_2 molecules along the light path is derived for each pixel. Generally, the absorption of light propagating through a sample is described by the Beer-Lambert law

$$\frac{dI(\nu, l)}{I(\nu, l)} = -c(l) \cdot m(\nu) \cdot dl, \tag{3.1}$$

where I is the intensity, ν is the optical frequency, l is the spatial coordinate along the beam path, m is the molar absorption coefficient and $c(l)$ the molar concentration of gas. Integrating both sides along the path from the dual-comb source to the detector array yields

$$T(\nu) = \frac{I_d(\nu)}{I_0(\nu)} = \exp\left(-m(\nu) \int_0^L c(l) dl\right), \tag{3.2}$$

where $T(\nu)$ is the measured transmittance (Main Text Figure 3a), L is the distance between the dual comb source and the detector array, $I_d(\nu) = I(\nu, L)$ is the intensity at the detector array and $I_0(\nu) = I(\nu, 0)$ is the intensity before absorption. A natural measure of the number of absorbing particles traversed by the beam is then defined as

$$C_{\text{int}} = \int_0^L c(l) dl. \tag{3.3}$$

In traditional gas cell spectroscopy, where the concentration is homogeneous and the path length is known, this integral can be carried out explicitly. In this experiment, the spatial distribution of the gas is unknown, and only the integrated concentration is measured.

3.4.4 Neural network architecture

To avoid any unnecessary processing, the CNN directly takes a single amplitude-normalised interferogram (100 temporal sampling points) as an input (Fig-

40

ure [3.5](#)a). The first convolutional layer uses periodic boundary conditions, and uses a kernel size equal to the size of the input. In our case, we found that 8 filters on the first layer were sufficient (extracting 800 features), however, more filters can readily be added to extend the CNN's capabilities to analyse different gas species and mixtures thereof. Each subsequent layer has a kernel size (approximately) divided by two and a doubled number of filters, such that the number of processed features remains constant throughout the layers. Each layer's activation function was chosen to be the rectified linear unit [134], as it gave the best performances among a few test functions. The last layer directly provides the scalar integrated concentration value. This neural network architecture allows skipping both Fourier transformations as well as time-consuming fitting of absorption profiles. The rapid and massively parallel recording capability of the system allows building large data sets for training such that regularisation layers [135] to prevent over-fitting are not necessary.

3.4.5   Neural network training

A training data set is rapidly built by sending the dual-combs through a 10 cm gas cell filled with an acetylene-nitrogen mixture (all light traverses the cell). Multiple segments, each of 10 seconds duration, for 180 different integrated concentrations, ranging from 0 to a maximal integrated concentration C_{int} of 4.16 mol·m^{-2} are recorded of over the full range of values for C_{int} (in total approximately 300 million interferograms are recorded within 30 minutes). In order to label each interferogram, i.e. assign to it one of the 180 possible values of C_{int}, the integrated concentration for each 10 seconds data set is derived as described in the Main Text via HITRAN fitting. The signal of all pixels is combined for better precision in the derivation of the integrated concentration label. Approximately $2 \cdot 10^6$ interferograms (equivalent recording time of only 12 s) from the training data set are randomly selected for training and validation of the CNN (training and validation are performed with different data). The training proceeds over 100 epochs and, on a desktop computer with a standard graphics processing unit, takes approximately 8 hours. A decreasing learning rate divided by 2 every 10 epochs is used to improve the convergence of the learning process (cf. Figure 2b).

3.4.6   Neural network first layer weights

To gain insight into the analysis performed by the neural network, it is interesting to look at the weights of the first layer (i.e. the convolution kernels). As an example, Figure [3.6](#)a shows two of the eight 100×1 kernels, each representing a modulated waveform, similar to those one could expect in a multi-heterodyne measurement. An intuitive understanding of these kernels can be obtained by considering their spectral content. Figure [3.6](#)b shows the Fourier-Transformation of the kernels and reveals that the kernels most prominently include the frequency components where acetylene absorption can be observed. The shaded background represents the envelope over all kernels indicating that
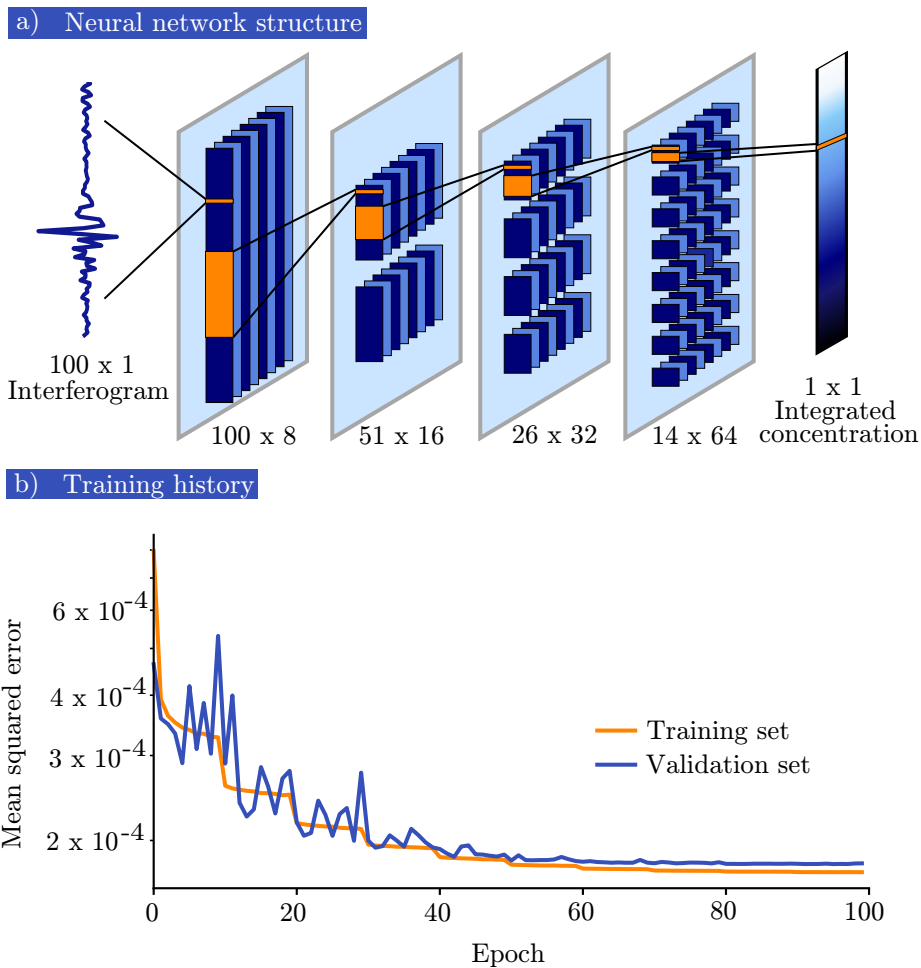
Figure 3.5: **Neural network architecture and training history. a.** A single 100 point interferogram is used as input for the convolutional neural network. A first layer with periodic boundary conditions and 8 filters extracts 800 features from the input. Approximately reducing the Kernel width by a factor of two and doubling their number in each subsequent layers keeps the number of features constant across the network. The last layer outputs the scalar integrated concentration value. **b.** Training history of the network, achieving a standard deviation of 1.3 % of the maximal integrated concentration with regard to the validation data set.
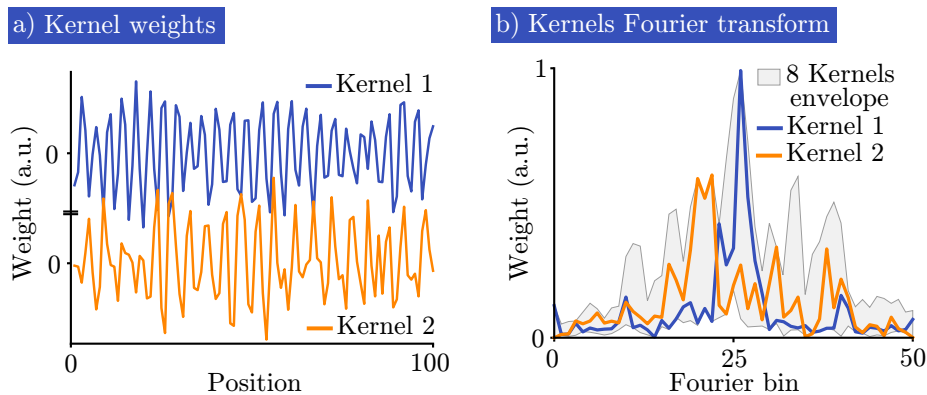
Figure 3.6: **CNN's first layer weights and spectrum. a.** Weights value for two out of the eight kernels in the first layer of the CNN. **b.** Fourier transform of the weights of two kernels in the CNN's first layer and envelope over all eight Fourier transformed kernels in light grey.

the neural network is extracting information from the absorption feature and neglecting information from the wings of the spectrum where absorption is weak and noise dominates the data. Further analysis of the first layer kernels shows that they form an almost orthogonal basis (i.e. they have small scalar cross-products). Thus the first layer projects the 100-dimensional input onto an 8-dimensional subspace that represents the most significant features, which are then further interpreted by the following layers.

Chapter 4

1 GHz dual-comb spectrometer with high mutual coherence for fast and broadband measurements

Thibault Voumard[1], **John Darvill**[1], **Thibault Wildi**[1], **Markus Ludwig**[1], **Christian Mohr**[1], **Ingmar Hartl**[1], **Tobias Herr**[1,2]

[1] *Deutsches Elektronen-Synchrotron DESY, Notkestr. 85, 22607 Hamburg, Germany*
[2] *Physics Department, Universität Hamburg UHH, Luruper Chaussee 149, 22761 Hamburg, Germany*

Context

To leverage the full optical bandwidth advantage of high mutual coherence, high repetition rate dual-comb spectroscopy, a dual-comb spectrometer based on 1 GHz mode-locked lasers is designed and built. Compared to the previously used electro-optic dual-comb system, short pulse duration and higher peak powers render spectral extension feasible. At the same time, high mutual coherence is harder to establish, as it is not natively inherited from a single pump source. This new dual-comb spectrometer achieves second-scale coherence times and is used to demonstrate fast and broadband spectroscopy of narrow absorption features. Additional details of the setup design and components are given in Appendix A, while general technical details for data acquisition and processing in dual-comb spectroscopy are given in Appendix B.

Author contribution

The author conceived and built the setup and conducted the data acquisition and data analysis. The author and T. Herr jointly wrote the manuscript.

1 GHz dual-comb spectrometer with high mutual coherence for fast and broadband measurements

Dual-frequency comb spectroscopy permits broadband precision spectroscopy with high acquisition rate. The combs' repetition rates as well as the mutual coherence between the combs are key to fast and broadband measurements. Here, we demonstrate a 1 GHz high-repetition rate dual-comb system with high mutual coherence (sub-Hz heterodyne beatnotes) based on mature, digitally-controlled, low-noise erbium-doped mode-locked lasers. Two spectroscopy experiments are performed with acquisition parameters not attainable in a 100 MHz system: detection of water vapor absorption around 1375 nm, illustrating the potential for fast and ambiguity-free broadband operation, as well as acquisition of narrow gas absorption features across a spectral span of 0.6 THz (600 comb lines) in only 5 μs.

4.1   Introduction

Dual-frequency comb spectroscopy (DCS) uses detection of multiheterodyne interferograms between two frequency combs with slightly different pulse repetition rates for coherent mapping of an optical spectrum to the radio frequency (RF) domain [10, 11, 12, 13, 76, 136, 81, 44, 43, 9]. This method can offer both broadband spectral coverage and rapid acquisition, ultimately limited by the Nyquist criterion

$$\Delta\nu \leq \frac{f_{\mathrm{r}}(f_{\mathrm{r}} + \Delta f_{\mathrm{r}})}{2\Delta f_{\mathrm{r}}}, \tag{4.1}$$

where $\Delta\nu$ is the maximal optical bandwidth that can be mapped without ambiguity from the optical to the RF domain, f_{r} is the repetition rate of one comb and Δf_{r} is the repetition rate difference between the two combs.

Broadband dual-comb spectroscopy [31, 86, 77] can thus be achieved in two ways: reducing Δf_{r}, or increasing f_{r}. The first approach has been pursued in dual-comb systems with high mutual coherence [85, 83, 137, 82, 88, 89] with Δf_{r} as low as a few Hertz.

The second approach, i.e. increasing f_{r}, is attractive due to the favorable quadratic scaling of $\Delta\nu \propto f_{\mathrm{r}}^2$. Moreover, the maximal acquisition rate for one full optical spectrum (one full, untruncated interferogram) is given by Δf_{r}. Hence, for a fixed optical bandwidth $\Delta\nu$, a higher repetition rate increases the maximal full-interferogram acquisition rate quadratically.

Further, the signal-to-noise ratio (SNR) also scales with f_{r} for a given spectral bandwidth as the optical power is distributed among fewer comb lines [43]. The trade-off resulting from a higher repetition rate is a reduction in the density of spectral sampling points. However, a 1 GHz repetition rate (i.e. a comb line spacing of 1 GHz) is sufficient to adequately sample even narrow gas absorption features at atmospheric pressure. Alternatively, the number of spectral sampling points can be increased by scanning the combs' repetition rates or offset frequencies at the cost of longer measurement time [103, 138].
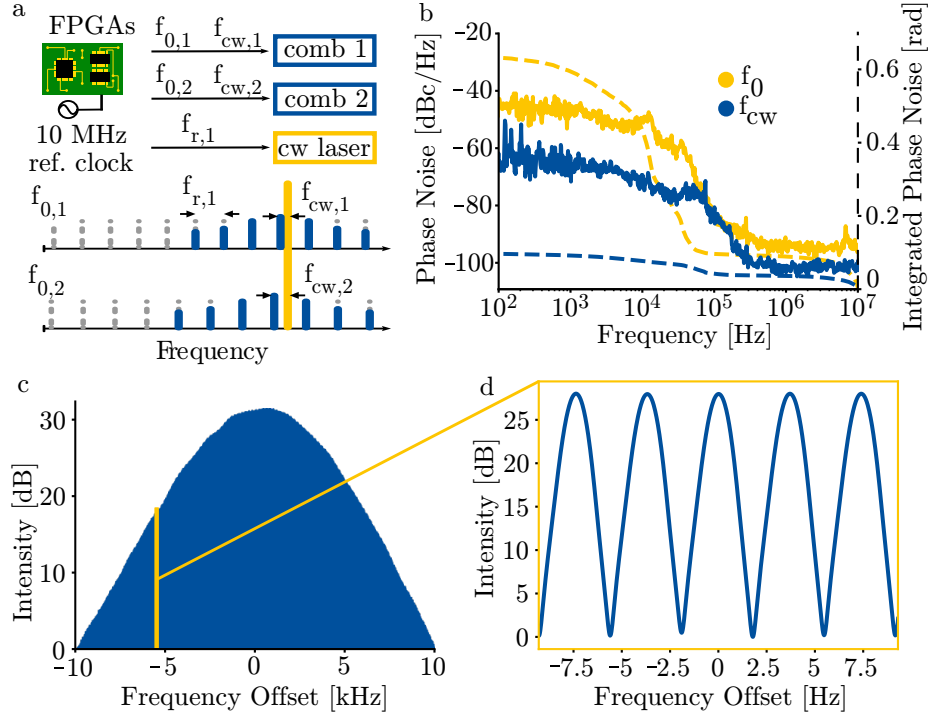
Figure 4.1: **Experimental setup and mutual coherence. a** Schematic of the field programmable gate array (FPGA)-based digital locking scheme for a high mutual coherence, fully self-referenced dual-comb spectrometer. One line of each comb is phase locked to a continuous-wave (CW) laser (beatnotes $f_{CW,1,2}$). The CW laser's frequency is controlled to keep the repetition rate of comb 1 $f_{r,1}$ stable to a radio frequency reference (10 MHz clock). Both carrier envelope offset frequencies $f_{0,i}$ are directly stabilized to the frequency reference. **b** Residual phase noise power spectral density (solid curves) and phase noise integrated from 10 MHz (dashed curves) for phase lock between a comb and the CW laser (blue, offset frequency $f_{CW,1} = 250$ MHz) and carrier envelope offset phase lock (yellow, offset frequency $f_{0,1} = 390$ MHz). **c** radio frequency multi-heterodyne spectrum obtained by mixing the stabilized combs on a photodetector. The zoom-in **d** shows individual multiheterodyne beatnotes spaced by $\Delta f_r \sim 4$ Hz with a 1 Hz resolution-bandwidth-limited linewidth, recorded by a real-time electrical spectrum analyzer.

High-repetition rate dual-comb systems are more challenging to implement than their lower repetition rate counterparts due to lower pulse peak power. Previous demonstrations of high-repetition rate combs often relied on electro-optic combs [139, 140, 141, 121] where GHz-repetition rates are readily available but spectral broadening is difficult. In contrast, microresonator-based combs can achieve extremely high repetition rate and broadband spectral coverage but only provide very coarse spectral sampling [110]. Previous work with mode-locked lasers includes narrowband spectroscopy with Ytterbium-doped 1 GHz fiber-laser [142] and 1 GHz Titanium-Sapphire lasers for dual-comb Raman spectroscopy [143]. Recently, a 1 GHz dual-comb system based on cavity-filtered 100 MHz erbium-doped fiber lasers has been implemented [144], acquiring a 750 GHz wide spectral span in only 11 μs highlighting the potential of high-repetition rate mode-locked laser systems. Similarly, a time-interleaved 100 MHz-based system has been demonstrated, acquiring in 40 μs a 3.1 THz wide spectrum [145]. Although not yet reaching large spectral span, entirely chip-integrated 1 GHz dual-combs have been demonstrated highlighting the potential for low-cost and widespread use of such systems [146]. The general interest in fast spectroscopy is also evidenced by efforts in Fourier transform spectroscopy where fast, resonant mechanical scanners can be used to achieve acquisition rates of up to 24 kHz. [147].

Here, we demonstrate a 1 GHz dual-comb spectrometer with high mutual coherence (sub-Hz multiheterodyne beatnote width) based on mature erbium-doped solid-state mode-locked lasers. We show a broadband spectral window without ambiguity in the optical-to-RF frequency mapping as well as fast spectroscopy with μs-scale full-interferogram acquisition time, both in regimes not attainable in a 100 MHz-based system. All feedback loops are implemented via a compact, flexible and easy to operate FPGA-based digital locking scheme [148, 149, 150].

4.2 Results

4.2.1 Setup

The dual-comb spectrometer builds upon two commercially available low-noise solid-state 1 GHz mode-locked lasers (Menhir Photonics) with tunable repetition rate and offset frequency, and with a center wavelength of 1560 nm. The combs are amplified to $\sim$900 mW of average optical power and broadened to an octave-spanning supercontinuum in a highly-nonlinear fiber (HNLF) supporting the formation of a Raman soliton. The combs' carrier-envelope offset frequencies are detected through f-2f interferometers (similar to ref. [151]) and stabilized to a 10 MHz RF standard by modulation of the pump currents. High mutual coherence between both comb sources is achieved by phase-locking one line of each comb to a 1560 nm continuous-wave (CW) fiber-laser ($\sim$10 kHz linewidth) via piezo-actuators. To achieve absolute frequency calibration, the repetition rate of one comb $f_{r,1}$ is detected and the CW laser's frequency (to

which the combs are locked) is controlled to stabilize $f_{r,1}$ with respect to the same 10 MHz RF reference. This implies that also the CW laser's frequency as well as the repetition rate of the second comb are also stabilized and linked to the RF reference. In total, these five phase locks yield fully self-referenced dual-frequency combs with high mutual coherence (Fig. 4.1a).

All phase-locked loops are digital and implemented via inexpensive, compact field-programmable gate arrays (FPGAs). The boards are programmed through the open-source python package *pyrpl* [150], replacing traditional mixers, phase and frequency counters, function generators, filters and locking modules used in analog implementations. Through a minor hard- and software modification, an external 10 MHz RF reference can be directly fed to the FPGA, providing intrinsic low-noise synchronization (the FPGA clock is generated via an internal phase-locked loop). Besides its low complexity, the digital locking scheme readily enables completely autonomous startup of the system and dynamic modification of the combs' parameters. The residual phase-noise of the beatnote between one comb and the continuous wave laser as well as the residual phase noise of one of the carrier-envelope offset frequencies are shown in Fig. 4.1b. Their respective integrated residual phase noise are ~ 70 mrad and ~ 620 mrad, integrated from 10 MHz to 100 Hz. Notably, this compact digital approach achieves a lock quality comparable to stabilization with analog electronics in a similar laser [151].

4.2.2 Mutual coherence

The combs' high mutual coherence manifests itself in narrow radio frequency multiheterodyne beatnotes as shown in Fig. 4.1c,d. In this example, the beatnotes are spaced by $\Delta f_r \sim 4$ Hz and their apparent 3 dB-linewidth of 1 Hz is only limited by the resolution bandwidth of the recording real-time electrical spectrum analyzer (showing a power Fourier transform). This sub-Hz mutual coherence permits a $> 10^9$ compression factor from optical to radio frequency domain, providing the basis for a one-to-one mapping from optical to radio frequency domain over hundreds of THz. The spectral coverage is then only limited by the multiheterodyne detector and the spectral bandwidth of the combs. On the other hand, achieving a high compression factor enables the use of low-bandwidth heterodyne detectors, as recently demonstrated in dual-comb hyperspectral imaging [116, 141] and photoacoustic dual-comb spectroscopy [121, 112].

4.2.3 Broadband spectroscopy

As described in the introduction, one advantage of a high-repetition DCS system is the ability to unambiguously map an optical spectrum to a RF multiheterodyne spectrum while maintaining rapid acquisition speed. To demonstrate these characteristics, in a first experiment, a 70 THz wide spectrum (1.3 to 1.9 μm) is generated from each frequency comb in two normal-dispersion HNLFs (Fig. 4.2a). Here, $\Delta f_r \approx 3$ kHz is set, which would in principle permit

to cover an even wider span (> 160 THz), whereas in a 100 MHz system the maximal spectral span would only be ~ 1.6 THz. Both broadband comb spectra traverse ~ 10 cm of laboratory air where they experience absorption by water vapor before being short-pass filtered and combined on a 2 GHz InGaAs photodiode. As the used InGaAs-photodetector is not sensitive at wavelengths above ~ 1800 nm where pronounced water vapor absorption features are present, we recorded the weaker absorption features at ~ 1375 nm to validate the dual-comb signal. Figure 4.2b shows a 4 THz wide section of the measured transmittance based on the direct multiheterodyne signal. The high-mutual coherence permits recording the dual-comb multiheterodyne spectrum directly via an RF-spectrum analyzer (in ~ 10 s), bypassing any need for large storage and complex post-processing of the data; only a generic (high-pass) baseline correction is applied. Further, the retrieved absorption spectrum is in excellent agreement (0.01 RMS deviation) with the HITRAN database (transmittance modeled via HAPI) [92, 91].

4.2.4 Fast spectroscopy

In a second experiment, we perform spectroscopy of acetylene gas with μs-scale full-interferogram acquisition time. Here, the repetition rate difference is set to $\Delta f_r = 215$ kHz, corresponding to a minimal, full-interferogram acquisition time of ~ 5 μs. From the Nyquist criterion, a maximal optical bandwidth of ~ 2.3 THz can be covered without ambiguity, while a 100 MHz-based spectrometer would only accommodate a ~ 23 GHz span. The dual-comb signal is optically bandpass filtered to cover a 600 GHz spectral span containing absorption features of acetylene, ensuring multi-heterodyning to the RF domain well within the Nyquist constraint. The dual-comb light is sent through a 10 cm long acetylene absorption cell at atmospheric pressure and collected on a 2 GHz InGaAs photodiode. The temporal series of the multiheterodyne interferograms recorded with an oscilloscope can be seen in Fig. 4.3a along with a magnified single interferogram. A reference trace is obtained in the same experiment without acetylene in the cell. Using auto-correlation to locate the interferogram bursts, the interferogram series is interpolated to ensure an integer number of sampling points per interferogram. Single interferograms are then isolated and Fourier transformed, and the absolute value is taken to obtain positive real-valued single-interferogram spectra. Based on ~ 4300-interferograms for the absorption and reference signal an averaged transmittance spectrum can be computed and is shown in Fig. 4.3b. Comparison with the HITRAN database shows good agreement (0.058 RMS deviation) apart from weaker oscillatory features from a parasitic cavity in the optical beam-path. The averaged spectrum enables us to compute a standard deviation from this average for spectra retrieved from only single interferograms. This standard deviation is small compared to the absorption features and indicates that already single full-interferograms acquired at a rate of 215 kHz (i.e. 215'000 spectra per second, time resolution $< 5\mu s$) suffices to clearly identify acetylene based on its characteristic absorption features. The signal-to-noise figure of merit [43] was found to be 5×10^5 Hz$^{-1/2}$ to
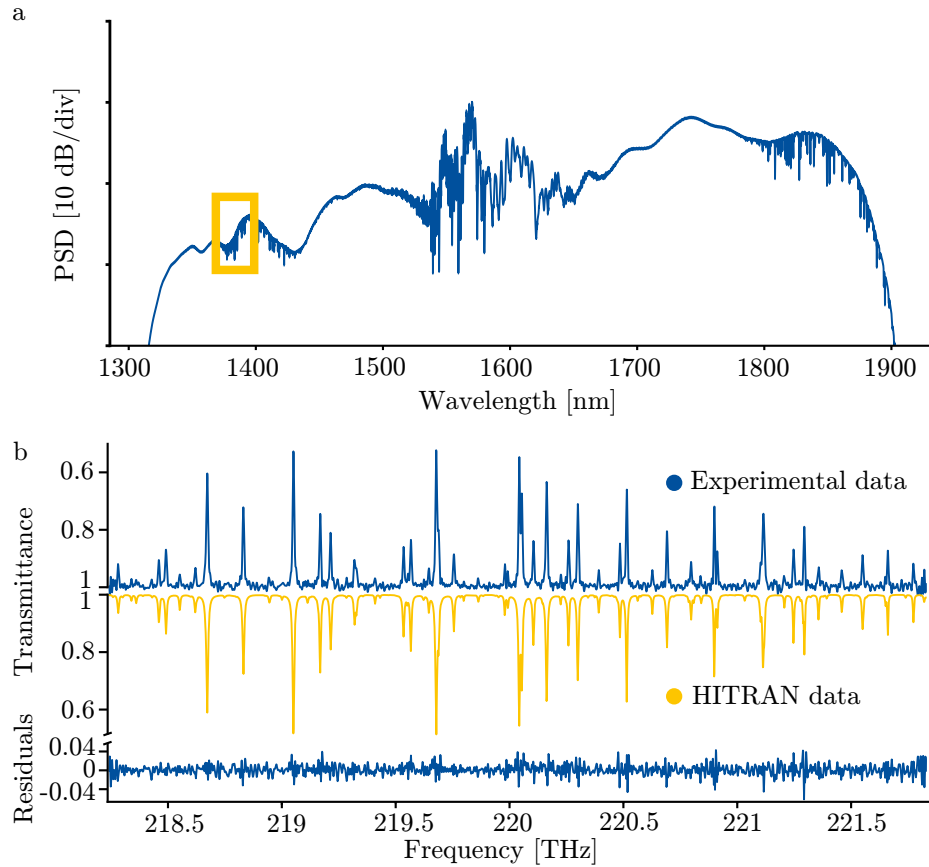
Figure 4.2: **Broadband spectroscopy.** **a** Broadband spectrum generated in normal-dispersion highly-nonlinear fiber used to perform water vapor spectroscopy around 1375 nm (yellow box). The spectrum is recorded by a grating-based optical spectrum analyzer with resolution bandwidth of 0.2 nm. PSD: Power spectral density. **b** Experimental reconstruction of water vapor absorption features over 4 THz (blue). Comparison with the HITRAN database (yellow) via HAPI shows small residuals (0.01 RMS deviation).
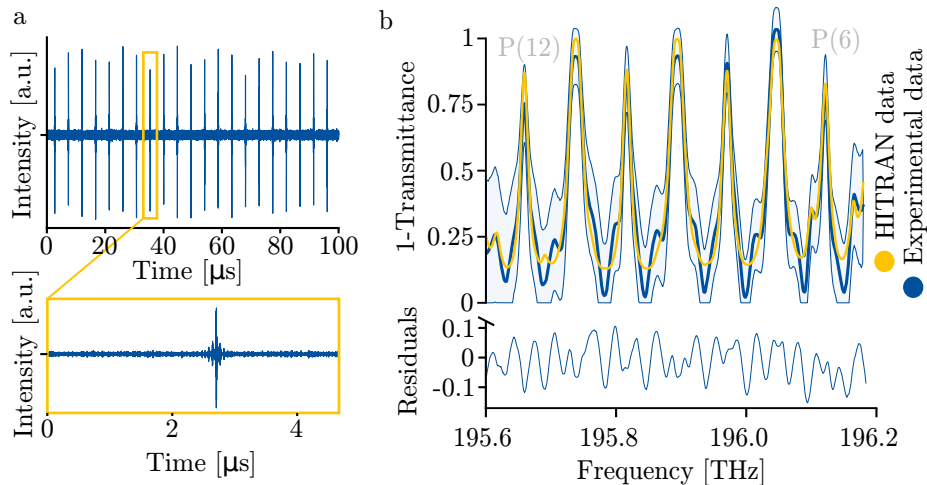
Figure 4.3: **Fast spectroscopy. a** Recorded series of interferograms generated with a ~ 215 kHz repetition rate difference and zoom-in on a single, ~ 4.6 μs total duration single interferogram. **b** Acetylene absorption features (P branch, lines 6 to 12) computed from HITRAN/HAPI (yellow). The light blue band represents the standard deviation of the experimentally retrieved spectra derived from individual single-interferograms, the darker blue line their mean (based on 4300 single interferogram spectra).

5×10^6 Hz$^{-1/2}$ for detectors with nominal bandwidth of 1 GHz and 125 MHz, respectively. Finally, we point out that operating with short acquisition times can improve noise performance as low-frequency noise below $\Delta f_\mathrm{r}/2$ does not affect single interferograms. In particular the negative impact of the usual oscillator noise in the ≤ 100 kHz frequency band can be elegantly reduced when a high $\Delta f_\mathrm{r} \geq 200$ kHz is used. Moreover, a large $\Delta f_r/2$ will also improve the efficacy of phase noise correction techniques[94, 28, 93, 40], which can lower noise with frequencies up to $\Delta f_r/2$.

4.3   Conclusion

A 1 GHz dual-frequency comb spectrometer with high mutual coherence for fast and broadband measurements based on mature erbium-doped mode-locked lasers is demonstrated. All feedback loops are implemented digitally, resulting in a compact and easy to operate setup that can readily be reconfigured. In comparison to a dual-comb spectrometer based on 100 MHz lasers, this represents a 100-fold improvement in the Nyquist criterion for the maximal spectral coverage or the full-interferogram acquisition rate. Two experiments are performed to demonstrate dual-comb characteristics that would not be possible with lower-repetition rate ($\sim$100 MHz) lasers: first, the potential for achieving

a broadband ambiguity-free spectral window is illustrated by performing spectroscopy of atmospheric water absorption features near 1375 nm over 4 THz with a $\Delta f_{\rm rep} = 3$ kHz. The high-mutual coherence with sub-Hertz multiheterodyne beatnotes also generates opportunities for broadband spectroscopy with low-bandwidth detectors (e.g. imaging, photo-acoustic or mid-infrared detectors). Second, fast spectroscopy of acetylene is performed over a 600 GHz wide optical span with a full-interferogram acquisition time of 5 μs, pointing towards opportunities for observing fast transients e.g. in high-throughput screening, flow-cytometry or plasma physics [152, 153, 154, 42, 155]. Similar to dual-comb spectroscopy, the high-repetition rate of 1 GHz is also of interest for infrared-field sampling techniques [25] where it can speed up the measurement and relax the requirement on the lasers' noise.

Chapter 5

Dual-frequency comb assisted astronomical spectrograph calibrator

Thibault Voumard[1], **Thibault Wildi**[1], **Markus Ludwig**[1], **François Bouchy**[2], **Tobias Herr**[1,3]

[1] *Deutsches Elektronen-Synchrotron DESY, Notkestr. 85, 22607 Hamburg, Germany*
[2] *Observatoire de Genève, Département d'Astronomie, Université de Genève, Chemin Pegasi 51b, 1290 Versoix, Switzerland*
[3] *Physics Department, Universität Hamburg, Luruper Chaussee 149, 22761 Hamburg, Germany*

Context

The high mutual coherence dual-comb spectrometer provides a path towards broadband, precise spectroscopy at high signal-to-noise ratios. Building on these strong assets, a novel technique for the calibration of astronomical spectrographs is presented. The dual-comb spectrometer is used to precisely and accurately measure the optical transmission of an astronomical Fabry-Pérot cavity over a broad bandwidth with short acquisition times. This permits linking the frequencies of the cavity modes to the SI standard and calibration of astronomical spectrographs with comb-accuracy and precision, without the need for astro-combs.

Author contribution

The author conceived and built the setup and conducted the data acquisition and data analysis. The author and T. Herr jointly wrote the manuscript.

Dual-frequency comb assisted astronomical spectrograph calibrator

Astronomical precision spectroscopy can support searches for Earth-like habitable exoplanets, observation of the Universe's expansion and searches for potential variability of fundamental physical constants. It critically relies on accurate and precise calibration of the astronomical spectrograph. Fabry-Pérot cavities have been established as robust and mature calibrators, which are however limited by their complex spectral characteristics and variability. In contrast, high-repetition rate laser frequency combs ('astrocomb') can provide SI-referenced accuracy and precision, however, they remain challenging to generate, costly and have high-maintenance requirements. Here, we explore a novel calibration technique that combines the robustness of Fabry-Pérot-based calibration with the precision and accuracy of laser frequency combs, however, without the need for high pulse repetition rate. Specifically, we utilize low-repetition rate dual-frequency comb lasers to rapidly measure and track the resonances of a Fabry-Pérot cavity, which we estimate in a proof-of-concept experiment covering 300 nm of spectral span (1450-1750 nm) could in principle already support spectrograph calibration on the 25 cm/s scale, comparable to levels needed for the search of habitable planets.

5.1   Introduction

Optical precision spectroscopy of astronomical objects provides a unique window into the cosmos. It has led to the Nobel-Prize winning discovery of the first planet orbiting around a star outside our Solar system, which was identified by the minute periodic Doppler-frequency shift it imprinted on its host star's spectrum during their orbital motion around their combined center of gravity [14]. In this case, the relative Doppler-frequency shift from the hot Jupiter-size planet corresponded to $\sim$ 200 MHz, i.e. a differential radial velocity of $\sim$ 100 m/s. Key to this measurement was the high frequency stability of the spectrograph obtained through careful instrument design and frequent calibration with a thorium-argon lamp [156]. The exciting prospect of extending this technique to detecting Earth-like planets requires significantly higher level of stability and precision corresponding to 10 cm/s over a one-year time scale. Monitoring Doppler-shifts with even higher stability of only few cm/s over several decades would enable to observe the cosmic expansion in 'real-time', constraining current ambiguities in cosmological models. In addition, accurate and precise measurements of absorption features in quasi-stellar objects would enable the measurement of physical constants (e.g. fine structure constant) and constraining their potential evolution over cosmological time scales [157, 158, 159, 160, 161]

In contrast to laboratory based precision spectroscopy, astronomical spectroscopy operates at low photon-fluxes and strongly broadened spectral features. The required precision can only be reached statistically, when detecting a high number of spectral features across a wide optical wavelength range. Current and

future high-resolution astronomical spectrographs can resolve spectral features of ∼10 GHz width across wavelengths spans of hundreds of nanometers within the ultra-violet to infrared wavelength ranges (ca. 350 to 2400 nm). Therefore, broadband calibration light sources providing spectral features that can be resolved by the spectrograph across broad optical bandwidths are critically needed.

The discovery potential of astronomical precision spectroscopy has sparked significant efforts towards more stable, precise and accurate calibration sources. A well-established method to generate bright calibration markers over a broad bandwidth is using a Fabry-Pérot (FP) cavity-filtered, broadband white light source (Fig. 5.1b) [162, 53, 54]. The cavity is designed to match the resolution of the spectrograph, with a free-spectral range in the tens of GHz. This technology is technically mature and robust, which is a key asset for low-downtime and low-maintenance operation at astronomical sites. However, as this method relies on the cavity's intrinsic stability it is susceptible to drifts. These drifts can be mitigated to some extent by using additional atomic cross-calibration standard such as halogen lamps [55, 163, 164, 165], however, their emission lines are sparse and do not provide the required stability. A higher stability can be achieved for one cavity resonance by referencing it to a rubidium-stabilized laser [52, 166, 167, 168, 169, 170], however, this single point stabilization does not capture wavelength-dependent drifts of the cavity resonances which emerge from changes in temperature, pressure, and aging of the cavity's coatings[171, 172].

Uniquely-suited sources for broadband precision calibration are optical frequency combs [173, 105, 48, 174, 49, 50, 175]. They provide spectra of narrow and equidistant laser lines with frequencies $f_n = f_0 + n f_{\text{rep}}$, where f_0 is the (carrier-envelope) offset frequency and f_{rep} the repetition rate of the laser. Both f_0 and f_{rep} can be linked to the definition of the SI second and, in that sense, provide absolute accuracy and stability. If the comb lines can be resolved by the spectrograph, which requires f_{rep} to be in the tens of GHz, such *astrocombs* can in principle provide the required level of metrological precision and are therefore considered the currently best option for high-performance calibration (Fig. 5.1c). Astrocombs can be derived from filtered mode-locked lasers [45, 176, 177, 178, 179, 46, 47, 180, 181], electro-optic modulators [182, 183, 184, 185, 186, 187] and microresonators [188, 189, 187] and have been demonstrated in infrared, visible and ultra-violet wavelength ranges. However, a minimal energy per laser pulse is needed for broadband spectral generation via nonlinear optical effects. This, in combination with the requirement of high-repetition rate (>10 GHz), implies high optical average power, which makes astrocomb generation and routine operation challenging.

Here, we propose a novel SI-traceable frequency-comb based method for the calibration of astronomical spectrographs that does not require the high-repetition rate of astrocombs. Instead, it combines the robustness of Fabry-Pérot calibration light with the mature technology of low-repetition rate lasers. In our approach, the modes of the Fabry-Pérot cavity are tracked by performing broadband dual-frequency comb spectroscopy (DCS) [10, 11, 12, 13, 75], providing precise frequency information on the cavity resonances and its trans-
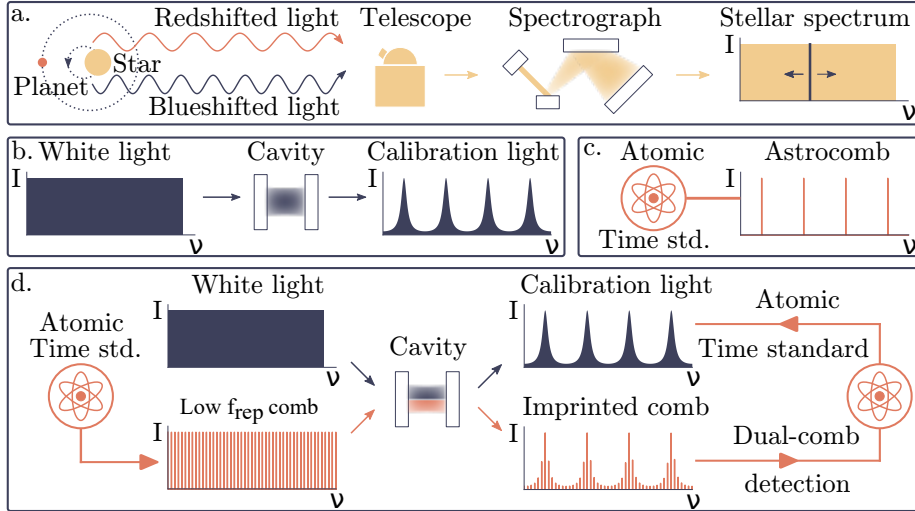
Figure 5.1: Concept of the dual-frequency comb assisted astronomical spectrograph calibrator. **a.** The radial velocity method for exoplanet detection relies on detecting minute Doppler shifts in a stellar spectrum caused by the rotation of the host star due to an exoplanet. To detect these shifts, highly accurate and precise calibration of the astronomical spectrograph is required. **b.** Calibration markers for an astronomical can be reliably and simply generated by filtering a white light supercontinuum with an appropriate Fabry-Pérot cavity, although the frequency of the resulting markers is not absolutely known. **c.** Laser frequency combs (astrocombs) offer bright calibration markers linked to an atomic time standard, although are challenging to implement and operate due to the required high-repetition rates in the tens of GHz. **d.** The novel method of calibration. The Fabry-Pérot cavity is fully characterized by measuring its optical features with a dual-comb spectrometer based on low-repetition rate lasers linked to an atomic time standard. The frequency of the calibration markers obtained by cavity filtering of a white light supercontinuum are then known with comb precision.

mission, which can be used for calibration (Fig. 5.1d). DCS relies on the multi-heterodyning of two optical frequency combs with slightly different repetition rates and enables the coherent mapping of the optical transmission spectrum of the Fabry-Pérot cavity into the radio-frequency domain. While conceptually related to Fourier-transform spectroscopy, DCS does not require moving mechanical parts, a major asset for low-maintenance operation. Moreover, it provides fast spectral acquisition, high-resolution and high signal-to-noise ratio and, importantly, if two SI-referenced frequency combs are used, can provide absolute accuracy and precision. Owing to its unique characteristics, DCS has been used in the past as an enabling technology in a diverse range of applications such as photo-acoustic spectroscopy [121, 112], ranging [40], cavity ring-down spectroscopy [36], hyperspectral imaging and holography [116, 141, 38], ptychoscopy [37], photothermal spectroscopy [39] and molecular sensing in the mid infrared and ultraviolet wavelength ranges [25, 27].

In our case, DCS permits the full characterization of the Fabry-Pérot cavity in short time, providing access not only to a potential global frequency shift of the cavity, but also to its line-by-line chromatic dispersion. As the generation of the calibration markers is now separate from obtaining accurate and precise frequency information, this technique does not require high-repetition rate lasers, effectively bypassing the associated challenge of generating broadband high-repetition rate astrocomb spectra. Our work therefore offers a complementary approach to spectrograph calibration for astronomical precision spectroscopy with significantly reduced complexity.

5.2   Results

The experimental setup employed in this study is illustrated in Fig 5.2. It utilizes a dual-comb spectrometer built around two commercially available low-noise solid-state mode-locked lasers operating at 1 GHz at 1560 nm center wavelength, each offering tunable repetition rate and offset frequency, as detailed in [190]. The repetition rates and offset frequencies of these combs are referenced to a 10 MHz GPS-disciplined Rubidium clock and effectively linked to the SI standard. The average optical power of the combs is amplified to approximately 900 mW and pulse duration of approximately 100 fs. Subsequently, these pulses are broadened by passing through 1.5 meters of normal-dispersion highly non-linear fiber, leading to broadband spectra that span over 300 nm (30 THz), as shown in the insets of Fig 5.2.   The optical cavity employed for this demonstration, shown in Fig. 5.2, is an astronomical Fabry-Pérot cavity with a near-infrared coating and a free-spectral range of approximately 12 GHz [165]. When illuminated with a white-light supercontinuum source, this cavity generates calibration markers over a broad spectral range, as illustrated in Fig. 5.3a, which are well-suited for the calibration of high-resolution infrared spectrographs. To precisely measure its modes, the cavity is sampled with one comb in a free-space configuration, as displayed in orange Fig. 5.2. The optical information from the cavity can be retrieved by multi-heterodyning the probing comb with
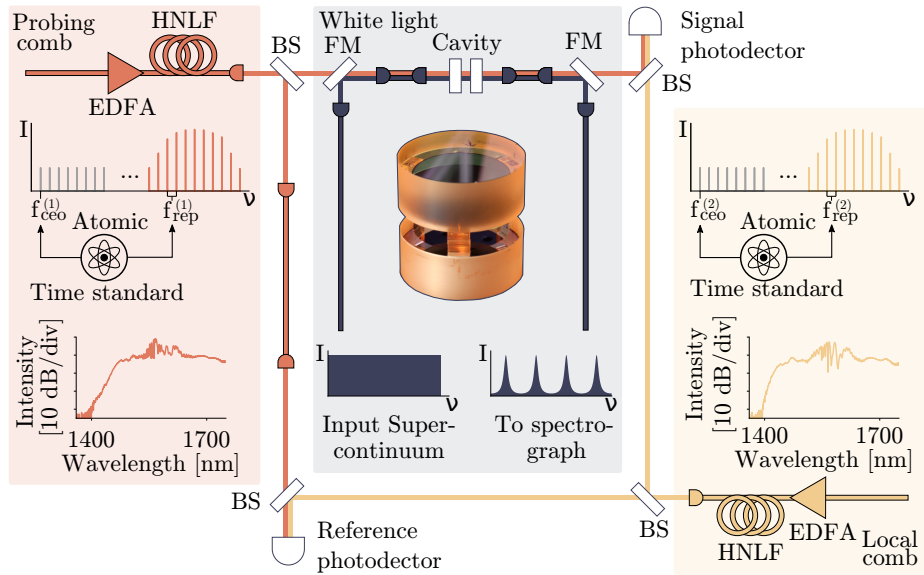
Figure 5.2: Experimental setup. An interferometric configuration permits the recording of a trace containing the cavity's optical features, as well as, a reference trace used for normalization. The path of the comb probing the cavity is depicted in orange, while the local comb is depicted in yellow. Both combs are referenced to a GPS-disciplined Rubidium clock, and their spectra are shown in the insets, covering more than 30 THz. Calibration markers suitable for an astronomical spectrograph are generated by sending a white-light supercontinuum through the Fabry-Pérot, as depicted in blue. A picture of the astronomical cavity provided by the Geneva observatory used in this demonstration is shown in the middle. EDFA: Erbium-doped fiber amplifier, HNLF: highly nonlinear fiber, S: beamsplitter, FM: flip mirror.
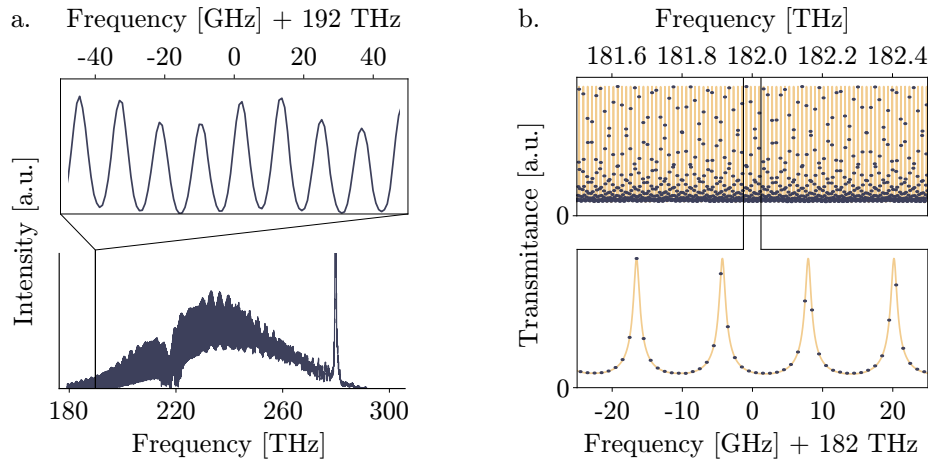
Figure 5.3: Experimental results. **a.** White light supercontinuum filtered by the cavity, providing appropriate calibration markers for an astronomical spectrograph. Recorded with an optical spectrum analyzer with a 0.1 nm resolution bandwidth. **b.** Selected spectral portions of the dual-comb measurement of the optical cavity modes. The experimental data points (blue) are fitted with the expected lineshape of the cavity (yellow).

a second comb (shown in yellow in Fig 5.2) through photo-detection, via dual-frequency comb spectroscopy. The repetition rate difference between the two combs of around 800 Hz leads to a down-conversion of the optical signal from the $\sim 170 - 210$ Thz range to radio frequencies between 45 and 75 MHz. With this configuration, spectra as wide as one octave could be readily measured. The resulting interferograms are recorded for a duration of approximately 2 seconds using a fast digitizer. This integration time is currently limited by the digitizer memory of 4 GB, although real-time data reduction for longer integration times could be implemented if necessary [97].

To prevent distortion of the measured cavity modes due to imperfect flatness of the comb spectra or their variation in time, a reference interferometric path without the cavity is recorded simultaneously. This reference permits concurrent normalization of the dual-comb signal and removes any contribution stemming from variations in the comb spectra, as well as compensates for any spectral power irregularities. Additionally, a measurement is performed without the cavity in the signal beam path to obtain the spectrally-dependent transmission of the interferometer. This measurement permits the removal of spectral systematics introduced by the interferometric setup, such as parasitic etalons or frequency-dependent splitting ratios from beam splitters. A Fourier transformation and normalization of the interferograms yields a down-converted spectrum of the cavity which can be mapped back to the optical domain, providing a 30 THz broadband, absolute measurement of the cavity modes with a 1 GHz spectral sampling interval, as shown for a 1 THz window in Fig. 5.3b in blue.
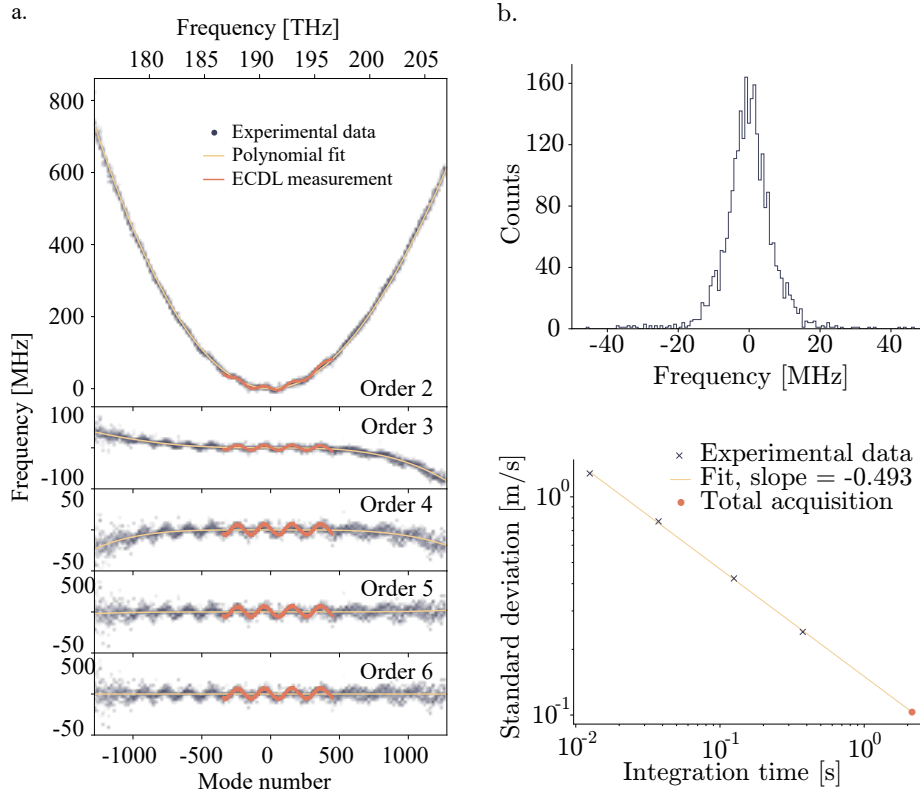
Figure 5.4: Experimental results. **a.** Integrated dispersion of the cavity as measured by the dual-comb spectrometer in blue, highlighting clear quadratic dispersion of the cavity modes. Subsequent panels show the residuals after removing the dominant polynomial orders. A polynomial fit of the integrated dispersion for each order is depicted in yellow. A measurement of the cavity obtained with a tunable continuous wave laser is given in orange for comparison. The oscillatory behavior of the experimental data is due to imperfect spatial coupling in and out of the cavity and commented in the main text. **b.** Histogram of the residuals after removing an order 5 polynomial from the integrated dispersion. **c.** The standard deviation associated to a dual-comb measurement of the cavity features, reaching 24 cm/s for a ~ 0.37 s measurement and projected to reach 10 cm/s for a full 2 s measurement.

Calibration of an astronomical spectrograph can then be achieved based on the measured cavity transmission, which defined the spectral calibration markers.

To explore the proposed technique further, the chromatic dispersion of the cavity is retrieved. To do so, the central frequency of each of its optical modes is determined through fitting with an expected, theoretical mode lineshape. As the finesse of the cavity is low, the transmission $|T(\omega)|$ (with ω the angular frequency) of the cavity can not be approximated by a Lorentzian. Rather, assuming a perfectly planar cavity with mirror reflectivity R, a straightforward computation gives

$$|T(\omega)| = \frac{1 - R}{\sqrt{1 + R^2 - 2R\cos\left(\omega/\nu_{\text{FSR}}\left(\omega\right)\right)}}, \qquad (5.1)$$

where ν_{FSR} is the free-spectral range of the cavity. From the fitting results shown in Fig. 5.3b in yellow, the integrated dispersion of the cavity, which corresponds to the frequency offset of its modes from an equidistant frequency grid, is calculated and displayed in Fig. 5.4a in blue. Since the cavity's dispersion is expected to vary slowly with wavelength, it is estimated over the measurement's bandwidth using a polynomial fit in yellow for analysis, although it is not required for an actual calibration. Higher-order terms of this polynomial are subtracted from the experimental data until the residuals show no frequency-dependent slope, as shown in Fig. 5.4a, and are symmetrically distributed around zero, as depicted in Fig 5.4b. These results demonstrate that a 5th-order polynomial effectively reproduces the cavity's broadband dispersion over this bandwidth, though alternative filtering or fitting techniques can be employed for larger optical bandwidths. A measurement of the cavity's dispersion using a frequency comb-calibrated tunable continuous wave laser [191], shown in orange in Fig. 5.4a, is in excellent general agreement with the dual-comb measurement over the tuning range of the laser.

From the lower panels of Fig. 5.4a, it is apparent that the integrated dispersion measured by the dual-comb spectrometer displays noticeable oscillatory behavior. We attribute the oscillatory pattern, at least in parts, to the broadband dielectric mirror coatings. In addition we observed that the exact pattern is sensitive to the mode-matching between input coupler, cavity and output coupler. Imperfect mode-matching between the incoming beam and the cavity mode can result in minute frequency-dependent asymmetries in the cavity's lineshape, which can lead to a perceived shift of the lines centroid. These effects are precisely measured by the dual-comb technique, which shares the beam path with the supercontinuum light source from which the calibration markers are derived.

To assess the precision of the method, a 2 second duration measurement of the cavity features is divided into N segments of equal length. For each segment i, the central frequency f_μ^i of each optical mode μ of the cavity is obtained through lineshape fitting, and the standard deviation of the retrieved

frequencies is calculated as

$$\sigma_\mu = \sqrt{\frac{1}{N} \sum_{i=1}^{N} \left(f_\mu^i - \bar{f}_\mu\right)^2}, \tag{5.2}$$

where

$$\bar{f}_\mu = \frac{1}{N} \sum_{i=1}^{N} f_\mu^i. \tag{5.3}$$

The corresponding aggregated frequency deviation over all cavity modes is then given by

$$\sigma = \frac{1}{\sqrt{\mu_{tot}}} \sum_{\mu=1}^{\mu_{tot}} \frac{\sigma_\mu}{\mu_{tot}}, \tag{5.4}$$

where μ_{tot} is the number of measured cavity modes. By repeating this procedure for segments of 10, 30, 100 and 300 interferograms, a clear and expected scaling of the standard deviation with the inverse square root of time is observed, as shown in Fig. 5.4c. The standard deviation of the cavity's resonant frequencies is experimentally measured to be ~ 7 MHz per resonance on average for the series of 300 interferograms, corresponding to a statistical deviation of 24 cm/s over the ~ 2300 measured resonances. Assuming the scaling with time holds for more than 2 seconds, a full 2 second measurement reaches an estimated deviation of 10 cm/s. Although our experiment is a proof-of-concept demonstration, this level of precision is comparable to state-of-the-art calibration of astronomical spectrographs.

Our technique has additional benefits in its short measurement times of 2 seconds, which may alleviates the need for long-term stability (e.g. across a full night) in the Fabry-Pérot cavities as they can be calibrated on the fly. In addition, these short acquisition times could permit stepping of the Fabry-Pérot cavity resonances via e.g. a piezo actuator to sequentially characterize each pixel of the spectrographs detector.

5.3 Conclusion

A novel technique for calibration of astronomical spectrometers is proposed. This technique combines the robustness of Fabry-Pérot-based calibration with the precision and accuracy of laser frequency combs, without however requiring high-repetition rate. While our proof-of-concept demonstration is limited to a spectral span of 30 THz, we estimate that it could in principle provide a calibration of better than 25 cm/s level, comparable to what would be needed for the detection of Earth-like exoplanets. Future extension to broader spectral coverage can likely increase the precision further. The ability to rapidly characterize the Fabry-Pérot cavity may relax the need for its long-term stability and permit tuning its resonance frequencies so that calibration light can be sent to any part of the detector for further improved and complete calibration. The robustness

of the system, including its off-the-shelf lasers, permits low-maintenance operation and the reduced cost in comparison to high-repetition rate astrocombs may make comb-based precision calibrators accessible to a larger number of telescopes and instruments.

Chapter 6

Simulating supercontinua from mixed and cascaded nonlinearities

Thibault Voumard[1], **Markus Ludwig**[1], **Thibault Wildi**[1], **Furkan Ayhan**[2], **Victor Brasch**[3], **Luis Guillermo Villanueva**[2], **Tobias Herr**[1,4]

[1] *Deutsches Elektronen-Synchrotron DESY, Notkestr. 85, 22607 Hamburg, Germany*
[2] *École Polytechnique Fédérale de Lausanne (EPFL), CH-1015 Lausanne, Switzerland*
[3] *Centre Suisse d'Electronique et Microtechnique SA (CSEM), CH-2002 Neuchâtel, Switzerland. Currently at Q.ant GmbH, Handwerkstraße 29, 70565 Stuttgart, Germany*
[4] *Physics Department, Universität Hamburg, Luruper Chaussee 149, 22761 Hamburg, Germany*

Context

To push the optical coverage of 1 GHz dual-comb spectrometers further, the optimization of their spectral extension processes is necessary due to their relatively low peak powers. For this reason, a software capable of simulating the propagation of pulses in waveguide structures exhibiting both quadratic and cubic nonlinearities is developed. In particular, this software permits the investigation of photonic integrated waveguides, which have already demonstrated impressive spectral extensions of high repetition rate sources and are prime candidates for achieving extremely broadband coverage. With the design opportunities provided by the software, these platforms could enable the extension of the demonstrated techniques to the mid- and far-infrared for molecular spectroscopy and to the visible for the astronomical spectrograph calibration. In a broader perspective, this software is generally useful to investigate and optimize any co-linear supercontinuum generation or frequency conversion process. Additional information about the software, its installation and the underlying theory is given in Appendix C.

Author contribution

The author derived the theory, conceived the new solver and anti-aliasing scheme, implemented the simulation software and conducted the simulation and data analysis. The author and T. Herr jointly wrote the manuscript.

Simulating supercontinua from mixed and cascaded nonlinearities

Nonlinear optical frequency conversion is of fundamental importance in photonics and underpins countless of its applications: Sum- and difference-frequency generation in media with quadratic nonlinearity permit reaching otherwise inaccessible wavelength regimes and the dramatic effect of supercontinuum generation through cubic nonlinearities has resulted in the synthesis of broadband multi-octave spanning spectra, much beyond what can be directly achieved with laser gain media. Chip-integrated waveguides permit to leverage both, quadratic and cubic effects at the same time, creating unprecedented opportunities for multi-octave spanning spectra, across the entire transparency window of a nonlinear material. Designing such waveguides often relies on numeric modeling of the underlying nonlinear processes, which, however, becomes exceedingly challenging when multiple and cascading nonlinear processes are involved. Here, to address this challenge, we report on a novel numeric simulation tool for mixed and cascaded nonlinearities that uses anti-aliasing strategies to avoid spurious light resulting from a finite simulation bandwidth. A dedicated 5th-order interaction picture Runge-Kutta solver with adaptive step-size permits efficient numeric simulation, as required for design parameter studies. Importantly, the simulation results are shown to quantitatively agree with experimental data and the simulation tool is made available as an open-source Python package (PyChi).

6.1   Introduction

Broadband optical spectra find a wide range of applications in optical sensing, spectroscopy, tomography, ultrashort pulse generation and optical precision metrology from terahertz to ultraviolet frequencies [192]. Often, laser sources with the desired properties cannot operate directly in the spectral region of interest. Instead, spectral content at the desired wavelength may be generated from a pump laser source through nonlinear optical frequency conversion. Sum- (SFG) and difference-frequency generation (DFG) in non-centrosymmetric optical crystals have enabled, for instance, optical parametric amplifiers and oscillators in the mid-infrared and terahertz regimes, as well as high-harmonic and ultra-violet pulse generation. Extreme spectral broadening of optical pulses, in some cases only limited by material transparency, has been achieved through the effect of supercontinuum generation based on the cubic nonlinearities in step-index, photonic crystal and specialty fibers [193].

More recently, chip-based integrated micro- and nano-photonic waveguides have emerged as a powerful addition to established nonlinear media [194, 195, 196, 197, 198]. Such waveguides can tightly confine light to sub-square micrometer cross-section and can be made from highly nonlinear materials. Moreover, lithographically defined on the nanoscale, integrated waveguides offer new opportunities for dispersion engineering via the modification of their dimensions or through subwavelength patterning along the propagation direction (e.g. pe-

riodic poling or photonic bandgap engineering). Through advances in thin film technology, a wide variety of materials is available, including materials with transparency in the terahertz, mid-infrared, visible or ultra-violet wavelength domains. Waveguides with cubic nonlinearity have given rise to ultrabroadband supercontinua [199, 200, 201, 202, 203], with simultaneous third-harmonic or triple-sum frequency generation (TFG) [204]. Waveguides with quadratic and cubic nonlinearities have given rise to high-harmonic generation and simultaneous spectral broadening [205, 206, 207]. Quadratic nonlinearities have also been observed in waveguides made from centrosymmetric materials, where they can originate from surface-induced symmetry breaking or photo-induced periodic redistribution of charges [208, 209]. Designing integrated waveguide usually relies on numeric simulation of the underlying nonlinear optical processes. However, efficiently simulating all possible cascaded nonlinear optical processes in integrated waveguides is non-trivial as it requires a broadband, densely sampled, uninterrupted frequency interval. Additionally, cascaded nonlinearities can lead to the formation of numeric aliases (i.e. incorrect simulation results) due to the cyclic nature of the discrete Fourier transform, thus demanding the implementation of anti-aliasing strategies for efficient and accurate simulation.

Nonlinear propagation phenomena can be described via the generalized nonlinear Schrödinger equation (GNLSE), which remains valid even for extremely short pulses in the single cycle regime [210, 211, 192]. Besides self-phase modulation (SPM), additional effects such as Raman scattering, self-steepening, frequency dependence of the nonlinear parameters and refractive index can readily be included. The GNLSE has also been adapted in recent years to incorporate additional cubic and quadratic nonlinear effects such as SFG or TFG [212, 213, 214, 215, 216, 217, 206, 218, 219, 220, 221].

Here, we present a numeric tool for the simulation of light propagation in nonlinear media and waveguides. It implements an extended GNLSE accounting for cubic and quadratic nonlinear interactions, as well as, Raman scattering and self-steepening. To avoid computational artifacts in the multi-octave nonlinear simulation, anti-aliasing strategies are implemented. Modeling of frequency- or spatially-dependent (along the propagation direction) parameters is readily possible, for instance frequency conversion in aperiodically poled waveguides, or materials with spatially-varying dispersion. A dedicated, 5th-order Runge-Kutta solver with adaptive step-size has been implemented for short computation times and high rate of convergence even on a generic desktop computers. To validate the numeric tool, experiment of broadband frequency conversion in photonic integrated waveguides with quadratic and cubic nonlinearities are performed and shown to agree well with the numeric results. The numeric simulation tool is made available as an open-source *Python* package (*PyChi*).

6.2 Propagation model

Following the approach in previous work [218], a temporal field envelope is defined as a function of propagation coordinate z and time t

$$A(z,t) = \left(E(z,t) + i\mathcal{H}[E(z,t)]\right)e^{-i\omega_0 t + i\beta(\omega)z}, \tag{6.1}$$

where $E(z,t)$ is the electric field, $\mathcal{H}$ denotes the Hilbert transform, ω_0 is the center frequency of the simulation and $\beta(\omega)$ is the frequency-dependent wave vector in the nonlinear medium. Note that Fourier transforms of quantities are denoted with the corresponding lowercase symbols, e.g. $\mathcal{F}[A(z,t)](\omega) = a(z,\omega)$. The evolution of the spectral field envelope along the propagation direction z is given by

$$\partial_z a(z,\omega) + i\beta(\omega + \omega_0)a(z,\omega) = \mathcal{N}[a(z,\omega)], \tag{6.2}$$

where $\mathcal{N}[a(z,\omega)]$ is the general nonlinear operator describing wave-mixing interactions. Keeping all interactions up to cubic order yields

$$\mathcal{N}[a(z,\omega)] = -\frac{i(\omega + \omega_0)}{4n(\omega + \omega_0)c}\left(p_{NL}^{(2)}(z,\omega) + p_{NL}^{(3)}(z,\omega)\right),$$

where

$$P_{NL}^{(2)}(z,t) = \chi^{(2)}\Big[A(z,t)^2 e^{i\omega_0 t} \qquad\qquad\text{(SFG)}$$

$$+ 2|A(z,t)|^2 e^{-i\omega_0 t}\Big] \qquad\qquad\text{(DFG)}$$

and

$$P_{NL}^{(3)}(z,t) = \frac{\chi^{(3)}}{2}\Big[3A(z,t)|A(z,t)|^2 \qquad\qquad\text{(SPM)}$$

$$+ 3A^*(z,t)|A(z,t)|^2 e^{-2i\omega_0 t} \qquad\qquad\text{(CKT)}$$

$$+ A^3(z,t)e^{2i\omega_0 t}\Big] \qquad\qquad\text{(TFG)}$$

The terms responsible for sum-frequency (SFG), difference-frequency (DFG) and triple-sum frequency generation (TFG), as well as, self-phase modulation (SPM) and the conjugated Kerr term (CKT) have been identified, $n(\omega)$ is the effective refractive index (including material and geometric dispersion effects) and $\chi^{(2)}$ respectively $\chi^{(3)}$ are the quadratic respectively cubic nonlinear coefficients. This equation accounts for the frequency-dependence of the nonlinear operator (which is responsible for self-steepening) and is here slightly modified to also include Raman scattering via the introduction of a frequency-dependent susceptibility [222, 223]

$$\chi^{(3)}(\omega', \omega'', \omega''') := \chi^{(3)}g(\omega' - \omega''), \tag{6.3}$$

where ω', ω'' and ω''' are the angular frequencies of the mixing fields driving the polarization, with

$$G(t) = \alpha\delta(t) + (1 - \alpha)\frac{\tau_1^2 + \tau_2^2}{\tau_1\tau_2^2}e^{-t/\tau_2}\sin(t/\tau_1), \tag{6.4}$$
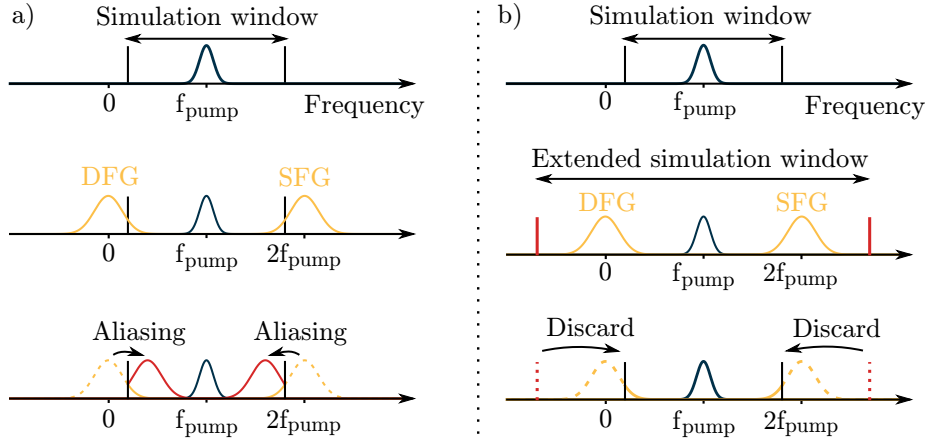
Figure 6.1: Anti-aliasing strategy. a) Schematic representation of a quadratic nonlinear interaction leading to spurious numeric aliases in the simulation window. b) Example of the anti-aliasing algorithm implemented for the same quadratic nonlinear interaction. The simulation window is temporarily elongated to prevent aliases from forming, and subsequently reduced to its original size, providing an alias-free computation of nonlinear interactions. DFG: difference-frequency generation, SFG: sum-frequency generation.

where α, τ_1 and τ_2 are material-dependent quantities (typically, $\alpha \approx 0.7$ to 0.82, $\tau_1 \approx 0.0122$ ps, $\tau_2 \approx 0.032$ ps for silica fibers [223, 222]).

6.3 Computational scheme

Through the SFG, DFG, CKT and TFG nonlinear interaction terms, light with frequency components outside of the simulation range can be generated. These frequency components will get aliased and folded back into the simulation domain due to the cyclic nature of the discrete Fourier transform. Untreated, this behavior leads to spurious light aliases in the simulation window. Simply extending the simulation window is not a viable strategy as the computational costs increase accordingly and cascaded nonlinear interactions will eventually lead to the appearance of aliases. Consequently, an anti-aliasing protection is implemented, as exemplified with a quadratic nonlinearity in Fig. 6.1. Such techniques have been largely applied in the fields of nonlinear electronics and fluid mechanics and can be equivalently used here. At each step, the field is Fourier transformed and padded with zeros in the frequency domain, effectively augmenting the span of the simulation window. If the original simulation bandwidth is $\Delta\omega$, the padding needs to extend the field by a factor $\frac{N+1}{2} + \frac{(N-1)\omega_0}{\Delta\omega}$, where N is the nonlinearity's order (note that in case of mixed nonlinearities the nonlinear terms are computed separately). The padded field is transformed back in the time domain and the nonlinear terms are computed, with resulting

frequencies all comprised within the extended simulation window [224, 225]. After Fourier transforming the time-domain nonlinear terms, only the frequency components contributing to the original simulation window are retained, providing an alias-free computation. Notably, this scheme preserves the total energy of the pulse as the discarded spectral components are not allowed to build up, thus do not draw energy from the pulse. Further details about the anti-aliasing technique such as comparison against propagation without protection, proof of energy conservation and the choice of padding sizes are given in the Supplementary Material.

In general, nonlinear interactions are computationally expensive to simulate and thus require some degree of numerical optimization in order to achieve fast execution times, particularly in models where all five nonlinear interactions are simulated. To this end, the efficient fast Fourier transform library *pyfftw* and the optimization library *numba* have been used. A powerful numeric solver that could be used here is the 4th-order Runge-Kutta RK4IP scheme [226]. It leverages the so-called interaction picture of the propagation (corresponding to a change of reference frame analogous to the quantum mechanical interaction picture) in order to reduce the number of computational operations per step. However, it is not an embedded method, i.e. it does not directly provide an error estimation for an efficient adaptive step-size control. Strategies such as step-doubling have been employed to provide error estimation. Although this significantly augments the computational cost per step, the reduction in the required number of steps results in faster overall integration times [227, 228]. A later adaptation called the ERK4IP [229] provided an embedded version of the RK4IP requiring no extra operations for error estimation and was also tested in this work. In our implementation, using this solver yielded a 3 to 4 times reduction of computation time over the step-doubling RK4IP for SPM-based propagation. When other nonlinear processes are taken into account, we found that even higher order schemes perform better by providing a higher rate of convergence. Consequently, we implemented a new 5th-order Runge-Kutta solver based on the Dormand-Prince method [230] adapted in the interaction picture, requiring fewer dispersion operations.

	1	2	3	4	5	6	7
α_{2j}	1/5						
α_{3j}	3/40	9/40					
α_{4j}	44/45	-56/15	32/9				
α_{5j}	19372/6561	-25360/2187	64448/6561	-212/729			
α_{6j}	9017/3168	-355/33	46732/5247	49/176	-5103/18656		
α_{7j}	35/384	0	500/1113	125/192	-2187/6784	11/84	
α_{8j}	5179/57600	0	7571/16695	393/640	-92097/339200	187/2100	1/40
j	1	2	3	4	5	6	7

Table 6.1: Butcher tableau for the solver implemented in this work.

With the field in the frequency domain, the algorithm is the following:

$$a_I = e^{-i\Delta z \beta} a^m \tag{6.5}$$

$$k_1 = e^{-i\Delta z \beta} \mathcal{N}\left[a^0\right] \text{ or } k_1 = e^{-i\Delta z \beta} k_7^{m-1} \tag{6.6}$$

$$k_2 = e^{-\frac{4}{5}i\Delta z \beta} \mathcal{N}\left[e^{\frac{4}{5}i\Delta z \beta}(a_I + \Delta z \alpha_{21} k_1)\right] \tag{6.7}$$

$$k_3 = e^{-\frac{7}{10}i\Delta z \beta} \mathcal{N}\left[e^{\frac{7}{10}i\Delta z \beta}(a_I + \Delta z \cdot \sum_{j=1}^{2} \alpha_{3j} k_j)\right] \tag{6.8}$$

$$k_4 = e^{-\frac{1}{5}i\Delta z \beta} \mathcal{N}\left[e^{\frac{1}{5}i\Delta z \beta}(a_I + \Delta z \cdot \sum_{j=1}^{3} \alpha_{4j} k_j)\right] \tag{6.9}$$

$$k_5 = e^{-\frac{1}{9}i\Delta z \beta} \mathcal{N}\left[e^{\frac{1}{9}i\Delta z \beta}(a_I + \Delta z \cdot \sum_{j=1}^{4} \alpha_{5j} k_j)\right] \tag{6.10}$$

$$k_6 = \mathcal{N}\left[a_I + \Delta z \cdot \sum_{j=1}^{5} \alpha_{6j} k_j\right] \tag{6.11}$$

$$a^{m+1} = a_I + \Delta z \cdot \sum_{j=1}^{6} \alpha_{7j} k_j \tag{6.12}$$

$$k_7 = \mathcal{N}\left[a^{m+1}\right] \tag{6.13}$$

$$b^{m+1} = a_I + \Delta z \cdot \sum_{j=1}^{7} \alpha_{8j} k_j \tag{6.14}$$

$$\epsilon = \frac{||a^{m+1} - b^{m+1}||}{||a^{m+1}||} \tag{6.15}$$

where Δz is the step-size, a^m is the electric field envelope at step m, k_7^{m-1} is the previously computed value of k_7 and for completeness, the α_{ij} coefficients are given in the Butcher tableau, Table 6.1.

This algorithm is of order 5 in the step-size and provides a relative error ϵ for step-size control. Additionally, it has the *first-same-as-last property*, i.e.

the evaluation of k_1 does not require a nonlinear operation after the first step. Compared to the ERK4IP, the proposed scheme requires 6 nonlinear operator evaluations against 4, but is one degree higher. It has been found that the total number of nonlinear operator evaluations to achieve comparable simulations results between the two solvers does not differ. However, the higher rate of convergence of the order 5 solver leads to improved error estimation and step-size control, which has empirically proven useful for the dynamics of mixed and cascaded nonlinearities.

6.4   Comparison with experiments

To verify the predictive power of the software, comparisons with experimental results have been performed. In a first experiment, a lithium niobate waveguide (mode area $\sim$1 µm^2, length 6 mm, Supplementary Material for more details), exhibiting both quadratic and cubic nonlinearities, has been pumped with a 100 MHz Erbium-based oscillator. The pump pulses of 80 fs duration and central wavelength 1560 nm are coupled to the waveguide via a lensed fiber. The resulting optical spectrum obtained with approximately 10 pJ on-chip pulse energy is then recorded via an optical spectrum analyzer, see Fig. 6.2. To reproduce the experimentally obtained spectrum, material parameters and effective refractive indices (simulated by a separate finite element simulation) are used as input parameters of the simulation and a sech^2 pulse intensity profile is assumed. The simulated spectrum is shown in Fig. 6.2 (computed in $\sim$ 300 s), as well as a simulated spectrum based on SPM only. Experimental and simulated results are in excellent agreement; in particular width, position and amplitude of the SFG are accurately reproduced. The finer structure apparent in the simulated SFG spectrum results from the phase mismatch between the pump and the SFG, leading to fringes not resolved by the optical spectrum analyzer. This comparison validates the two different nonlinear operators responsible for quadratic interactions, namely SFG and DFG as well as SPM through the cubic nonlinearity.

Similarly, a silicon nitride waveguide exhibiting a purely cubic intrinsic material nonlinearity has been tested (mode area $\sim$1 µm^2, length 5 mm, Supplementary Material for more details). The experimentally observed spectrum obtained with approximately 100 pJ on-chip pulse energy reveals strong, SPM-dominated spectral broadening and TFG, see Fig. 6.3. Again, material parameters and effective refractive indices of the waveguide are used as input parameters to the numeric simulation. The simulated spectrum (computed in $\sim$ 1100 s), along with an SPM-only simulated spectrum for comparison, is shown in Fig. 6.3. Both simulated spectra reproduce the SPM-based broadening, but only the complete model captures the TFG part of the spectrum. The overall position and envelope of the TFG are well reproduced, while deviations are visible in the finer structure of the TFG spectrum. We attribute those deviations to increasing uncertainty in the material data towards shorter wavelength (impacting the waveguide disperison), as well as, physical effects not included in the simulation

Figure 6.2: Experimental spectrum obtained from a lithium niobate waveguide pumped at 1560 nm with a 100 MHz oscillator (blue) and measured with an optical spectrum analyzer (0.4 nm resolution bandwidth), along with simulated spectra. A model accounting only for self-phase modulation (yellow, vertical offset of -3 dB) is shown for comparison with a model containing quadratic and cubic nonlinearities (red).
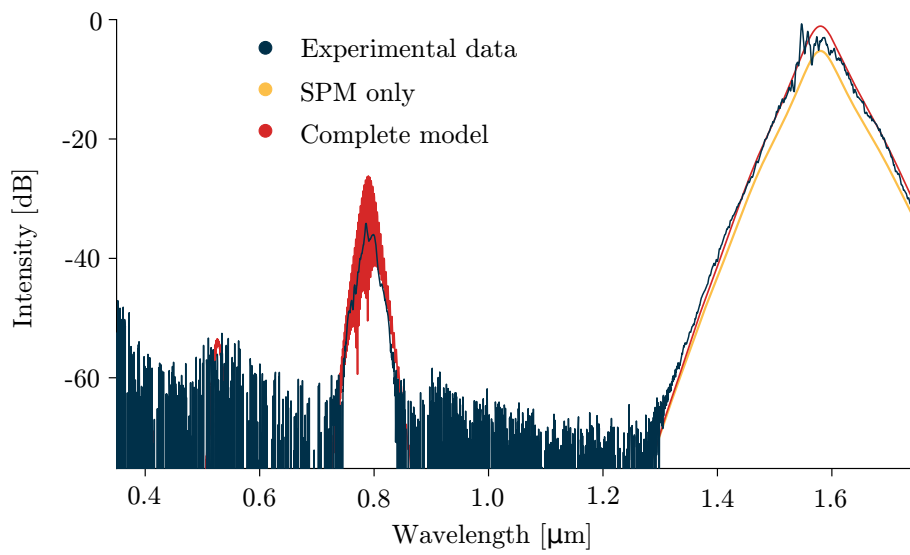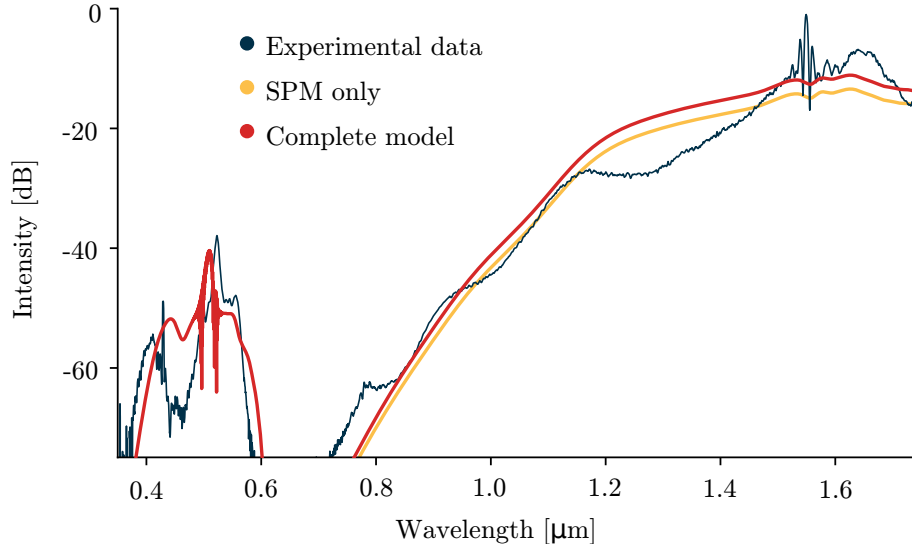
Figure 6.3: Experimental spectrum obtained from a silicon nitride waveguide pumped at 1560 nm with a 100 MHz oscillator (blue) and measured with an optical spectrum analyzer (0.4 nm resolution bandwidth), along simulated spectra. A model accounting only for self-phase modulation (yellow, vertical offset of -3 dB) is shown for comparison with a model containing quadratic and cubic nonlinearities (red).

such as surface roughness induced scattering and interaction between higher order transverse waveguide modes (e.g. sharp peak experimentally observed at around 450 nm). These results validate the remaining nonlinear operators in the propagation model, namely SPM, TFG and the CKT. We note that the solver has also been validated against previous numeric results[192] of SPM-only based supercontinuum generation as detailed in the Supplementary Material.

Finally, to illustrate the rich nonlinear physics captured by the new numeric tool, Fig. 6.4 shows the simulation of a 100 fs, 1.5 nJ pulse propagating through a hypothetical waveguide with a silicon nitride waveguide-like dispersion exhibiting commensurate cubic and quadratic nonlinearities and generating a broadband spectrum (computed in ~ 35 s). Along with strong SFG and TFG, higher-frequency cascaded nonlinearities resulting from the interplay of SFG and TFG can be observed. The different phase mismatches for each processes and frequencies lead to characteristic intensity oscillations in the propagation direction. The spatial periods of these oscillations can guide the design of quasi-phase matching polings.

The code and data used to produce the figures in this manuscript are provided along with the simulation code [231].
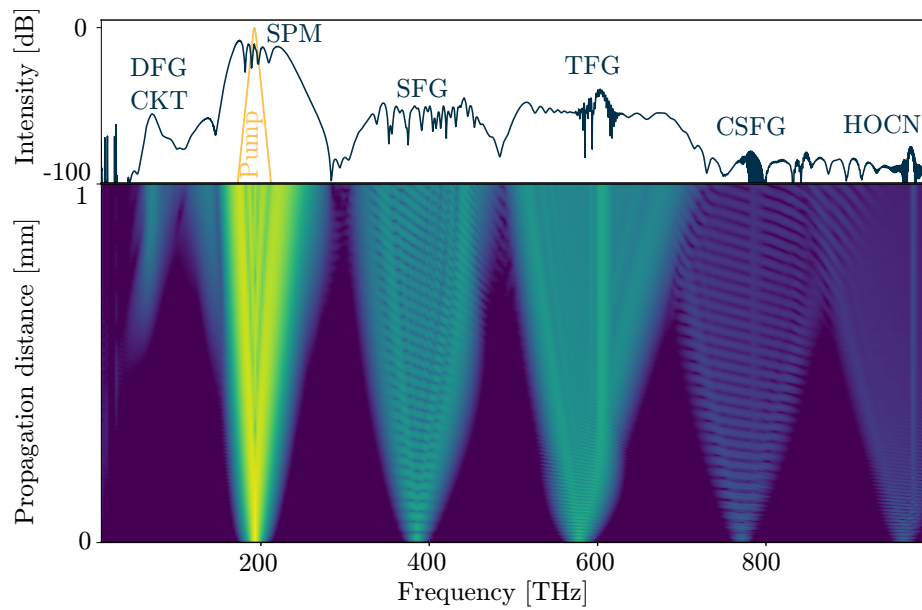
Figure 6.4: Example of simulation results obtained in a hypothetical waveguide exhibiting strong quadratic and cubic nonlinearities. Intricate interplay between the different nonlinear terms can be observed. Prominent features in the final spectrum have been noted - DFG: difference-frequency generation, CKT: conjugated Kerr term, SPM: self-phase modulation, SFG: sum-frequency generation, TFG: triple sum-frequency generation, CSFG: cascaded SFG, HOCN: higher-order cascaded nonlinearities.

6.5   Conclusion

Advances in integrated photonics have opened up new possibilities in broadband light generation. Numeric simulation of the underlying nonlinear optical processes is essential to the development of future nonlinear photonic devices and applications. Here, by implementing a new solver and an anti-aliasing scheme, we have developed a numeric tool for efficient simulation of ultra-broadband spectra including effects of quadratic and cubic nonlinearities, as well as, cascaded effects. The simulations agree with experimental data on a quantitative level and thus represent a powerful tool for the design and modeling of nonlinear optical devices and experiments. The newly developed numeric tool is made available as an open-source *python* package [231]. The presented analytical models can readily be generalized to any desired nonlinear degree (e.g. quartic, quintic, etc.) and the numeric implementation can be easily adapted in a corresponding manner. Besides the field of integrated optics, the numeric tool may also be useful for simulating broadband spectra and dynamics in specialty optical fibers, nonlinear crystals and parametric amplifiers.

6.6   Supplementary information

Below is a supplemental document published alongside the article for additional information.

6.6.1   Anti-aliasing technique

The anti-aliasing protection is key in the simulation of quadratic and cubic nonlinearities. Without it, cascaded nonlinearities can generate light outside the simulation window, which through the cyclic nature of the discrete Fast Fourier Transform (FFT) will get folded back into the simulation window. This spurious light can then couple with physical light and quickly contaminates the whole simulation, invalidating the numerical results. This effect is rarely relevant in simulations involving only self-phase modulation (spectrally local dynamics) where a sufficiently large simulation window acts as a proper anti-aliasing protection. However, when considering other nonlinearities, e.g. quadratic nonlinearity or harmonic generation, and their cascading, a sufficiently large simulation window is not possible and does not provide a numerically sound solution, as the associated computation time would become prohibitively long. As described in the main text, the approach implemented in the numeric tool is to temporarily zero-pad the propagated field, extending the simulation window to accommodate for light that could be generated outside of its initial size. Then, however, only contributions within the initial simulation window are kept. In this section we provide more details concerning the anti-aliasing technique.

Propagation with and without anti-aliasing

The necessity of the anti-aliasing technique is illustrated by Fig. 6.5 for a quadratic nonlinear interaction. A short pulse with a center frequency of 350 THz is propagated in a hypothetical waveguide with a (purely) quadratic nonlinearity. The group velocity disperison is chosen to be zero (perfect phase-matching), to better illustrate the differences between propagation with and without anti-aliasing. The left panel of Fig. 6.5 shows the propagation of the pulse with the anti-aliasing technique and displays the expected behavior: the pulse is efficiently converted to its second harmonic. One can also observe typical oscillations coming from the back-conversion of the second harmonic into the fundamental, as well as, spectral broadening due to cascaded frequency conversion acting as an effective self-phase modulation.

The right panel of Fig. 6.5, shows the same propagation without any form of anti-aliasing. Strong spurious light is immediately generated via folding of the higher order harmonics and participates in the nonlinear interaction invalidating the propagation results. These results demonstrate the necessity of an anti-aliasing technique for the simulation of mixed and/or cascaded nonlinearities.

Anti-aliasing padding size

Supposing an initial simulation bandwidth $\Delta\omega$ and a center angular frequency ω_0, the lowest, respectively highest frequency components that can be generated through a quadratic nonlinearity are $-\Delta\omega$, respectively $2\omega_0 + \Delta\omega$. A non-optimal, but reasonable choice would then be to multiply the original bandwidth by $2 + 2\omega_0/\Delta\omega$, which would ensure that all potentially generated frequency components are well resolved before being discarded. However, as the FFT *folds back* components outside of the frequency window around the window borders, a smaller window can be used. By choosing the extended simulation window edges to sit exactly at the midpoint between the initial simulation window and the generated frequency extremes, these extremes will get back-folded just short of the initial simulation window [224]. This allows one to extend the simulation window by a reduced factor $3/2 + \omega_0/\Delta\omega$. Using a similar reasoning, the argument can be extended to any nonlinearity of order N, demonstrating that a window extension factor $\frac{N+1}{2} + \frac{(N-1)\omega_0}{\Delta\omega}$ will always suffice. This generalizes the considerations of Ref.[225] to a central frequency different from zero and has been implemented here. Notably, different padding lengths are used for the different nonlinear interactions to minimize the computational time. In case of mixed nonlinearities each nonlinear contribution (i.e. quadratic and cubic) to a propagation step are computed separately with their respective value of N and corresponding padding.

Interestingly, one could further optimize the anti-aliasing algorithm to minimize the extension of the simulation window. When simulating quadratic nonlinear interactions, only initial frequency components between $\omega_0 - \Delta\omega/2$ and $\Delta\omega$ will result in a sum-frequency within the span of the initial simulation window. One can then decide to filter out all other frequency components when

79

calculating the sum-frequency term, which correspondingly reduces the extent of possible output frequencies that can be generated, without changing the final result. Accordingly, the required padding factor also decreases, and can be shown to reach $\frac{3}{2}$. By the same arguments, a nonlinear interaction of order N will require a padding factor of $\frac{N+1}{2}$, similarly as in Ref.[225]. However, the implementation of such a technique implies using additional Fourier transforms on the filtered fields and has here provided only marginally better computational times when compared with the simple method proposed above. Moerover, numeric computation of the Fourier transforms performs better when the number of points is a power of two, which reduces the potential gain of this technique. Its implementation is also more complex and prevents straightforward inclusion of nonlinearites of higher order (quartic, quintic, ...), which here led to the choice of using the simpler anti-aliasing method.

Energy conservation of the anti-aliasing technique

The proposed anti-aliasing scheme preserves the total energy during propagation, which intuitively can be understood as follows: Suppose that we have a continuous wave light, whose complex amplitude is denoted a_0 and whose second harmonic of amplitude a_1 stands in the frequency region which is discarded by the algorithm. The action of sum-frequency and difference-frequency generation during propagation couple a_0 with a_1 via [232]

$$\partial_z a_0 \propto a_1 a_0^* \tag{6.16}$$

$$\partial_z a_1 \propto a_0 a_0. \tag{6.17}$$

Numerically, one can approximate these equations at step $n+1$ with

$$a_0^{n+1} - a_0^n \propto a_1^n a_0^{n*} \tag{6.18}$$

$$a_1^{n+1} - a_1^n \propto a_0^n a_0^n. \tag{6.19}$$

By definition, the anti-aliasing algorithm will force a_1 to zero at each step by discarding it, so $a_1^n = 0$. Consequently, $a_0^{n+1} = a_0^n$, so that the complex amplitude of a_0 is conserved, implying that its energy is also conserved. Generalizing this observation to a continuum rather than a continuous wave laser and other nonlinearities then implies that the energy is unaffected by the anti-aliasing technique.

A rigorous proof for the scheme implemented in the numeric tool is as follows. By definition, energy conservation is achieved if

$$\int_{-\infty}^{\infty} d\omega \; n(\omega + \omega_0)|a(z,\omega)|^2 = cst. \tag{6.20}$$

From the finite width of the simulation window, the analytical envelope $a(z,\omega)$ is restricted to a finite support of width $\Delta\omega$. During the anti-aliasing algorithm, at each nonlinear step, the field is first zero-padded, which does not change the total energy. The padding is large enough to accommodate for any frequency

that could be generated from the initial simulation window. Next, the nonlinear terms are evaluated, and only terms that fall within the original simulation window are kept. This corresponds to restricting the support of the nonlinear terms to that of the analytical envelope. As the derivative of the analytical envelope is dictated by these nonlinear terms, having the analytical envelope confined to its support equivalently fulfills this condition. To demonstrate that the technique conserves energy, one must thus show that

$$\int_{-\Delta\omega/2}^{\Delta\omega/2} d\omega \ n(\omega + \omega_0)|a(z,\omega)|^2 = cst, \tag{6.21}$$

which is equivalent to demonstrating

$$\partial_z \int_{-\Delta\omega/2}^{\Delta\omega/2} d\omega \ n(\omega + \omega_0)|a(z,\omega)|^2 = 0. \tag{6.22}$$

Carrying out the derivative, it is then sufficient to prove that

$$\Sigma := \int_{-\Delta\omega/2}^{\Delta\omega/2} d\omega \ n(\omega + \omega_0)\big(a(z,\omega)\partial_z a^*(z,\omega)$$
$$+ a^*(z,\omega)\partial_z a(z,\omega)\big) = 0. \tag{6.23}$$

From the propagation model,

$$\partial_z a(z,\omega) + i\beta(\omega + \omega_0)a(z,\omega) = \mathcal{N}[a(z,\omega)] \tag{6.24}$$

which implies

$$a(z,\omega)\partial_z a^*(z,\omega) + a^*(z,\omega)\partial_z a(z,\omega)$$
$$= a(z,\omega)\mathcal{N}^*[a(z,\omega)] + a^*(z,\omega)\mathcal{N}[a(z,\omega)]. \tag{6.25}$$

From now on, the z dependency of $a(z,\omega)$ will be omitted. We will proceed to demonstrate energy conservation for quadratic nonlinear processes only, as the proof for other nonlinearity orders can be derived in the same way. One has

$$n(\omega + \omega_0)\mathcal{N}[a(\omega)] = \frac{-i(\omega + \omega_0)\chi^{(2)}}{8\pi c}$$
$$\cdot \int_{-\Delta\omega/2}^{\Delta\omega/2} d\omega' \ \big[a(\omega')a(\omega - \omega_0 - \omega')$$
$$+ 2a(\omega')a^*(\omega' - \omega_0 - \omega)\big], \tag{6.26}$$

where one can recognize the terms responsible for sum-frequency and difference-

frequency generation. Consequently,

$$\Sigma = \int_{-\Delta\omega/2}^{\Delta\omega/2} d\omega \int_{-\Delta\omega/2}^{\Delta\omega/2} d\omega' \frac{-i(\omega+\omega_0)\chi^{(2)}}{8\pi c}$$
$$\cdot \Bigg[a^*(\omega)a(\omega')a(\omega-\omega_0-\omega')$$
$$- a(\omega)a^*(\omega')a^*(\omega-\omega_0-\omega')$$
$$- 2a(\omega)a^*(\omega')a(\omega'-\omega_0-\omega)$$
$$+ 2a(\omega')a^*(\omega)a^*(\omega'-\omega_0-\omega) \Bigg]. \quad (6.27)$$

The two first terms are transformed under the change of variable

$$\omega \to \omega + \omega_0 + \omega', \quad (6.28)$$

while the two last term are transformed under the change of variable

$$\omega' \to \omega' + \omega_0 + \omega. \quad (6.29)$$

The integration boundaries do not change, as they are limited by the support of $a(\omega)$. This yields

$$\Sigma = \int_{-\Delta\omega/2}^{\Delta\omega/2} d\omega \int_{-\Delta\omega/2}^{\Delta\omega/2} d\omega' \frac{-i\chi^{(2)}}{8\pi c}(\omega-\omega')$$
$$\cdot \Bigg[a(\omega)a(\omega')a^*(\omega+\omega_0+\omega')$$
$$- a^*(\omega)a^*(\omega')a(\omega+\omega_0+\omega') \Bigg]. \quad (6.30)$$

As ω and ω' are dummy integration variable, one has

$$\Sigma = \Sigma(\omega \leftrightarrow \omega'). \quad (6.31)$$

However, from the factor $(\omega-\omega')$ in Eq.6.30, one also has the anti-symmetric result

$$\Sigma = -\Sigma(\omega \leftrightarrow \omega') \quad (6.32)$$

which implies

$$\Sigma = -\Sigma = 0, \quad (6.33)$$

demonstrating that energy is conserved through the anti-aliasing scheme.
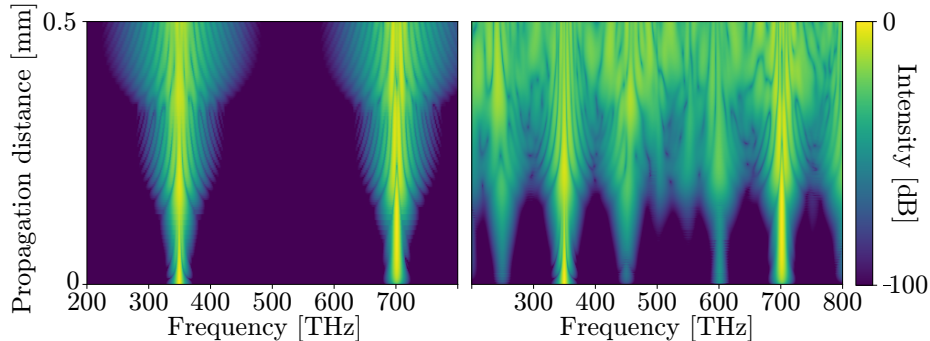
Figure 6.5: Propagation of a short pulse in a zero-group velocity dispersion, quadratic nonlinear medium with and without anti-aliasing. Left panel: with anti-aliasing, the pulse gets efficiently converted to its second harmonic and cascaded nonlinearities induce spectral broadening. Right panel: without anti-aliasing, spurious frequency components get generated during propagation and invalidate the simulation result.

6.6.2 Waveguides geometry

Both, silicon nitride and the lithium niobate waveguides, are on a SiO_2 substrate; only the silicon nitride waveguides are also clad with SiO_2. The dimensions of the lithium niobate waveguide are: length 6 mm, height 800 nm (partially etched, etch depth ca. 580 nm), top width 1400 nm, and sidewall angle 70 deg. The dimensions of the silicon nitride waveguide are: length 5 mm, height 800 nm, top width 800 nm, and sidewall angle 90 deg. The frequency dependent effective refractive indices of both waveguides used for simulating the nonlinear spectral generation were obtained via finite element modeling, taking into account the frequency dependent bulk refractive indices.

6.6.3 Comparison with an established solver

As an additional validation of the new numeric tool, we compare it to results obtained through an established solver in the context of SPM-based (and Raman scattering) supercontinuum generation [192]. The simulation results are shown in Fig. 6.6 and should be compared to Fig. 3 in Ref. [192].

6.6.4 Propagation results

For completeness, the frequency- and time-domain propagation for each case presented in the main text are given here. Fig. 6.7 illustrates the simulated propagation in the lithium niobate platform, Fig. 6.8 in the silicon nitride and Fig. 6.9 shows an example of cascaded nonlinearities.
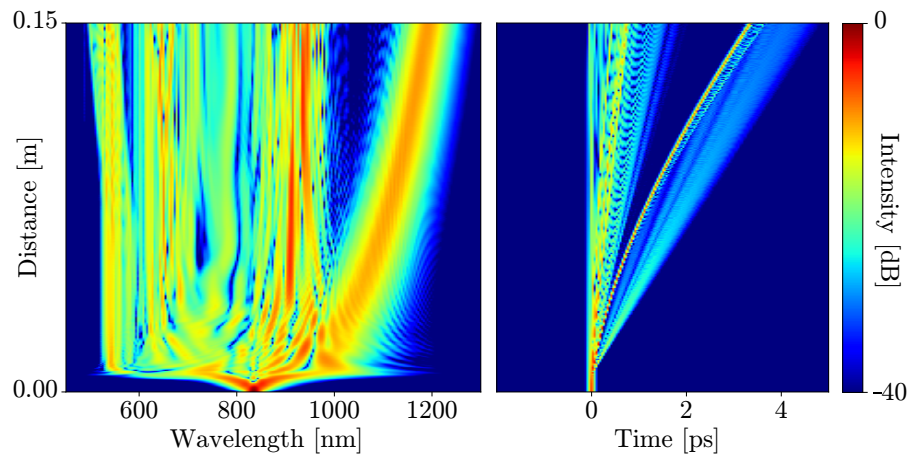
Figure 6.6: Simulated supercontinuum generation reproducing the results of Fig. 3 in ref. [192]
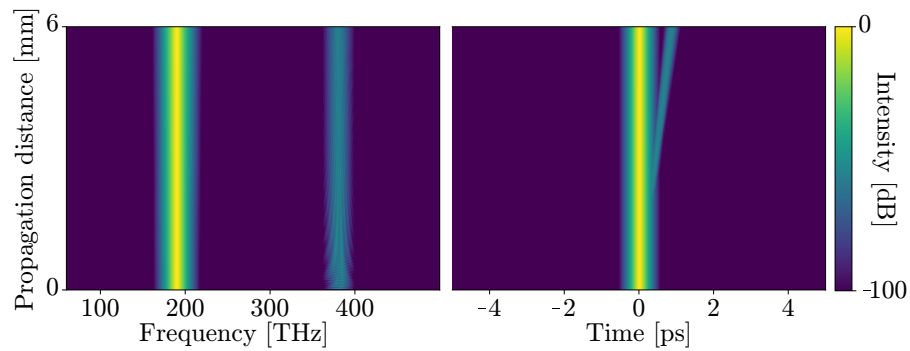
Figure 6.7: Frequency- and time-domain propagation of the pulse in the lithium niobate platform (cf. Fig. 6.2).
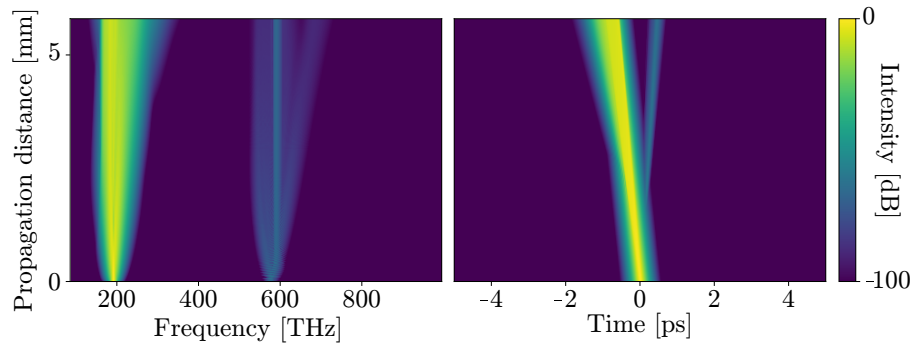
Figure 6.8: Frequency- and time-domain propagation of the pulse in the silicon nitride platform (cf. Fig. 6.3).
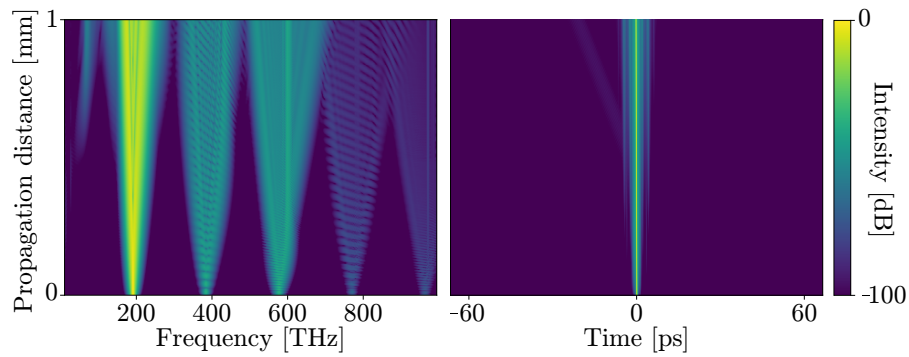
Figure 6.9: Frequency- and time-domain propagation of a pulse in a hypothetical waveguide leading to cascaded nonlinearities (cf. Fig. 6.4).

Chapter 7

Summary and outlook

In this thesis, we explored the opportunities presented by high mutual coherence, high repetition rate dual-comb spectrometers. Through broadband optical coverage, as well as, the possibility to operate at high and low acquisition rates, such systems enable novel techniques for optical molecular spectroscopy and beyond.

In Chapter 2, we demonstrated that the high mutual coherence of a 1 GHz electro-optic dual-comb spectrometer can be leveraged to achieve a compression ratio of 10^7 from optical to acoustic frequencies. This characteristic enabled the demonstration of photo-acoustic dual-comb spectroscopy, which combines the advantages of a photo-acoustic detection scheme with those of dual-comb spectroscopy. The community's strong enthusiasm towards the new technique has been evidenced by multiple publications on the subject: in 2020, Friedlein et al. from the National Institute of Standards and Technology, Boulder, USA [112] published in the same issue of Nature Communications the application of dual-comb photo-acoustic spectroscopy to polymer films, highlighting the technique's versatility. Follow-up work on photo-acoustic dual-comb spectroscopy has been reported in [233, 234], while applications of the technique in acoustic comb generation [235] have been demonstrated. The technique has recently been combined with resonant cavities, leading to the development of dual-comb optomechanical spectroscopy [236].

In Chapter 3, real-time dual-comb hyperspectral imaging has been demonstrated by pushing the compression ratio of the high mutual coherence spectrometer even further to enable the use of an infrared detector array. By using a neural network for fast data reduction, the technique permits the capture and processing of hyperspectral images at high spectral and spatial resolution with a 10 Hz refresh rate. This publication was gratified with Optics Letters' editor's pick. Noticeable interest has since been demonstrated towards dual-comb hyperspectral imaging in follow-up works (e.g. [117, 237]) and led to the development of its natural extension, dual-comb holography [38].

Even without spectral extension, the simplicity and robustness of high coherence, high repetition rate electro-optic dual-comb spectrometers offer unique

opportunities as dedicated high precision measurement systems. The high mutual coherence electro-optic dual-comb system built for these projects has been later transferred to the University in Toruń, Toruń, Poland, where Charczun et al. [35] demonstrated its application to dual-comb cavity-mode width and shift spectroscopy. Later, at the same institute and with the same system, Lisak et al. [36] performed the first instance of dual-comb cavity ring-down spectroscopy.

To fully benefit from the advantages in bandwidth and acquisition rate of high repetition rate dual-comb spectroscopy, a high mutual coherence Erbium-based 1 Ghz dual-comb spectrometer was built and used to perform fast and broadband spectroscopy in Chapter 4. This work reported the first 1 GHz dual-comb spectrometer with Erbium mode-locked lasers, and the third overall demonstration of a dual-comb spectrometer based on 1 GHz mode-locked lasers after the works of I. Hartl et al. [142] with Ytterbium lasers and K. J. Mohler et al. [143] with Titanium-Sapphire lasers. In addition, the versatile, FPGA-based stabilization scheme used offers opportunities to streamline the operation of such systems and to achieve real-time data processing. The appeal of digital control schemes has manifested in multiple publications in recent years, e.g. in [86, 99, 150]. Prior to this publication, significant efforts had been deployed to achieve 1 GHz repetition rate dual-comb spectroscopy [144, 145] in the Erbium region, although the proposed techniques were inherently limited in bandwidth. An architecture based on the same oscillators later demonstrated operation in the mid- [238] and far-infrared [26] and high repetition-rate dual-comb spectrometers are getting increasing attention.

The optical coverage provided by this spectrometer was then leveraged to demonstrate a novel calibration technique for astronomical spectrographs relying on the spectroscopic measurement of a calibration cavity in Chapter 5. The technique provides the full chromatic dispersion of a Fabry-Pérot calibrator, which permits the determination of the resulting calibration markers with comb precision. The approach is based on mature technology and does not require the operation of astrocombs, opening new opportunities for low repetition rate lasers to calibrate astronomical spectrographs. The demonstrated standard deviation on the resonant frequencies of the cavity has been determined to be comparable to state-of-the-art calibrators, reaching down to 25 cm/s for a ~ 0.4 s measurement and enabling calibration on a level suitable for the search of Earth-like exoplanets. Although the manuscript is still in preparation, the technique is expected to have a strong impact on the development of calibration methods for astronomical spectrographs as an appealing alternative to astrocombs. The robustness, reliability and cost-efficiency of the system is particularly suited to observatories without access to astrocombs.

In Chapter 6, to push broadband operation even further, a software was developed to simulate nonlinear light interactions, providing a path towards the spectral extension of these high repetition rate systems. This work took inspiration from an open-source software simulating self-phase modulation of short pulses named pyNLO [221] for its general structure. The publication was gratified with APL Photonics' editor's pick. It has found applications since in the work of Ludwig et al. from DESY, Hamburg, Germany [239], that achieved
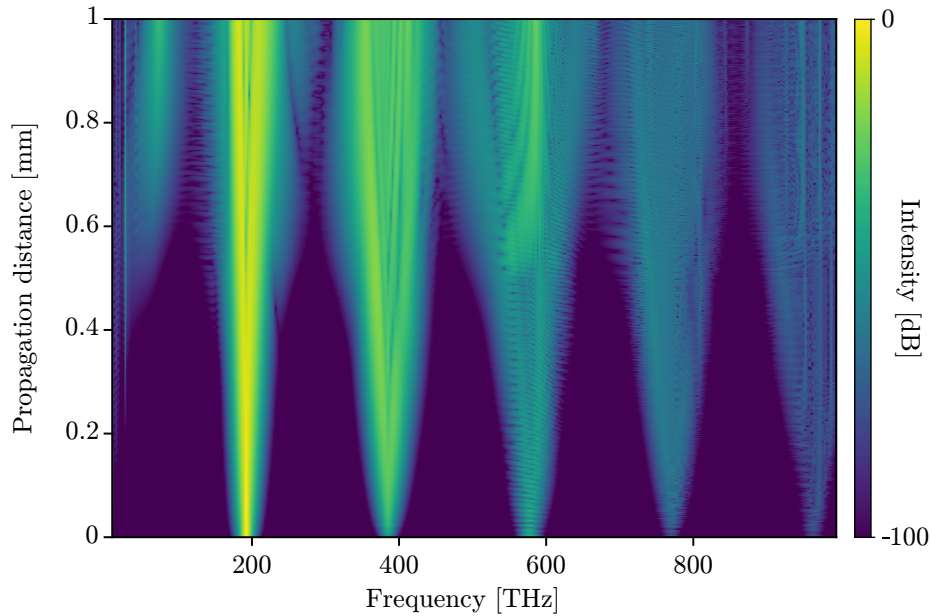
Figure 7.1: Simulation of the propagation of a short near-infrared pulse in a poled Lithium Niobate waveguide resulting in broadband visible light generation.

frequency conversion of an 18 GHz electro-optic comb from the near-infrared down to the ultraviolet region for astronomical spectrograph calibration, and we expect further work to leverage the software. Extensions of the demonstration combining dual-comb spectroscopy with Fabry-Pérot calibration of astronomical spectrographs could highly benefit from the software, bringing the operating range to the visible using waveguide structures comparable to those in the work of Ludwig et al. [239] or Obrzud et al. from CSEM, Neuchâtel, Switzerland [204].

An example of the propagation of a short pulse with parameters corresponding to those of the dual-comb spectrometer in a poled Lithium Niobate waveguide is presented in Fig. 7.1, showcasing a possible spectral extension to the visible region. This particular structure was designed with two successive periodic polings each occupying half of the waveguide's length. The first poling matches the pump wavelength to the second harmonic, while the second poling matches the pump and the second harmonic to the third harmonic, resulting in intense visible light.

In light of these demonstrations, it is clear that high mutual coherence, high repetition rate dual-comb spectrometers offer a large spectrum of exciting applications in molecular spectroscopy and beyond. These systems have received a strong interest of the optics community in the last few years and led to the development of multiple new combinations of dual-comb spectroscopy with spe-

cialty detection techniques. It is expected that this field of optical spectroscopy will continue to flourish in the near future, as multiplexed sources with natively high mutual coherence are being developed and refined (see e.g. [24]). In addition, with the spectral broadening that integrated photonics chips can provide, the optical coverage and versatility of such spectrometers have the potential to reach impressive performances.

Appendix A

Dual-comb spectrometer with 1 GHz mode-locked lasers

In this section, some of the critical components that enabled the realization of a high mutual coherence dual-comb spectrometer based on 1 GHz Erbium mode-locked lasers (Menhir-1550 from Menhir Photonics AG) are detailed. The information presented here is complementary to Chapter 4. The spectrometer is built so as to be transportable, in order to facilitate future out-of-lab experiments. The dual-comb spectrometer is built according to the architecture shown in Fig. A.1, as explained in Chapter 4. The continuous wave laser used in the setup is a Koheras Adjustik from NKT Photonics with central wavelength of 1560 nm. The different modules are detailed hereafter.
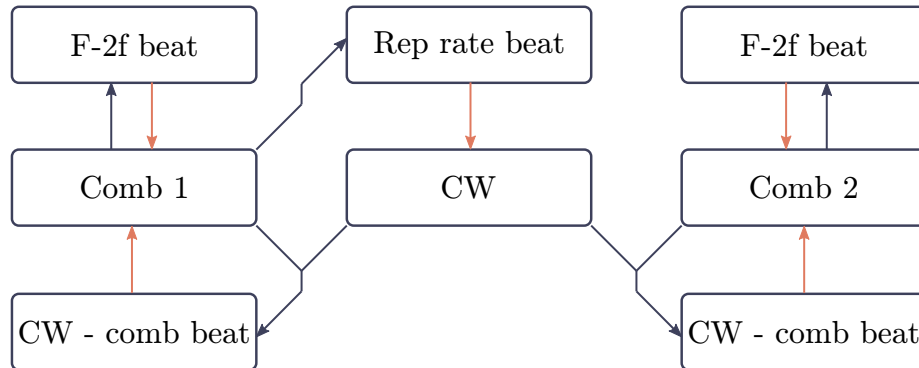
Figure A.1: Architecture of the dual-frequency comb control loops. Blue lines show optical paths to different detection modules, while orange lines denote the resulting control signals sent to the lasers. CW: continuous wave laser.
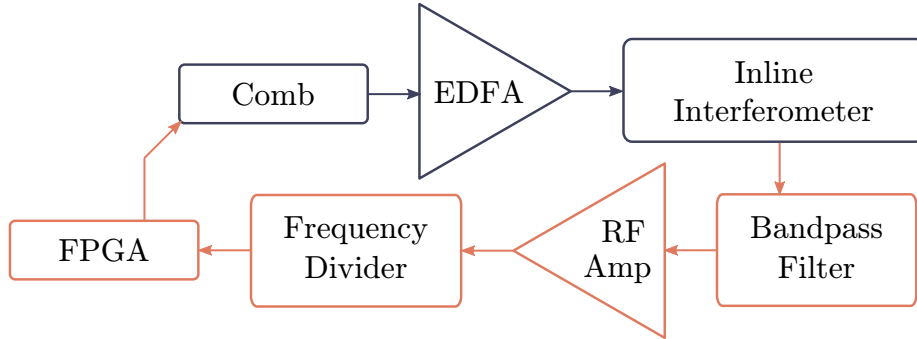
Figure A.2: Components of the f-2f modules, see details in text. EDFA: Erbium-doped fiber amplifier, RF Amp: radio frequency amplifier, FPGA: field-programmable gate array.

A.1 F-2f beatnote modules

To achieve a high mutual coherence between the two frequency combs, it is essential to lock the offset frequencies of both combs to a stable reference. To this end, two nearly identical f-2f interferometer are constructed. These f-2f modules are responsible for detecting the carrier envelope offset frequency of the combs and provide an error signal to phase lock this offset by modulating the comb's pump current. While the design of the inline f-2f interferometers themselves is relatively standard, the use of 1 GHz repetition rate frequency comb complicates the generation of the required octave spanning spectrum and requires a purposely-developed optical amplification and compression process. As depicted in Fig. A.2, the f-2f modules consist of a dispersion-compensated optical amplifier and an inline interferometer to detect the offset beatnote. This beatnote is then filtered and amplified, before being divided to fit within the bandwidth of an FPGA-based module. The FPGA-based module then generates an error signal to stabilize the detected beatnote against an RF reference that can be provided to the FPGA or generated internally.

A.1.1 Dispersion-compensated amplifiers

Critical to the broadening process, amplifiers with compensated dispersion were built and are detailed here. The amplifiers are using a commercially available modular mechanical platform providing mechanical stability, protection and facilitated transport. An overall picture of an (open) amplifier can be seen in Fig. A.3. The amplifier is pumped in a forward-backward configuration with two 3 W diodes and uses a double-clad Erbium-doped fiber for amplification. The splices from the wavelength division multiplexers to the Erbium-doped fiber are coated with a low refractive index glue on aluminum heat sinks. A certain amount of dispersion compensating fiber is added before the amplifier and optimized via a cut-back method to yield the shortest pulses out of the amplifier.
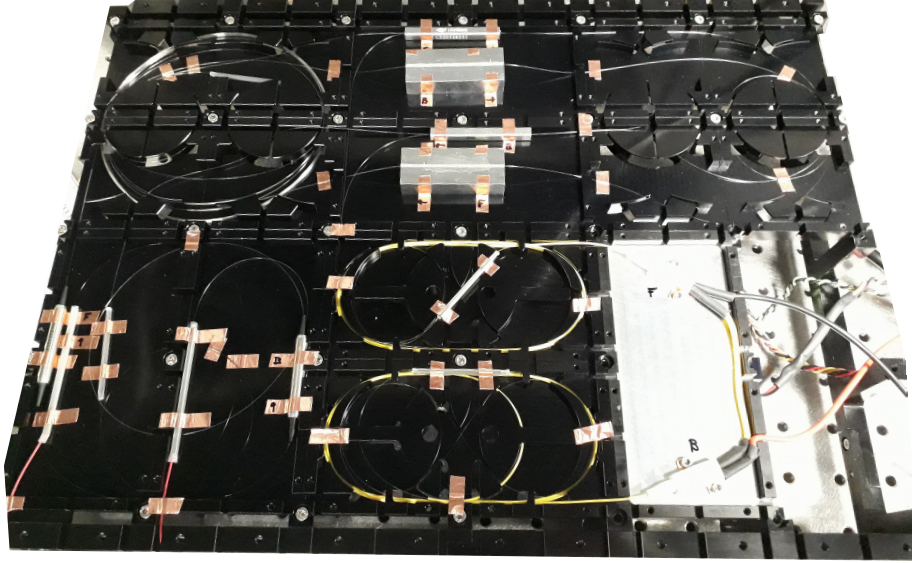
Figure A.3: Photograph of the insides of a dispersion-compensated amplifier.

Component	Part number	Provider	Notes
DCF	PM2000D	Coherent	2 m
2x Isolators	HPMIS-D-F-250-5-0.8-5.5x35-S5	Optosun	50 cm
1x Forward WDM	PMMPC-(1+1)*1-F-976/3W-1550-110/604-604-C1-1m	LightComm	50 cm
1x Backward WDM	PMMPC-(1+1)*1-B-976/3W-1550-110/604-604-C1-1m	LightComm	50 cm
Erbium-doped fiber	DCF-EY-10/128-PM	Coractive	6.5 m
Low-index glue	SPC-373AP	Efiron	-
2x Pump diodes	K976AB2RN-3.000WN0N-10522F20ENA0	BWT Beijing	3 W
Current controller	LD5CHA	Wavelength Electronics	5 A

Table A.1: Components used to build the dispersion-compensated amplifiers.
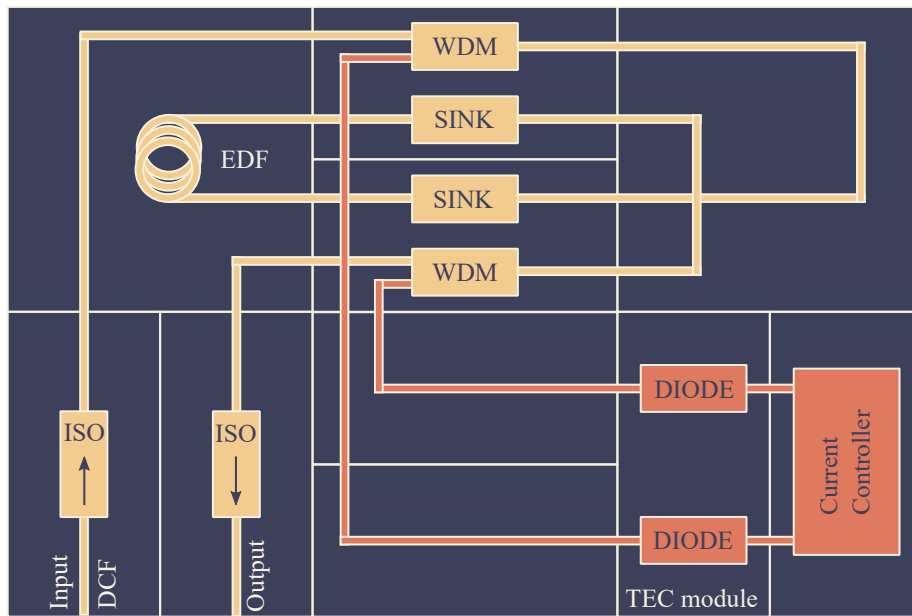
Figure A.4: Schematic of a dispersion-compensated amplifier matching the general layout visible in Fig. A.3. DCF: dispersion compensating fiber, ISO: isolator, WDM: wavelength division multiplexer, SINK: heat sink, DIODE: pump diode.
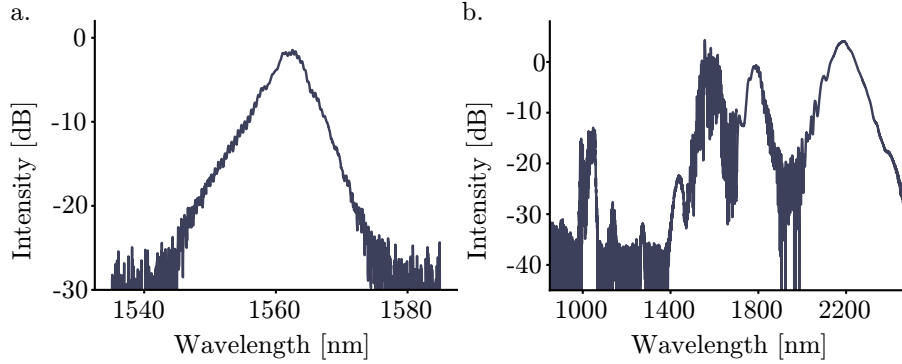
Figure A.5: **a.** Typical output spectrum of the dispersion-compensated amplifier when seeded with a strongly dispersed pulse. **b.** Supercontinuum with Raman-shifted soliton and dispersive wave at the input of the inline f-2f interferometer.

From input pulses of 500 fs duration and 15 mW average power, the amplifier provides output pulses of $\sim$ 100 fs duration with $\sim$ 1 W average power. These pulses are then sent through a highly nonlinear fiber to achieve an octave spanning spectrum for the f-2f interferometer. The detailed amplifier's components list, including the length of the respective fibers, is given in Tab. A.1, while a schematic of the amplifier configuration is given in Fig. A.4.

The amplifiers performed reliably and consistently, and a total of five copies of this model were built for various usage in the laboratory. The output spectrum after amplifying a strongly dispersed pulse can be seen in Fig A.5a, corresponding to an amplification free of self-phase modulation. Note that the weak modulations are due to the fiber patchcord used to disperse the pulse, preceding the amplifier.

A.1.2   Inline interferometers

After amplification and compression in the amplifiers, the pulses are coupled into 2 meters of Raman-shifting highly nonlinear fiber that spectrally broaden the pulses to an octave, as shown in Fig. A.5b. A photograph of the inline interferometer used to detect the f-2f beatnote can be seen in Fig. A.6. Light from the highly nonlinear fiber is collimated and focused into a periodically-poled Lithium Niobate crystal in order to double the frequency of the 2 micron Raman-shifted soliton, so that it overlaps in frequency with the supercontinuum's dispersive wave. This part of the spectrum around 1 micron is then isolated by a dichroic filter and a bandpass filter and detected with an amplified photodetector, leading to a $\geq$ 30 dB carrier envelope offset frequency beatnote.
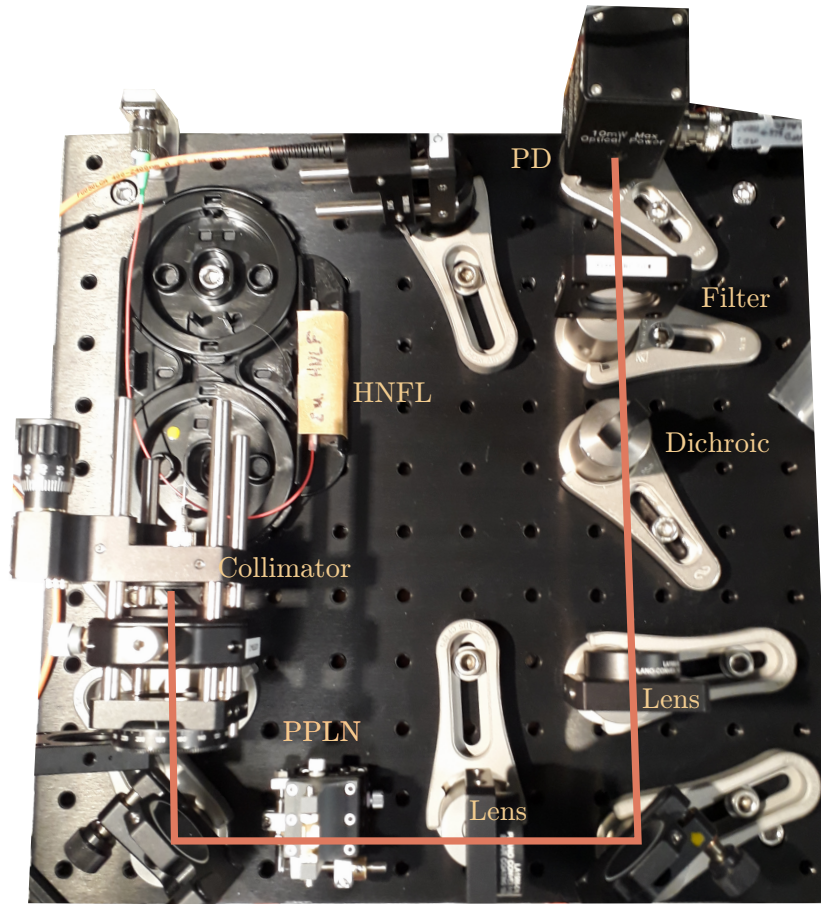
Figure A.6: Inline f-2f interferometer. The optical path is highlighted with an orange line, see details in text. HNLF: highly nonlinear optical fiber, PPLN: periodically-poled Lithium Niobate, PD: amplified photodetector.
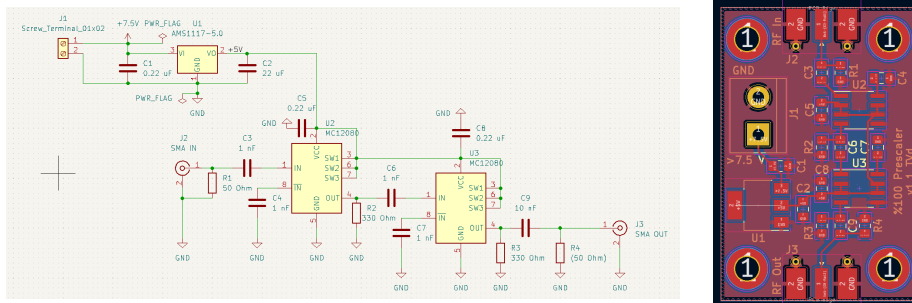
Figure A.7: Schematic and PCB layout for a divide-by-hundred frequency divider.

A.1.3 Frequency dividers

After filtering by a tunable bandpass filter, the offset beatnote is amplified with a radio frequency amplifier. To achieve stabilization of the beatnote against a stable reference, an FPGA-based digital locking scheme is used. The analog-to-digital converters have a limited sampling rate of 125 MHz, and thus are not capable of directly sampling a 500 MHz signal. Consequently, frequency dividers are used to scale the detected beatnote down. However, it was found during experimentation that commercially available frequency dividers are quite expensive, have a long delivery time and have a tendency to cease functioning.

Homemade frequency dividers were thus designed, tested and used instead of commercially available solutions. As an example, we present here a hundred-fold divider. This particular design relies on cascading two divide-by-ten frequency dividers, the rest of the circuit providing power supply stabilization and 50 Ohm impedance matching. The schematic of the design with the components can be found in Fig. A.7 along with the PCB layout. The frequency divider has a typical output power of 0 dBm and works with input frequencies from 100 MHz to 1.6 GHz, with typical input powers from -10 to 10 dBm.

Further modifications of the circuit led to the development of frequency dividers with adjustable division factors of 10, 20, 40 and 80, with similar performances, although operating down to 10 MHz.

A.1.4 FPGA

The FPGA boards used for each control loop are Red Pitaya 125-14. They are controlled via a slightly modified version of *pyrpl* [150] that accommodates a 10 MHz reference input for the board. The interfacing to the board is made via python, and the state of locks as well as the inputs and error signals can be monitored in real-time from a desktop computer. The control loops are optimized by modifying the control parameters while monitoring the phase noise of the beatnotes.

In the case of the f-2f lock, the output control signal of the Red-Pitaya is amplified from a -1 to 1 V range to a -5 to 5 V range, and connected to the current modulation input of the mode-locked laser, resulting in a locked beatnote with a residual phase noise of 620 mrad integrated over from 10 MHz to 100 Hz, see Fig. 4.1.

A.2 CW - frequency comb beatnote modules

Once the offsets of the combs have been stabilized, the repetition rates of the frequency combs still need to be controlled. As the noise on the repetition rate beatnote is multiplied by a factor $\sim 10^5$ in the optical domain (corresponding to the optical mode numbers), the approach adopted here does not rely on stabilizing the repetition rate beatnote against a radio frequency reference directly. Instead, a transfer continuous wave laser with low noise is used to anchor an optical line of each comb in the optical domain, resulting in low noise on each
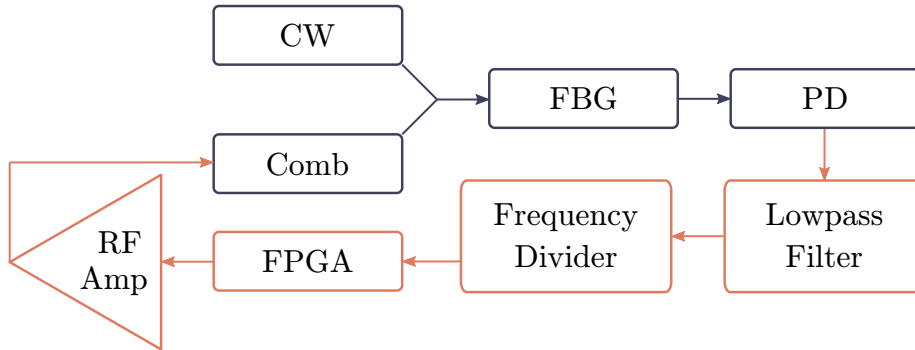
Figure A.8: Architecture of the modules used to lock an optical line of a frequency comb to a continuous wave laser. CW: Continuous wave laser, FBG: Fiber Bragg grating, PD: amplified photodetector, FPGA: field-programmable gate array, RF Amp: radio frequency amplifier.

comb's repetition rate. Additionally, as both combs are locked to the same continuous wave laser, fluctuations in the center frequency of the continuous wave laser disappear from the heterodyne signal as discussed in Chapter 1. The overall architecture of the modules responsible for these locks is presented in Fig. A.8. For portability, these modules were assembled inside rack-compatible mounts.

Using a fiber splitter, light from the comb and the continuous wave laser is combined and sent in a fiber Bragg grating. This grating acts as a very narrow bandpass filter, which removes unnecessary comb lines. An amplified photodetector delivers the beatnotes to a lowpass filter with a 500 MHz bandwidth, which removes all but the beatnote between the continuous wave laser and the nearest comb line. Analogous to the f-2f module, this beatnote is divided down using a frequency divider, and sent to an FPGA. The control loop is implemented in the FPGA and the resulting error signal is strongly amplified to a range of 0-125 V to drive the piezo actuators of the frequency comb, resulting in an optical lock with a residual phase noise of 120 mrad integrated from 10 MHz to 100 Hz (see Fig. 4.1).

A.3 Repetition rate beatnote module

Finally, the last remaining degree of freedom of the system that remains to be stabilized is the center frequency of the continuous wave laser. The module responsible for this is depicted in Fig. A.9. As the frequency combs are locked to the continuous wave laser, a change in its frequency results in variations on the repetition rate of both lasers. Consequently, the repetition rate of one of the comb can be used as the monitoring signal for the center frequency of the continuous wave laser. The repetition rate of the first comb is thus detected by
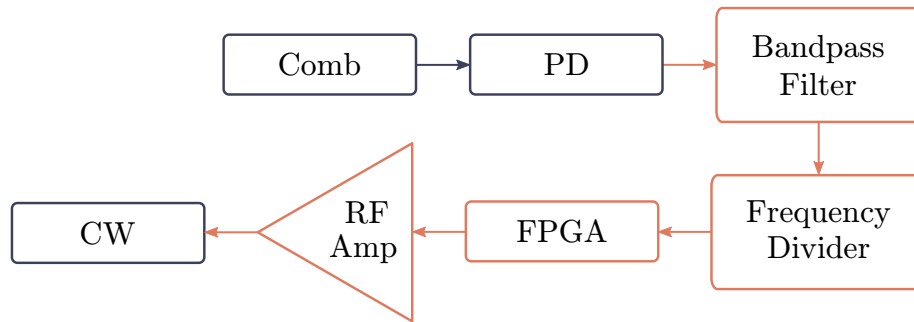
Figure A.9: Architecture of the module used to lock the center frequency of the continuous wave laser. CW: Continuous wave laser, PD: amplified photodetector, FPGA: field-programmable gate array, RF Amp: radio frequency amplifier.

directly shining around 0.5 mW of its light on an amplified photodetector. The beatnote is then bandpass filtered around 1 GHz, divided down by a frequency divider and sent to an FPGA to generate an appropriate error signal. This error signal is then amplified and used to actuate the central frequency of the continuous wave laser, resulting in a fully stabilized dual-comb interferometer with high mutual coherence.

Appendix B

Dual-comb data acquisition and processing

In this Chapter, a discussion of the workflow of data acquisition and processing in dual-comb spectroscopy is presented. Useful resources for this Chapter can be found in e.g. [240, 94, 95, 83, 28, 93, 40, 77, 97]

B.1   Data acquisition

To properly resolve a dual-comb signal, the heterodyne interferogram needs to be adequately recorded. The photodetector used to detect the optical signal should have a radio frequency bandwidth of at least $f_{rep}/2$, to capture the lowest frequency radio frequency comb in its entirety. A low-pass filter is usually used to keep only this radio frequency comb, removing the unnecessary contributions from higher order beatnotes. Accordingly, the digitizer used to record the photodetector's voltage needs to achieve a sampling frequency of at least f_{rep}. Depending on the repetition rate of the considered system, these requirements can demand specialized equipment. In addition, the amount of data generated during an acquisition can become prohibitively large depending on the sampling rate of the digitizer and might require direct data reduction by on-the-fly coherent averaging. In certain cases, as in Chapter 2 and Chapter 3, these requirements can be lowered if the entire radio frequency comb is compressed close to DC, which relaxes the requirements on the detector's bandwidth and the sampling rate of the digitizer, but requires high mutual coherence between the frequency combs.

B.2   Coherent averaging

Coherent averaging of a dual-comb signal can be achieved if the interferograms are periodic and can be directly averaged in the time domain. This approach

has the benefit of necessitating the Fourier transform of a single, averaged inter-
ferogram to retrieve the quantities of interest, rather than a Fourier transform
of the entire, unaveraged trace, and thereby also strongly reducing the required
memory.

For the interferograms to be periodic, the parameters of the system need
to be chosen carefully. In particular, as an interferogram has a duration of
$1/\Delta f_{rep}$, the periodicity requirement is

$$
\begin{aligned}
i_{DCS}(t) &\propto \sum_n \sum_m A_n^* A_m' e^{2\pi it(m\Delta f_{rep}+\Delta f_{ceo})} e^{2\pi it(m-n)f_{rep}} \\
&= \sum_n \sum_m A_n^* A_m' e^{2\pi i(t+1/\Delta f_{rep})(m\Delta f_{rep}+\Delta f_{ceo})} e^{2\pi i(t+1/\Delta f_{rep})(m-n)f_{rep}}
\end{aligned}
\tag{B.1}
$$

which leads to

$$
\Delta f_{ceo} = k\Delta f_{rep},
\tag{B.2}
$$

with k an integer, as well as,

$$
(m-n)f_{rep} = l\Delta f_{rep},
\tag{B.3}
$$

with l an integer. Consequently, the interferograms will be periodic if Δf_{ceo}
and f_{rep} are multiples of Δf_{rep}.

These conditions are however not sufficient to achieve direct coherent aver-
aging, as there is no guarantee that the sampling system is synchronized to the
interferograms a priori. Accordingly, the sampling rate f_s must be chosen so
that each interferogram is recorded with an integer number of samples, leading
to the additional requirement

$$
f_s = p\Delta f_{rep},
\tag{B.4}
$$

with p an integer.

If these conditions are fulfilled, the interferograms can be directly coherently
averaged in the time domain for a time corresponding to the mutual coherence
of the dual-comb spectrometer.

With a digital control system, fulfilling these conditions might require ad-
ditional care. In particular, if the control system can only provide locking to
certain frequencies in discrete increments, one must ensure that the potential
interplay with frequency dividers will result in coherent averaging conditions.

B.3   Phase correction

To go beyond the mutual coherence time of a dual-comb spectrometer, post-
processing can be applied to series of interferograms. Alternatively, these cor-
rection techniques can be used to make interferograms periodic a posteriori.
Different techniques can be deployed to these ends, although the overall phi-
losophy stays unchanged: for each interferogram, a deviation from the nominal
repetition rate difference and offset frequency difference is computed and then
corrected.

B.3.1   Computing deviations

The deviations in repetition rate difference and offset frequency difference can be recovered in different ways. The first method proposed here provides a good approximation of the deviations for high mutual coherence systems operating close to coherent averaging conditions.

In general, an interferogram can be Fourier transformed and the phase of each of its spectral component retrieved. The phases of the first interferogram of the series can be defined as references, and set to zero without loss of generality. We thus define the series of recorded, low-pass filtered interferograms by

$$I(t) = \sum_n V_n e^{2\pi i t (n(\Delta f_{rep} + \delta f_{rep}(t)) + \Delta f_{ceo} + \delta f_{ceo}(t))}, \tag{B.5}$$

where the variations in repetition rate difference and offset difference have been explicitly written. Note that this complex quantity is obtained through the analytical continuation of the digitized voltage via a Hilbert transform. After an expected period of $1/\Delta f_{rep}$, one obtains (dropping the time dependence of the variations)

$$I(t + 1/\Delta f_{rep}) = \sum_n V_n e^{2\pi i t (n\Delta f_{rep} + \Delta f_{ceo})}$$
$$\cdot e^{2\pi i t (n\delta f_{rep} + \delta f_{ceo})}$$
$$\cdot e^{2\pi i (n\delta f_{rep}/\Delta f_{rep} + \delta f_{ceo}/\Delta f_{rep})}. \tag{B.6}$$

This expression makes it clear that the second interferogram of the series will have a non-zero phase of its spectral components due to the last exponential, which does not display a t exponent. In addition, from the n prefactor, the linear slope of this spectral phase is $2\pi\delta f_{rep}/\Delta f_{rep}$, while its overall offset is $2\pi\delta f_{ceo}/\Delta f_{rep}$. The deviations can thus be easily recovered by Fourier transforming each subsequent interferogram and tracking their spectral phases.

The limitations of this approach manifest themselves in the second exponential of Eq. B.6, which is responsible for a (small) frequency shift of the radio frequency comb's teeth. This shift is not coherently sampled by the system and leads to spurious leakage during Fourier transformation, preventing a perfect reconstruction of the deviations. Another disadvantage of this technique is the requirement that every interferogram should be entirely Fourier transformed, which can be time consuming for data-heavy applications.

An appealing, although more involved alternative method free of these shortcomings avoids Fourier transforms altogether to prevent spectral leakage. Consider

$$|I(t)|^2 = \sum_m \sum_n V_n V_m^* e^{2\pi i t (n-m)(\Delta f_{rep} + \delta f_{rep})}, \tag{B.7}$$

which corresponds to the analytical envelope of the interferogram. This quantity is free from deviations of the offset difference frequency. By finding the maximum of this quantity for successive interferograms, one can monitor the

variation in the position of the center burst of successive interferograms, which by definition directly gives $1/(\Delta f_{rep} + \delta f_{rep})$. As a benefit, only a small portion of the interferograms near the center burst needs to be considered, permitting fast processing times. In the case where the center burst of the interferograms are poorly defined, a more costly cross-correlation can be used to determine the variation in the interferograms' timing.

After these variations are corrected (as will be explained below), the interferograms only contain variations in the offset frequency difference, i.e.

$$I(t) = \sum_n V_n e^{2\pi i t (n\Delta f_{rep} + \Delta f_{ceo} + \delta f_{ceo})}. \tag{B.8}$$

One can compute the polar angle of this complex quantity to find the temporal phases around the center burst of the interferogram

$$\angle I(t) = 2\pi t \delta f_{ceo} + \angle \left(\sum_n V_n e^{2\pi i t (n\Delta f_{rep} + \Delta f_{ceo})} \right). \tag{B.9}$$

The second term in this expression can be easily retrieved from the first interferogram, as it has $\delta f_{ceo} = 0$ by definition. Then, a direct subtraction with this reference provides the wanted δf_{ceo} variation for each interferogram. This algorithm is quite efficient, in that entire Fourier transformation of the interferograms are not required.

B.3.2 Correcting deviations

Once the deviation in Δf_{rep} has been computed, the series of interferograms can be corrected. To do so, a modified time grid

$$\tau(t) = t \left(1 + \frac{\delta f_{rep}(t)}{\Delta f_{rep}} \right) \tag{B.10}$$

is computed, which leads to

$$I(t) = e^{2\pi i t (\Delta f_{ceo} + \delta f_{ceo}(t))} \sum_n V_n e^{2\pi i n \tau(t) \Delta f_{rep}}, \tag{B.11}$$

so that

$$I(\tau^{-1}(t)) = e^{2\pi i \tau^{-1}(t)(\Delta f_{ceo} + \delta f_{ceo}(\tau^{-1}(t)))} \sum_n V_n e^{2\pi i n t \Delta f_{rep}} \tag{B.12}$$

is corrected in repetition rate difference deviation, by interpolating $I(t)$ on the linear time grid $\tau(t)$. The temporal phase of the prefactor exponential can be easily computed as explained above and a simple multiplication yields the corrected series of interferograms

$$I_{corr}(t) = e^{2\pi i \tau^{-1}(t)(\Delta f_{ceo} + \delta f_{ceo}(\tau^{-1}(t)))} I(\tau^{-1}(t)) = \sum_n V_n e^{2\pi i n t \Delta f_{rep}}. \tag{B.13}$$

As $I_{corr}(t)$ has $\Delta f_{ceo} = 0$ and is free of repetition rate difference deviations, it can be coherently averaged for as long as desired.

B.3.3 Limitations of phase correction

This phase correction technique has limits in the bandwidth of the noise that it can remove. As a single correction value for Δf_{rep} and Δf_{ceo} can be computed per interferogram, the technique effectively samples deviations with a rate of Δf_{rep}. This implies that any noise with frequency higher than $\Delta f_{rep}/2$ will not be captured and corrected by the technique. This observation motivates the use of high coherence systems that possess low noise overall and pushes towards operating these systems at high acquisition rates (i.e. high Δf_{rep}).

Another practical limitation of the technique comes from additional noise sources. The model considered in this section was free of any noise other than on the repetition rate difference and the offset frequency difference, while a physical system will exhibit e.g. intensity noise, detection noise, thermal noise. These contributions will affect the values of the computed deviations and slightly distort the expected results after correction. Advanced models relying on Kalman filters have been proposed to maximize the efficiency of correction techniques even with additional noise sources [240].

B.3.4 Example

For the interested reader, the following *python* implementation generates a series of noisy interferograms and uses the algorithms described above to correct them.

```
"""
This program generates interferograms with random fceo and frep
noise and uses a phase correction technique to recover coherently
averageable interferograms.
"""


import numpy as np
import matplotlib.pyplot as plt
plt.close('all')
from scipy.interpolate import interp1d
from scipy.signal import find_peaks


"""
Computing interferograms
"""
# Parameters
time = np.linspace(0, 0.99999, int(1e5))
spectral_elements = 50
frep = 50
fceo = 5000
bins_per_int = len(time)//frep

# Perfect interferograms
```

```
perfect_int = np.zeros(len(time), dtype=complex)
for i in np.arange(spectral_elements):
    perfect_int += np.exp(2j*np.pi*(time-1/2/frep)*(i*frep + fceo))

# Noisy interferograms
prep_noisy = 0.2*(np.random.rand(frep) - 0.5)
pceo_noisy = 0.5*(np.random.rand(frep)  - 0.5)
noisy_int = np.zeros(len(time), dtype=complex)
for i in np.arange(spectral_elements):
    for j in np.arange(frep):
        noisy_int[j*bins_per_int:(j+1)*bins_per_int] += \
        np.exp(2j*np.pi*((time[:bins_per_int]-1/2/frep)\
        *((i+fceo//frep)*frep) + prep_noisy[j]*(i+fceo//frep)\
        + pceo_noisy[j]))

# Plots for comparison
plt.figure()
plt.plot(time, perfect_int)
plt.plot(time, noisy_int)
plt.xlim(0, 1)
plt.xlabel('Time [s]')
plt.ylabel('Voltage [a.u.]')
plt.legend(('Perfect interferograms', 'Noisy interferograms'))

freq = np.fft.fftfreq(len(time), np.mean(np.diff(time)))
plt.figure()
plt.plot(freq, np.abs(np.fft.fft(perfect_int)))
plt.plot(freq, np.abs(np.fft.fft(noisy_int)))
plt.xlim(4500, 8000)
plt.xlabel('Frequency [Hz]')
plt.ylabel('Intensity [a.u.]')
plt.legend(('Perfect interferograms', 'Noisy interferograms'))


"""
Computing and correcting frep variations
"""
# Get peaks of envelope
envelope = np.abs(noisy_int)**2
max_ind, _ = find_peaks(envelope, distance = 0.3*bins_per_int,
                        height=1500)

# Refine peak finding with Lagrange polynomial maximum
peak_time = np.zeros(len(max_ind))
for i, ind in enumerate(max_ind):
    num = envelope[ind-1]*(time[ind]+time[ind+1])
```

```
        num -= 2*envelope[ind]*(time[ind-1]+time[ind+1])
        num += envelope[ind+1]*(time[ind-1]+time[ind])
        num /= 2
        num /= envelope[ind-1] - 2*envelope[ind] + envelope[ind+1]
        peak_time[i] = num

# Compute frep phase deviation
prep_meas = 1/2/frep-peak_time%(1/frep)

# Correct frep deviations
prep_int = interp1d(peak_time, prep_meas, 'nearest',
                    bounds_error=False,
                    fill_value='extrapolate')
tau = time + prep_int(time)
int_rep_corr = interp1d(tau, noisy_int, 'linear',
                        bounds_error=False,
                        fill_value='extrapolate')
int_rep_corr = int_rep_corr(time)

# Plot frep corrected interferograms
cut_int_perf = perfect_int[bins_per_int//2:-bins_per_int//2]
cut_int_rep_corr = int_rep_corr[bins_per_int//2:-bins_per_int//2]
cut_freq = np.fft.fftfreq(len(cut_int_rep_corr), np.mean(np.diff(time)))

plt.figure()
plt.plot(time[:-bins_per_int], cut_int_perf)
plt.plot(time[:-bins_per_int], cut_int_rep_corr)
plt.xlabel('Time [s]')
plt.ylabel('Voltage [a.u.]')
plt.legend(('Perfect interferograms', 'Frep corrected interferograms'))

plt.figure()
plt.plot(cut_freq, np.abs(np.fft.fft(cut_int_perf)))
plt.plot(cut_freq, np.abs(np.fft.fft(cut_int_rep_corr)))
plt.xlim(4500, 8000)
plt.xlabel('Frequency [Hz]')
plt.ylabel('Intensity [a.u.]')
plt.legend(('Perfect interferograms', 'Frep corrected interferograms'))


"""
Computing and correcting fceo variations
"""
# Reshape interferograms
int_rep_corr_resh = np.reshape(int_rep_corr, (frep, len(time)//frep))
```

```
# Compute phases and variation
polar_phases = np.unwrap(np.angle(int_rep_corr_resh), axis=0)
polar_phases -= np.mean(polar_phases, axis=0)
pceo_meas = np.mean(polar_phases, axis=1)

# Correct fceo deviations
pceo_int = interp1d(0.02*np.arange(frep)+0.01, pceo_meas,
                    kind='nearest', bounds_error=False,
                    fill_value='extrapolate')
int_corr = np.exp(-1j*pceo_int(time))*int_rep_corr

# Plot fully corrected interferograms
cut_int_corr = int_corr[bins_per_int//2:-bins_per_int//2]
cut_int_noisy = noisy_int[bins_per_int//2:-bins_per_int//2]
plt.figure()
plt.plot(time[:-bins_per_int], cut_int_perf)
plt.plot(time[:-bins_per_int], cut_int_corr)
plt.xlabel('Time [s]')
plt.ylabel('Voltage [a.u.]')
plt.legend(('Perfect interferograms', 'Fully corrected interferograms'))

plt.figure()
plt.plot(np.abs(np.fft.fft(cut_int_perf)))
plt.plot(np.abs(np.fft.fft(cut_int_noisy)))
plt.plot(np.abs(np.fft.fft(cut_int_corr)))
plt.xlim(4500, 8000)
plt.xlabel('Frequency [Hz]')
plt.ylabel('Intensity [a.u.]')
plt.legend(('Perfect interferograms', 'Noisy interferograms',
            'Fully corrected interferograms'))
plt.savefig('phase_correction.pdf')
```

The typical results from this implementation will resemble Fig. B.1, where the Fourier transform of the ideal, noisy and corrected interferograms can be compared. While the technique does not achieve perfect reconstruction (mostly due to necessary interpolations), it is capable of a strong signal-to-noise ratio recovery, even with barely distinguishable initial comb lines. In the case where the noise of the system is relatively low, an almost perfect reconstruction of the noise-free signal can be achieved as shown in Fig. B.2.
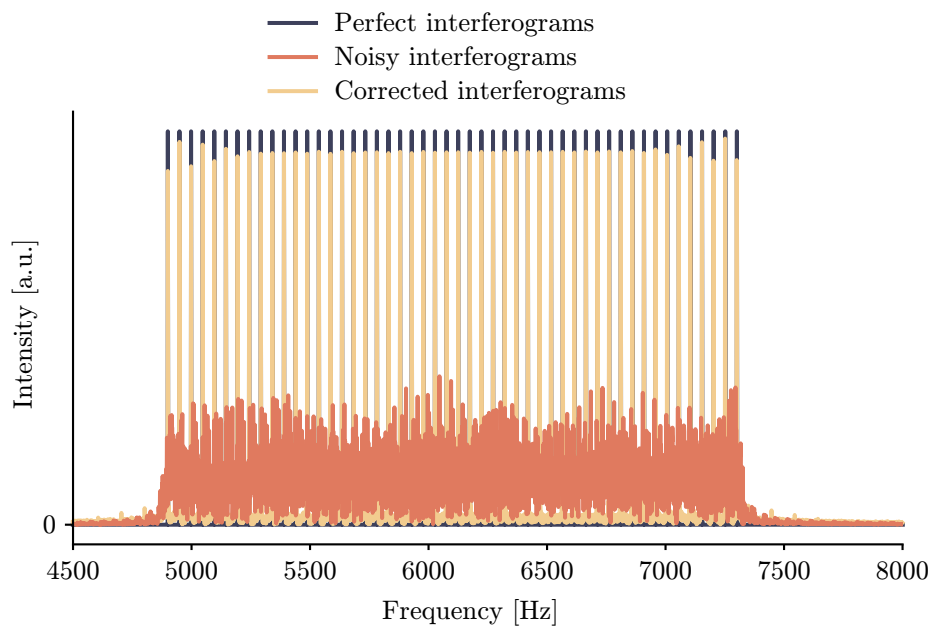
Figure B.1: Example of a phase correction of interferograms with high noise. The Fourier transform of noisy interferograms is shown in orange and displays low signal-to-noise ratio. After phase-correction of the interferograms, the yellow trace is recovered with good signal-to-noise ratio. The Fourier transform of noise-free interferograms is depicted in blue. A perfect reconstruction is not achieved due to the high noise affecting the interferograms.
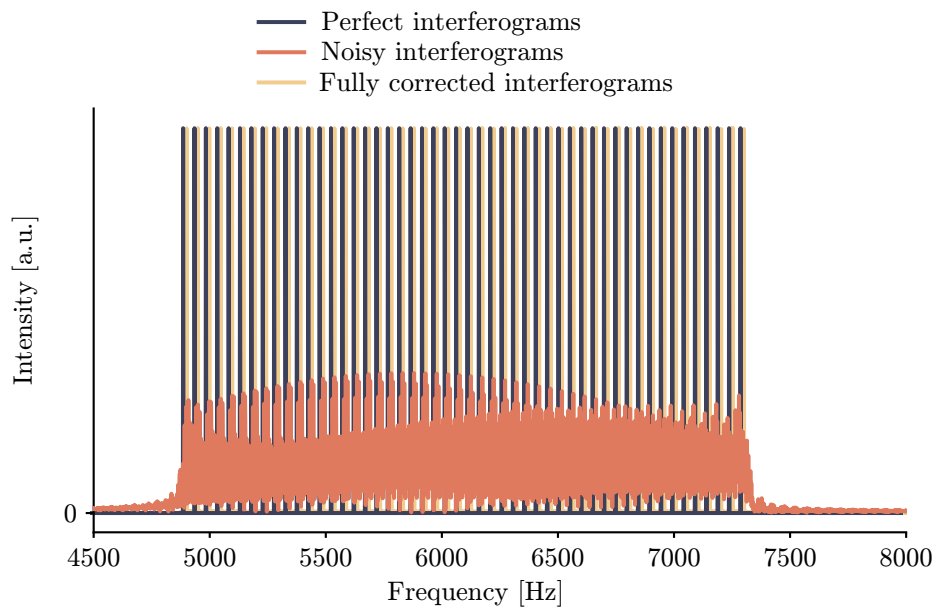
Figure B.2: Example of a phase correction of interferograms with limited noise. The Fourier transform of noisy interferograms is shown in orange and displays low signal-to-noise ratio. After phase-correction of the interferograms, the yellow trace is recovered with excellent signal-to-noise ratio. The Fourier transform of noise-free interferograms is depicted in blue and slightly offset in frequency for comparison.

Appendix C

pyChi

We provide here additional information on the python simulation software pyChi. The software presentation and installation instructions are given based on the GitHub page (https://github.com/pychi-code/pychi). The theoretical background upon which the software is built is presented in a second part.

C.1 Software

C.1.1 Capabilities

pyChi is aimed at simulating the propagation of short pulses in nonlinear media and capturing as much physics as possible. It is based on a unidirectional propagation model, which stays valid even for sub-cycle optical pulses. In particular, this propagation model accounts for

- Full frequency dependence of the effective refractive index

- Quadratic nonlinear interactions (sum- and difference-frequency generation)

- Cubic nonlinear interactions (triple sum-frequency generation, self-phase modulation, conjugated Kerr term)

- Raman scattering

- Self-steepening

- Frequency-dependence of the nonlinear coefficients

- z-dependence of the effective refractive index and nonlinear coefficients (permitting e.g. poling and tapered waveguides to be simulated)

The package is built to be as user-friendly as possible, providing a relatively high-level interface while still allowing for physically intricate simulation

cases. It leverages a purposely-developped order 5 solver, although more classical solvers (such as the RK4IP) have also been implemented for completeness and versatility.

C.1.2 Installation

First, make sure pip is up-to-date using

```
pip install --upgrade pip
```

On Windows, install the package using

```
pip install pychi
```

On Mac, one might have to first run

```
conda install -c conda-forge pyfftw
```

due to some OS specificities in pyFFTW installation.
   Then, one should be able to install pychi normally using

```
pip install pychi
```

C.1.3 Documentation

The documentation is available and best viewed under ReadTheDocs (https://pychi.readthedocs.io/en/latest/). This documentation has been automatically generated using SPHINX, and is still a work in progress. Do not hesitate to contact us at pychi@desy.de for any needed clarifications and examples.

C.1.4 Example

Here is a typical example of the use of pychi to simulate the propagation of a short optical pulse in a nonlinear waveguide exhibiting both cubic and quadratic nonlinearities.

```
# -*- coding: utf-8 -*-
"""
Created on Mon Feb 28 15:31:47 2022
The waveguide/fiber parameters are first provided, and a Waveguide instance
is created. Then, the pulse parameters are used to create a Light object.
A physical model is then chosen, taking into account different nonlinear
interactions based on the user choice. Finally, a solver is instantiated
and computes the propagation of the pulse in the waveguide with the chosen
nonlinear interactions.
@author: voumardt
"""
import matplotlib.pyplot as plt
import numpy as np
```

```python
from scipy.constants import c

import pychi


"""
User parameters
"""
### Simulation
t_pts = 2**15

### Light
pulse_duration = 100e-15
pulse_wavelength = 1.56e-06
pulse_energy = 1e-9

### Waveguide
wg_length = 0.001
wg_chi_2 = 1.1e-12
wg_chi_3 = 3.4e-21
wg_a_eff = 1e-12
wg_freq, wg_n_eff = np.load('effective_index.npy')
# wg_n_eff is the effective dispersion of the waveguide considered,
# sampled on the grid wg_freq


"""
Nonlinear propagation
"""
### Prepare waveguide
waveguide = pychi.materials.Waveguide(wg_freq, wg_n_eff, wg_chi_2, wg_chi_3,
                                      wg_a_eff, wg_length, t_pts=t_pts)
# Additional options:
# wg_n_eff can be a 2 dimensional array, with first dimension
# the wavelength dependence and second dimension the z dependence.
#
# chi2 and chi3 can be callables, returning a z dependent value.
# Alternatively, they can be defined as one dimensional arrays
# describing their z dependence, or two dimensional arrays
# describing their z and frequency dependence. They can
# also be callables of (z, freq).
#
# One can use waveguide.set_gamma(gamma) or waveguide.set_n2(n2)
# to provide a nonlinear coefficient or nonlinear refractive
# index and overwrite chi3.
#
```

```
# Check documentation for more options and details.


### Prepare input pulse
pulse = pychi.light.Sech(waveguide, pulse_duration, pulse_energy,
                         pulse_wavelength)
# Other available pulse shapes:
# pulse = pychi.light.Gaussian(waveguide, pulse_duration,
                               pulse_energy, pulse_wavelength)
# pulse = pychi.light.Cw(waveguide, pulse_average_power, pulse_wavelength)
# pulse = pychi.light.Arbitrary(waveguide, pulse_frequency_axis,
                                pulse_electric_field, pulse_energy)


### Prepare model
model = pychi.models.SpmChi2Chi3(waveguide, pulse)
# Other models available:
# model = pychi.models.Spm(waveguide, pulse)
# model = pychi.models.Chi2(waveguide, pulse)
# model = pychi.models.Chi3(waveguide, pulse)
# model = pychi.models.SpmChi2(waveguide, pulse)
# model = pychi.models.SpmChi3(waveguide, pulse)
# model = pychi.models.Chi2Chi3(waveguide, pulse)


### Prepare solver, solve
solver = pychi.solvers.Solver(model)
solver.solve()


"""
Plots
"""
pulse.plot_propagation()
# Results can also be accessed via pulse.z_save, pulse.freq,
# pulse.spectrum, pulse.waveform
# The refractive index and GVD can be seen
# with waveguide.plot_refractive_index()
```

Typical propagation results using the above script would look as in Fig. C.1.4.

Check the examples folder for some specific cases and validation against experimental data.

Propagation results
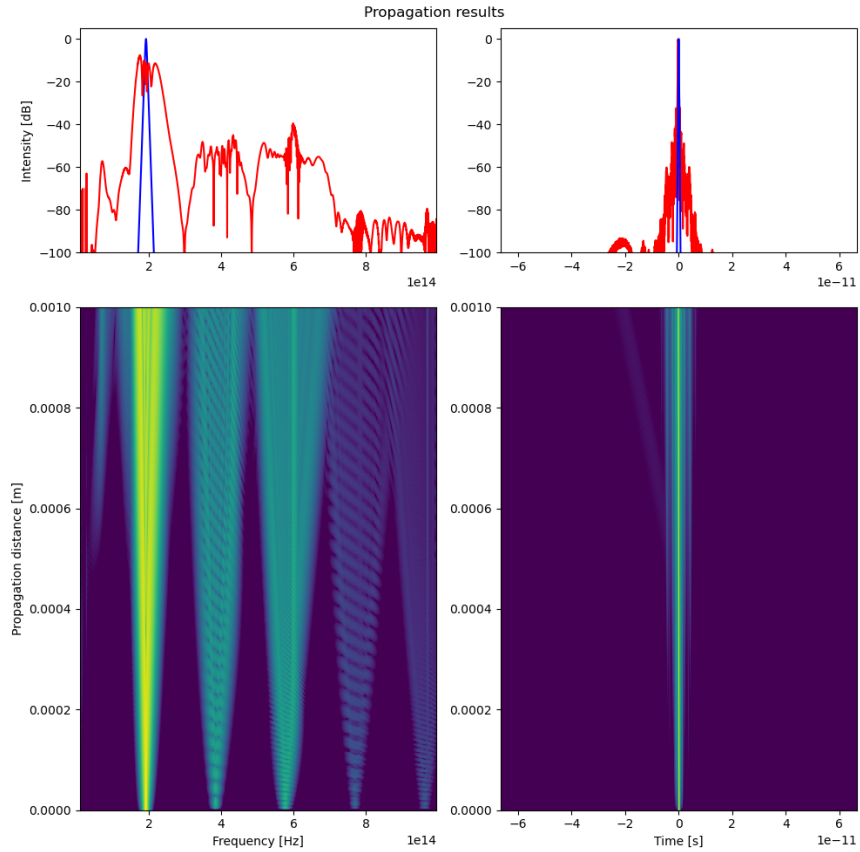
C.1.5 Contacts

pychi has been developped at DESY by the Ultrafast Microphotonics group. If you use it for publications, please cite the associated paper with DOI 10.1063/5.0135252.

If you have any questions, remarks, contributions, do not hesitate to contact us at pychi@desy.de or directly on GitHub (https://github.com/pychi-code/pychi).

C.2 Theory

In this section, the propagation equation that is implemented in the simulation software pyChi is derived from Maxwell's equations. The different approximations used are highlighted in bold, permitting a better understanding of the equation's limitations. Similar approaches are used to derive the standard nonlinear Schrödinger equation and its generalizations, which come as special cases arising from bandwidth-limiting approximations. Notably, the complete deriva-

tion is a hard to find resource, motivating its inclusion here. Useful resources for this derivation can be found in References [192, 206, 210, 211, 212, 213, 214, 215, 216, 217, 218, 219, 220, 221].

C.2.1 Definitions

We use the following convention for Fourier transformations:

$$F(t) = \frac{1}{2\pi} \int_{-\infty}^{\infty} f(\omega) e^{i\omega t} d\omega, \tag{C.1}$$

$$f(\omega) = \int_{-\infty}^{\infty} F(t) e^{-i\omega t} dt. \tag{C.2}$$

Notably, time-domain quantities are denoted with an upper case letter, while the corresponding frequency-domain quantities are denoted with a lower case letter.

C.2.2 Maxwell's equations

Let us start from Maxwell's macroscopic equations

$$\vec{\nabla} \cdot \vec{D} = \rho_f, \tag{C.3}$$

$$\vec{\nabla} \cdot \vec{B} = 0, \tag{C.4}$$

$$\vec{\nabla} \wedge \vec{E} = -\frac{\partial \vec{B}}{\partial t}, \tag{C.5}$$

$$\vec{\nabla} \wedge \vec{H} = \vec{J}_f + \frac{\partial \vec{D}}{\partial t}, \tag{C.6}$$

where $\vec{D}$ is the displacement field, ρ_f is the free charge density, $\vec{B}$ is the magnetic field, $\vec{E}$ is the electric field, $\vec{H}$ is the magnetising field and $\vec{J}_f$ is the free electric current density. The displacement field is defined as

$$\vec{D} = \epsilon_0 \vec{E} + \vec{P}, \tag{C.7}$$

where ϵ_0 is the vacuum permittivity and $\vec{P}$ is the polarisation, whose expression depends on the constitutive equations of the material at hand. Similarly, the magnetising field is defined as

$$\vec{H} = \frac{1}{\mu_0} \vec{B} - \vec{M}, \tag{C.8}$$

where μ_0 is the vacuum magnetic permeability and $\vec{M}$ is the magnetisation, whose expression also depends on the constitutive equations of the media of propagation. Maxwell's equations can then be rewritten as

$$\epsilon_0 \vec{\nabla} \cdot \vec{E} + \vec{\nabla} \cdot \vec{P} = \rho_f, \tag{C.9}$$

$$\vec{\nabla} \cdot \vec{B} = 0, \tag{C.10}$$

$$\vec{\nabla} \wedge \vec{E} = -\frac{\partial \vec{B}}{\partial t}, \tag{C.11}$$

$$\frac{1}{\mu_0} \vec{\nabla} \wedge \vec{B} - \vec{\nabla} \wedge \vec{M} = \vec{J}_f + \epsilon_0 \frac{\partial \vec{E}}{\partial t} + \frac{\partial \vec{P}}{\partial t}. \tag{C.12}$$

Note that by taking the time derivative of Eq. C.9 and the divergence of Eq. C.12, one gets the continuity equation

$$\vec{\nabla} \cdot \vec{J}_f + \frac{\partial \rho_f}{\partial t} = 0. \tag{C.13}$$

Taking the curl of Eq. C.11 and the time derivative of Eq. C.12, one obtains

$$\vec{\nabla} \wedge (\vec{\nabla} \wedge \vec{E}) = -\vec{\nabla} \wedge \frac{\partial \vec{B}}{\partial t} \tag{C.14}$$

and

$$\frac{1}{\mu_0} \vec{\nabla} \wedge \frac{\partial \vec{B}}{\partial t} - \vec{\nabla} \wedge \frac{\partial \vec{M}}{\partial t} = \frac{\partial \vec{J}_f}{\partial t} + \epsilon_0 \frac{\partial^2 \vec{E}}{\partial t^2} + \frac{\partial^2 \vec{P}}{\partial t^2}, \tag{C.15}$$

which can be combined into

$$\epsilon_0 \frac{\partial^2 \vec{E}}{\partial t^2} + \frac{1}{\mu_0} \vec{\nabla} \wedge (\vec{\nabla} \wedge \vec{E}) = -\frac{\partial \vec{J}_f}{\partial t} - \frac{\partial^2 \vec{P}}{\partial t^2} - \vec{\nabla} \wedge \frac{\partial \vec{M}}{\partial t}. \tag{C.16}$$

Using the identity

$$\vec{\nabla} \wedge (\vec{\nabla} \wedge \vec{A}) = \vec{\nabla}(\vec{\nabla} \cdot \vec{A}) - \nabla^2 \vec{A} \tag{C.17}$$

where $\vec{A}$ is any vector field, the divergence of Eq. C.9

$$\vec{\nabla}(\vec{\nabla} \cdot \vec{E}) = \frac{1}{\epsilon_0} \vec{\nabla} \rho_f - \frac{1}{\epsilon_0} \vec{\nabla}(\vec{\nabla} \cdot \vec{P}) \tag{C.18}$$

and the identity

$$\epsilon_0 \mu_0 = c^{-2}, \tag{C.19}$$

one obtains the inhomogenous wave equation

$$\nabla^2 \vec{E} - \frac{1}{c^2} \frac{\partial^2 \vec{E}}{\partial t^2} = \frac{1}{\epsilon_0} \vec{\nabla} \rho_f + \mu_0 \frac{\partial \vec{J}_f}{\partial t} - \frac{1}{\epsilon_0} \vec{\nabla}(\vec{\nabla} \cdot \vec{P}) + \mu_0 \frac{\partial^2 \vec{P}}{\partial t^2} + \mu_0 \vec{\nabla} \wedge \frac{\partial \vec{M}}{\partial t}. \tag{C.20}$$

Taking the Fourier transform of Eq. C.20 yields

$$\left(\nabla^2 + \frac{\omega^2}{c^2}\right) \vec{e} = \frac{1}{\epsilon_0} \vec{\nabla} \rho_f + i\mu_0 \omega \vec{j}_f - \frac{1}{\epsilon_0} \vec{\nabla}(\vec{\nabla} \cdot \vec{p}) - \mu_0 \omega^2 \vec{p} + i\mu_0 \omega \vec{\nabla} \wedge \vec{m}. \tag{C.21}$$

C.2.3   Simplifications in waveguides

Now that we have derived the general equation C.21, let us apply it to the special case of a nonlinear waveguide, fiber or crystal pumped by an intense, short pulse. The waveguides of interest are considered neutral and not conductive, therefore there are **no free charges or currents**, i.e.

$$\rho_f = 0, \tag{C.22}$$

$$j_f = 0. \tag{C.23}$$

The waveguides are also typically **non-magnetic** with

$$\vec{m} = 0, \tag{C.24}$$

so that Eq. C.21 reduces to

$$\left(\nabla^2 + \frac{\omega^2}{c^2}\right)\vec{e} = -\frac{1}{\epsilon_0}\vec{\nabla}(\vec{\nabla}\cdot\vec{p}) - \mu_0\omega^2\vec{p}. \tag{C.25}$$

The polarisation field can be estimated through the use of quantum mechanics, but **far from material resonances**

$$\vec{P}(t) = \epsilon_0 \sum_{n=1}^{\infty} \int_{-\infty}^{\infty} \int_{-\infty}^{\infty} ...\, dt'dt''...\, X^{(n)}(t-t', t-t'', ...) : E(t')E(t'')..., \tag{C.26}$$

where $X^{(n)}$ is a rank $n+1$ tensor and : denotes the tensor product. Causality implies $X^{(n)} = 0$ for $t - t^{(n)} > 0$, and we have considered here only **local interactions**, i.e. there is no integration in the spatial dimensions. Note that a constant term is not excluded, but only relevant in ferroelectric materials. One can write the Fourier transform of $\vec{P}(t)$ as

$$\vec{p}(\omega) = \epsilon_0 \sum_{n=1}^{\infty} (2\pi)^{1-n} \vec{p}_n(\omega), \tag{C.27}$$

where

$$\vec{p}_n(\omega) = \int_{-\infty}^{\infty} \int_{-\infty}^{\infty} ...d\omega' d\omega''... \chi^{(n)}(\omega', \omega'', ...)$$
$$: e(\omega')e(\omega'')...\delta(\omega' + \omega'' + ... - \omega), \tag{C.28}$$

where $\delta(\omega)$ is the Dirac delta function and

$$\chi^{(n)}(\omega', \omega'', ...) = \int_{-\infty}^{\infty} \int_{-\infty}^{\infty} ...dt' dt''...X^{(n)}(t', t'', ...)e^{-i(\omega't'+\omega''t''+...)} \tag{C.29}$$

is the Fourier transform of the nonlinear response tensor. These tensors usually have drastically reduced norm with n, so we suppose that the waveguides considered exhibit **only χ^2 and χ^3 nonlinearities**. This is usually a reasonable

approximation as the model still accurately captures waveguides that have a negligible $X^{(2)}$ due to symmetry (centro-symmetric material have $X^{(2)} \approx 0$). Notably, the approach can be straightforwardly extended to higher nonlinearity orders. We consequently set

$$\vec{p}(\omega) = \epsilon_0 \sum_{n=1}^{3} (2\pi)^{1-n} \vec{p}_n(\omega). \tag{C.30}$$

As the linear term in the polarisation is big compared to the next order terms, one has from Eq. C.9 by supposing **small nonlinear effects** and **low spatial dependency of the linear response tensor**

$$
\begin{aligned}
0 &= \vec{\nabla} \cdot \vec{d} \\
&= \epsilon_0 \vec{\nabla} \cdot \vec{e} + \vec{\nabla} \cdot \vec{p} \\
&= \epsilon_0 \vec{\nabla} \cdot \vec{e} + \epsilon_0 \vec{\nabla} \cdot (\chi^{(1)} : \vec{e} + \sum_{n=2}^{3} (2\pi)^{1-n} \vec{p}_n(\omega)) \\
&\approx \epsilon_0 \vec{\nabla} \cdot \vec{e} + \epsilon_0 \vec{\nabla} \cdot (\chi^{(1)} : \vec{e}) \\
&\approx \epsilon_0 (1 + \chi^{(1)}) \vec{\nabla} \cdot \vec{e} \\
&\implies \vec{\nabla} \cdot \vec{e} \approx 0 \\
&\implies \vec{\nabla} \cdot \vec{p} \approx 0,
\end{aligned}
\tag{C.31}
$$

and therefore Eq. C.20 becomes

$$\left(\nabla^2 + \epsilon_0 \mu_0 \omega^2\right) \vec{e} = -\mu_0 \omega^2 \vec{p}. \tag{C.32}$$

The terms linear in $\vec{e}$ in $\vec{p}$ can be accounted for by defining

$$\epsilon_0 \longrightarrow \epsilon(\omega) = \epsilon_0 (1 + \chi^{(1)}(\omega)), \tag{C.33}$$

$$\vec{p} \longrightarrow \vec{p}_{NL}, \tag{C.34}$$

where $\vec{p}_{NL}$ contains only the nonlinear terms, giving

$$\left(\nabla^2 + \epsilon \mu_0 \omega^2\right) \vec{e} = -\mu_0 \omega^2 \vec{p}_{NL}. \tag{C.35}$$

The refractive index is then defined as

$$n = \sqrt{\frac{\epsilon(\omega)}{\epsilon_0}} = \sqrt{1 + \chi^{(1)}}. \tag{C.36}$$

Supposing that the susceptibility is **homogeneous and isotropic** and choosing the axis orientation properly (here along the z-axis), one obtains the scalar nonlinear wave equation

$$\left(\nabla^2 + \epsilon \mu_0 \omega^2\right) e = -\mu_0 \omega^2 p_{NL} \tag{C.37}$$

or in the time domain,

$$(\nabla^2 - \epsilon\mu_0\partial_t^2)E = \mu_0\partial_t^2 P_{NL}. \tag{C.38}$$

Eq. C.38 is usually the starting point for nonlinear simulations in most kind of materials, comprising waveguides, nonlinear fibers and crystals.

C.2.4   Effective refractive index

To proceed further, we note that

$$\nabla^2 = \partial_x^2 + \partial_y^2 + \partial_z^2, \tag{C.39}$$

define

$$k^2 = \epsilon\mu_0\omega^2 \tag{C.40}$$

and postulate that the following variable separation is sensible:

$$e(x, y, z, \omega) = g(x, y, \omega)a(z, \omega), \tag{C.41}$$

which leads to

$$(\partial_x^2 g + \partial_y^2 g)a + g\partial_z^2 a + k^2 ga = -\mu_0\omega^2 p_{NL}. \tag{C.42}$$

By dividing by ga, one gets

$$\frac{1}{g}(\partial_x^2 g + \partial_y^2 g) + \frac{1}{a}\partial_z^2 a + k^2 = -\frac{\mu_0\omega^2}{ga}p_{NL}. \tag{C.43}$$

Note that the first term depends spatially only on x and y, the second term depends only on z, the third term is a constant and the RHS is a mixed term. The equation can thus be split into two parts

$$\frac{1}{g}(\partial_x^2 + \partial_y^2)g + (k^2 - \beta^2(z)) = -\frac{\mu_0\omega^2}{ga}p_{NL}, \tag{C.44}$$

$$\frac{1}{a}\partial_z^2 a = -\beta^2(z), \tag{C.45}$$

where the effective wavevector $\beta(z)$ needs to be determined from the first equation, and the second dictates the field propagation in the z direction.

   The solution to the first equation is approximated using perturbation theory. Supposing that the **nonlinear terms are small**, we write

$$g = g_0 + g_1 + ..., \tag{C.46}$$

where the subscripts denote the order of the perturbation, and where both $\chi^{(2)}$ and $\chi^{(3)}$ are considered first order perturbations. We also define

$$\beta^2 = \beta_0^2 + \beta_1^2 + ... \tag{C.47}$$

118

At order zero, one has

$$(\partial_x^2 + \partial_y^2)g_0 + (k^2 - \beta_0^2(z))g_0 = 0. \tag{C.48}$$

It is clear that this equation is independent of z, so that $\beta_0(z) = \beta_0$. This equation admits solutions in the form of spatial modes, which can be computed knowing the exact geometry of the waveguide, fiber or crystal used. Typically, we suppose that the laser light used to pump the sample has a single mode of lowest order, which means that only the lowest order "TM" (transverse magnetic) and "TE" (transverse electric) modes need to be computed. This is typically achieved using finite element methods software such as COMSOL, by requiring finiteness of the electric and magnetic field and appropriate continuity equations at interfaces. We thus assume from now on that β_0 is a known quantity.

At order one, we have

$$(\partial_x^2 + \partial_y^2)(g_0 + g_1) + (k^2 - \beta_0^2 - \beta_1^2(z))(g_0 + g_1) = -\frac{\mu_0\omega^2}{a(\omega, z)}p_{NL}^{(1)}, \tag{C.49}$$

where

$$p_{NL}^{(1)} = \frac{\epsilon_0}{2\pi}\int_{-\infty}^{\infty}d\omega'\chi^{(2)}(\omega', \omega-\omega')a(\omega', z)a(\omega-\omega', z)g_0(x, y, \omega')g_0(x, y, \omega-\omega')$$

$$+ \frac{\epsilon_0}{4\pi^2}\int_{-\infty}^{\infty}\int_{-\infty}^{\infty}d\omega'd\omega''\chi^{(3)}(\omega', \omega'', \omega-\omega'-\omega'')a(\omega', z)a(\omega'', z)a(\omega-\omega'-\omega'')$$

$$\cdot g_0(x, y, \omega')g_0(x, y, \omega'')g_0(x, y, \omega-\omega'-\omega''). \tag{C.50}$$

Using the order zero solution, one gets

$$-\beta_1^2 g_0 + (\partial_x^2 + \partial_y^2)g_1 + (k^2 - \beta_0^2)g_1 = -\frac{\mu_0\omega^2}{a}p_{NL}^{(1)}. \tag{C.51}$$

Multiplying by g on both sides, one gets

$$-\beta_1^2 g_0^2 + g_0(\partial_x^2 + \partial_y^2)g_1 + g_0(k^2 - \beta_0^2)g_1 = -\frac{\mu_0\omega^2}{a}g_0 p_{NL}^{(1)}. \tag{C.52}$$

By integrating over the whole x-y domain, one gets

$$\int dxdy\ \left[-\beta_1^2 g_0^2 + g_0(\partial_x^2 + \partial_y^2)g_1 + g_0(k^2 - \beta_0^2)g_1\right]$$

$$= -\int dxdy\ \frac{\mu_0\omega^2}{a}g_0 p_{NL}^{(1)}. \tag{C.53}$$

The second term on the left-hand side can be integrated by parts twice in x and y, which upon **vanishing of the field at infinity (or domain boundary)** yields

$$\int dxdy\ \left[-\beta_1^2 g_0^2 + g_1(\partial_x^2 + \partial_y^2)g_0 + g_0(k^2 - \beta_0^2)g_1\right]$$

$$= -\int dxdy\ \frac{\mu_0\omega^2}{a}g_0 p_{NL}^{(1)}. \tag{C.54}$$

119

The equation of motion for the g_0 field can now be used to finally provide

$$\beta_1^2 \int dx dy \ g_0^2 = \int dx dy \ \frac{\mu_0 \omega^2}{a} g_0 p_{NL}^{(1)}.$$ (C.55)

Note that the exact solution for g_1 does not need to be known to obtain this first order correction. We truncate the series at this point, although it could in principle be computed up to any order. Consequently, inserting β in Eq. C.45 leads to the propagation equation

$$\partial_z^2 a + \beta_0^2 a = -\mu_0 \omega^2 \frac{\int dx dy \ g_0 p_{NL}^{(1)}}{\int dx dy \ g_0^2}.$$ (C.56)

Note that the parameter β_0^2 is identified as the effective wavevector, which we will denote simply as β from now on. Note that one can define an effective refractive index as

$$\beta(\omega) \equiv \beta_0(\omega) = \frac{n_{eff}(\omega)\omega}{c}.$$ (C.57)

This effective refractive index comprises both material dispersion and the dispersion due to the geometry of the propagation medium.

C.2.5 Integrating out the spatial dependence

The integral in the numerator of the right hand side of Eq. C.55 can be written explicitly as follows:

$$\frac{\epsilon_0}{2\pi} \int_{-\infty}^{\infty} d\omega' \chi^{(2)}(\omega', \omega - \omega') a(\omega') a(\omega - \omega') \int dx dy \ g_0(\omega) g_0(\omega') g_0(\omega - \omega')$$

$$+ \frac{\epsilon_0}{4\pi^2} \int_{-\infty}^{\infty} \int_{-\infty}^{\infty} d\omega' d\omega'' \chi^{(3)}(\omega', \omega'', \omega - \omega' - \omega'') a(\omega') a(\omega'') a(\omega - \omega' - \omega'')$$

$$\cdot \int dx dy \ g_0(\omega) g_0(\omega') g_0(\omega'') g_0(\omega - \omega' - \omega'').$$ (C.58)

These integrals could be computed using the numerical solution g_0 to the eigenvalue problem. The spatial dependence can then be taken care of by redefining

$$\overline{\chi}^{(3)} = \chi^{(3)} \frac{\int dx dy \ g_0(\omega) g_0(\omega') g_0(\omega'') g_0(\omega - \omega' - \omega'')}{\int dx dy \ g_0^2(\omega)}$$ (C.59)

and

$$\overline{\chi}^{(2)} = \chi^{(2)} \frac{\int dx dy \ g_0(\omega) g_0(\omega') g_0(\omega - \omega')}{\int dx dy \ g_0^2(\omega)}$$ (C.60)

Here, we propose to **approximate g_0 with a Gaussian profile**. Let us also suppose that g_0 **is independent of ω** and

$$g_0(x, y, \omega) = G e^{\frac{-x^2 - y^2}{R^2}}.$$ (C.61)

Then, one gets

$$\int dxdy \, g_0^2 = G^2 \pi R^2 / 2 \tag{C.62}$$

$$\int dxdy \, g_0^3 = G^3 \pi R^2 / 3 \tag{C.63}$$

and

$$\int dxdy \, g_0^4 = G^4 \pi R^2 / 4. \tag{C.64}$$

Note now that the χ^3 term's spatial dependence can be written as

$$\int dxdy \, g_0^2 \cdot \frac{\int dxdy \, g_0^4}{(\int dxdy \, g_0^2)^2}, \tag{C.65}$$

where

$$\frac{(\int dxdy \, g_0^2)^2}{\int dxdy \, g_0^4} \tag{C.66}$$

can be recognised as the standard definition of the effective area A_{eff}. As we have some freedom in the definition of g_0 (the constant G), we require that

$$\int dxdy \, g_0^2 = A_{eff} = \frac{(\int dxdy \, g_0^2)^2}{\int dxdy \, g_0^4}, \tag{C.67}$$

so that the power in the waveguide is given by

$$P = \frac{1}{2} \epsilon_0 c n_{eff} A_{eff} |a|^2. \tag{C.68}$$

With this normalisation, the spatial dependence drops out of the χ^3 term completely and is swallowed in the definition of the electric field in terms of the power, which means that $\overline{\chi}^{(3)} = \chi^{(3)}$. This also leads to

$$G = \sqrt{2}, \tag{C.69}$$

which when inserted in the χ^2 spatially dependent integrals provides

$$\frac{\int dxdy \, g_0^3}{\int dxdy \, g_0^2} = \frac{2\sqrt{2}}{3} \approx 0.942. \tag{C.70}$$

One can then redefine

$$\overline{\chi_2} = \frac{2\sqrt{2}}{3} \chi_2. \tag{C.71}$$

Dropping the bar notation for the nonlinear indices, one obtains

$$\partial_z^2 a + \beta_0^2 a = -\mu_0 \omega^2 \overline{p}_{NL}, \tag{C.72}$$

121

with

$$\overline{p}_{NL} = \frac{\epsilon_0}{2\pi} \int_{-\infty}^{\infty} d\omega' \chi^{(2)}(\omega', \omega - \omega') a(\omega', z) a(\omega - \omega', z)$$
$$+ \frac{\epsilon_0}{4\pi^2} \int_{-\infty}^{\infty} \int_{-\infty}^{\infty} d\omega' d\omega'' \chi^{(3)}(\omega', \omega'', \omega - \omega' - \omega'') a(\omega', z) a(\omega'', z) a(\omega - \omega' - \omega'').$$

$$(\text{C.73})$$

Eq. C.72 has exactly the same form as Eq. C.38, except that the x, y dependencies have been taken care of, χ^2 has been multiplied by $\frac{2\sqrt{2}}{3}$, and the refractive index now comprises geometrical dispersion. Note that we drop the bar over the nonlinear polarization in the following.

C.2.6   Analytical signal

Taking advantage of the hermitian nature of the electric field, one can define

$$a(\omega) = (\alpha(\omega) + \alpha^\dagger(-\omega))/2, \qquad (\text{C.74})$$

where

$$\alpha(\omega > 0) = 2a(\omega), \qquad (\text{C.75})$$
$$\alpha(\omega = 0) = a(\omega), \qquad (\text{C.76})$$
$$\alpha(\omega < 0) = 0. \qquad (\text{C.77})$$

This corresponds to assigning a field containing all the information in the positive frequency axis, rather than using a hermitian field covering both the negative and positive frequency axis. Notably, $\alpha(\omega)$ is the Fourier transform of the analytical signal associated to $E(t)$, which can be computed using the Hilbert transform. Note that the dependence of the nonlinear parameters on frequencies will be omitted from now on, but can be restored if necessary.

Inserting $a(\omega)$ in Eq. C.72 provides

$$(\partial_z^2 + \beta^2)(\alpha(\omega) + \alpha^\dagger(-\omega)) =$$
$$-\frac{\mu_0 \epsilon_0 \omega^2}{4\pi} \int_{-\infty}^{\infty} d\omega' \chi^{(2)} \Big[\alpha(\omega')\alpha(\omega - \omega') + \alpha(\omega')\alpha^\dagger(\omega' - \omega)$$
$$+ \alpha^\dagger(-\omega')\alpha(\omega - \omega') + \alpha^\dagger(-\omega')\alpha^\dagger(\omega' - \omega) \Big]$$
$$-\frac{\mu_0 \epsilon_0 \omega^2}{16\pi^2} \int_{-\infty}^{\infty} d\omega' d\omega'' \chi^{(3)} \Big[\alpha(\omega')\alpha(\omega'')\alpha(\omega - \omega' - \omega'')$$
$$+ \alpha^\dagger(-\omega')\alpha(\omega'')\alpha(\omega - \omega' - \omega'') + \alpha(\omega')\alpha^\dagger(-\omega'')\alpha(\omega - \omega' - \omega'')$$
$$+ \alpha(\omega')\alpha(\omega'')\alpha^\dagger(\omega' + \omega'' - \omega) + \alpha^\dagger(-\omega')\alpha^\dagger(-\omega'')\alpha(\omega - \omega' - \omega'')$$
$$+ \alpha^\dagger(-\omega')\alpha(\omega'')\alpha^\dagger(\omega' + \omega'' - \omega) + \alpha(\omega')\alpha^\dagger(-\omega'')\alpha^\dagger(\omega' + \omega'' - \omega)$$
$$+ \alpha^\dagger(-\omega')\alpha^\dagger(-\omega'')\alpha^\dagger(\omega' + \omega'' - \omega) \Big]. \quad (\text{C.78})$$

As $\alpha(\omega)$ has a support from 0 to ∞, one has for $\omega \geq 0$

$$(\partial_z^2 + \beta^2)\alpha(\omega) =$$
$$- \frac{\mu_0 \epsilon_0 \omega^2}{4\pi} \int_{-\infty}^{\infty} d\omega' \chi^{(2)} \Big[\alpha(\omega')\alpha(\omega - \omega') + \alpha(\omega')\alpha^\dagger(\omega' - \omega)$$
$$+ \alpha^\dagger(-\omega')\alpha(\omega - \omega') \Big]$$
$$- \frac{\mu_0 \epsilon_0 \omega^2}{16\pi^2} \int_{-\infty}^{\infty} d\omega' d\omega'' \chi^{(3)} \Big[\alpha(\omega')\alpha(\omega'')\alpha(\omega - \omega' - \omega'')$$
$$+ \alpha^\dagger(-\omega')\alpha(\omega'')\alpha(\omega - \omega' - \omega'') + \alpha(\omega')\alpha^\dagger(-\omega'')\alpha(\omega - \omega' - \omega'')$$
$$+ \alpha(\omega')\alpha(\omega'')\alpha^\dagger(\omega' + \omega'' - \omega) + \alpha^\dagger(-\omega')\alpha^\dagger(-\omega'')\alpha(\omega - \omega' - \omega'')$$
$$+ \alpha^\dagger(-\omega')\alpha(\omega'')\alpha^\dagger(\omega' + \omega'' - \omega) + \alpha(\omega')\alpha^\dagger(-\omega'')\alpha^\dagger(\omega' + \omega'' - \omega) \Big]. \quad \text{(C.79)}$$

Note that the negative frequency equation is redundant with this one. The integrals can then be reduced from $[-\infty, \infty]$ to $[0, \infty]$ by appropriate change of variables. For the quadratic nonlinearity, one gets

$$p_{NL}^{(2)} = \frac{\chi^{(2)}}{4\pi\mu_0 c^2} \int_0^\infty d\omega' \alpha(\omega')\alpha(\omega - \omega') + 2\alpha^\dagger(\omega' - \omega)\alpha(\omega'). \quad \text{(C.80)}$$

One can recognize here the term responsible for sum-frequency generation respectively the term driving difference-frequency generation. Similarly, for the cubic nonlinearity,

$$p_{NL}^{(3)} = \frac{\chi^{(3)}}{16\pi\mu_0 c^2} \int_0^\infty d\omega' \int_0^\infty d\omega'' \alpha(\omega')\alpha(\omega'')\alpha(\omega - \omega' - \omega'')$$
$$+ 3\alpha^\dagger(\omega' + \omega'' - \omega)\alpha(\omega')\alpha(\omega'') + 3\alpha(\omega + \omega' + \omega'')\alpha^\dagger(\omega')\alpha^\dagger(\omega''), \quad \text{(C.81)}$$

which shows the terms driving triple-sum frequency generation, self-phase modulation respectively the conjugated Kerr term (analogous to the difference-frequency generation in a quadratic material).

C.2.7 Propagation equation

To proceed to a model that can be numerically simulated from a given input pulse as the initial condition, a reduction in the degree of the differential equation is needed. There are different ways to proceed, the most common one being the so-called slowly varying envelope approximation. We follow here another method based on an operator point of view, which clarifies the required approximations, although yields the same final result. We start by defining the nonlinear operator Π via

$$(\partial_z^2 + \beta^2)\alpha = -\mu_0 \omega^2 p_{NL} := \Pi[\alpha]. \quad \text{(C.82)}$$

One then has

$$\left(\partial_z^2 + (\beta^2 - \Pi)\right)[\alpha] = 0, \quad \text{(C.83)}$$

123

which **if the nonlinear operator is small** can be formally simplified to

$$\left(\partial_z + i\sqrt{\beta^2 - \Pi}\right)\left(\partial_z - i\sqrt{\beta^2 - \Pi}\right)[\alpha] = 0. \tag{C.84}$$

This equation defines a forward- and a backward-propagation wave. **If their interaction is neglected**, they can be separated, and the forward propagating wave is described by

$$\left(\partial_z + i\sqrt{\beta^2 - \Pi}\right)[\alpha] = 0. \tag{C.85}$$

As the nonlinear interactions are small, the square root can then be Taylor expanded at first order to yield the final propagation equation

$$\partial_z \alpha + i\beta\alpha = \frac{i\Pi}{2\beta}[\alpha] = \frac{-i\mu_0\omega^2}{2\beta}p_{NL}, \tag{C.86}$$

where p_{NL} is given by Eq. C.80 and Eq. C.81. This equation can be numerically integrated and is the master equation that governs propagation in the pyChi simulation software.

Bibliography

[1] NIKOLAI V. Tkachenko. Chapter 1 - Introduction. In NIKOLAI V. Tkachenko, editor, *Optical Spectroscopy*, pages 1–14. Elsevier Science, Amsterdam, January 2006.

[2] William W. Parson. Introduction. In William W. Parson, editor, *Modern Optical Spectroscopy: With Exercises and Examples from Biophysics and Biochemistry*, pages 1–29. Springer, Berlin, Heidelberg, 2015.

[3] Margherita Maiuri, Marco Garavelli, and Giulio Cerullo. Ultrafast Spectroscopy: State of the Art and Open Challenges. *Journal of the American Chemical Society*, 142(1):3–15, January 2020.

[4] John L. Hall. Nobel Lecture: Defining and measuring optical frequencies. *Reviews of Modern Physics*, 78(4):1279–1295, November 2006.

[5] Theodor W. Hänsch. Nobel Lecture: Passion for precision. *Reviews of Modern Physics*, 78(4):1297–1309, November 2006.

[6] Th Udem, R. Holzwarth, and T. W. Hänsch. Optical frequency metrology. *Nature*, 416(6877):233–237, March 2002.

[7] Tara Fortier and Esther Baumann. 20 years of developments in optical frequency comb technology and applications. *Communications Physics*, 2(1):1–16, December 2019.

[8] Steven T. Cundiff. *Colloquium*: Femtosecond optical frequency combs. *Reviews of Modern Physics*, 75(1):325–342, 2003.

[9] Albert Schliesser, Nathalie Picqué, and Theodor W. Hänsch. Mid-infrared frequency combs. *Nature Photonics*, 6(7):440–449, July 2012.

[10] Ian Coddington, Nathan Newbury, and William Swann. Dual-comb spectroscopy. *Optica*, 3(4):414–426, April 2016.

[11] Nathalie Picqué and Theodor W. Hänsch. Frequency comb spectroscopy. *Nature Photonics*, 13(3):146–157, March 2019.

[12] S. Schiller. Spectrometry with frequency combs. *Optics Letters*, 27(9):766–768, May 2002.

[13] Fritz Keilmann, Christoph Gohle, and Ronald Holzwarth. Time-domain mid-infrared frequency-comb spectrometer. *Optics Letters*, 29(13):1542–1544, July 2004.

[14] Michel Mayor and Didier Queloz. A Jupiter-mass companion to a solar-type star. *Nature*, 378(6555):355–359, November 1995.

[15] Amanda M. Lines, Gabriel B. Hall, Susan Asmussen, Jarrod Allred, Sergey Sinkov, Forrest Heller, Neal Gallagher, Gregg J. Lumetta, and Samuel A. Bryan. Sensor Fusion: Comprehensive Real-Time, On-Line Monitoring for Process Control via Visible, Near-Infrared, and Raman Spectroscopy. *ACS Sensors*, 5(8):2467–2475, August 2020.

[16] Jang Ah Kim, Dominic J. Wales, and Guang-Zhong Yang. Optical spectroscopy for in vivo medical diagnosis—a review of the state of the art and future perspectives. *Progress in Biomedical Engineering*, 2(4):042001, August 2020.

[17] T. Südmeyer, S. V. Marchese, S. Hashimoto, C. R. E. Baer, G. Gingras, B. Witzel, and U. Keller. Femtosecond laser oscillators for high-field science. *Nature Photonics*, 2(10):599–604, October 2008.

[18] Alexandre Parriaux, Kamal Hammani, and Guy Millot. Electro-optic frequency combs. *Advances in Optics and Photonics*, 12(1):223–287, March 2020. Publisher: Optical Society of America.

[19] T. Herr, V. Brasch, J. D. Jost, C. Y. Wang, N. M. Kondratiev, M. L. Gorodetsky, and T. J. Kippenberg. Temporal solitons in optical microresonators. *Nature Photonics*, 8(2):145–152, February 2014.

[20] Takasumi Tanabe, Shun Fujii, and Ryo Suzuki. Review on microresonator frequency combs. *Japanese Journal of Applied Physics*, 58(SJ):SJ0801, July 2019.

[21] H.R. Telle, G. Steinmeyer, A.E. Dunlop, J. Stenger, D.H. Sutter, and U. Keller. Carrier-envelope offset phase control: A novel concept for absolute optical frequency measurement and ultrashort pulse generation. *Applied Physics B*, 69(4):327–332, October 1999.

[22] David J. Jones, Scott A. Diddams, Jinendra K. Ranka, Andrew Stentz, Robert S. Windeler, John L. Hall, and Steven T. Cundiff. Carrier-Envelope Phase Control of Femtosecond Mode-Locked Lasers and Direct Optical Frequency Synthesis. *Science*, 288(5466):635–639, April 2000.

[23] Andrew D. Ludlow, Martin M. Boyd, Jun Ye, E. Peik, and P. O. Schmidt. Optical atomic clocks. *Reviews of Modern Physics*, 87(2):637–701, June 2015.

[24] J. Pupeikis, B. Willenberg, S. L. Camenzind, A. Benayad, P. Camy, C. R. Phillips, and U. Keller. Spatially multiplexed single-cavity dual-comb laser. *Optica*, 9(7):713–716, July 2022.

[25] Abijith S. Kowligy, Henry Timmers, Alexander J. Lind, Ugaitz Elu, Flavio C. Cruz, Peter G. Schunemann, Jens Biegert, and Scott A. Diddams. Infrared electric field sampled frequency comb spectroscopy. *Science Advances*, 5(6):eaaw8794, June 2019.

[26] Nazanin Hoghooghi, Sida Xing, Peter Chang, Daniel Lesko, Alexander Lind, Greg Rieker, and Scott Diddams. 1-GHz mid-infrared frequency comb spanning 3 to 13 {\mu}m, January 2022.

[27] Birgitta Bernhardt, Lukas Fürst, Adrian Kirchner, Alexander Eber, Florian Siegrist, and Robert di Vora. Broadband near-ultraviolet dual comb spectroscopy, May 2023.

[28] Takuro Ideguchi, Antonin Poisson, Guy Guelachvili, Nathalie Picqué, and Theodor W. Hänsch. Adaptive real-time dual-comb spectroscopy. *Nature Communications*, 5(1):1–8, February 2014. Number: 1 Publisher: Nature Publishing Group.

[29] T. Ideguchi, B. Bernhardt, G. Guelachvili, T. W. Hänsch, and N. Picqué. Raman-induced Kerr-effect dual-comb spectroscopy. *Optics Letters*, 37(21):4498–4500, November 2012.

[30] Arthur Hipke. *Dual-frequency-comb two-photon spectroscopy.* Text.PhDThesis, Ludwig-Maximilians-Universität München, April 2016.

[31] Sho Okubo, Kana Iwakuni, Hajime Inaba, Kazumoto Hosaka, Atsushi Onae, Hiroyuki Sasada, and Feng-Lei Hong. Ultra-broadband dual-comb spectroscopy across 1.0–1.9 um. *Applied Physics Express*, 8(8):082402, July 2015. Publisher: IOP Publishing.

[32] G. B. Rieker, F. R. Giorgetta, W. C. Swann, I. Coddington, L. C. Sinclair, C. L. Cromer, E. Baumann, A. M. Zolot, and N. R. Newbury. Open-Path Dual-Comb Spectroscopy of Greenhouse Gases. In *CLEO: 2013 Postdeadline*, page CTh5C.9, San Jose, California, 2013. OSA.

[33] Hollie Wright, Jinghua Sun, David McKendrick, Nick Weston, and Derryck T. Reid. Two-photon dual-comb LiDAR. *Optics Express*, 29(23):37037–37047, November 2021.

[34] Nazanin Hoghooghi, Robert J. Wright, Amanda S. Makowiecki, William C. Swann, Eleanor M. Waxman, Ian Coddington, and Gregory B. Rieker. Broadband coherent cavity-enhanced dual-comb spectroscopy. *Optica*, 6(1):28–33, January 2019.

[35] D. Charczun, A. Nishiyama, G. Kowzan, A. Cygan, T. Voumard, T. Wildi, T. Herr, V. Brasch, D. Lisak, and P. Masłowski. Dual-comb cavity-mode width and shift spectroscopy. *Measurement*, 188:110519, January 2022.

[36] Daniel Lisak, Dominik Charczun, Akiko Nishiyama, Thibault Voumard, Thibault Wildi, Grzegorz Kowzan, Victor Brasch, Tobias Herr, Adam J. Fleisher, Joseph T. Hodges, Roman Ciuryło, Agata Cygan, and Piotr Masłowski. Dual-comb cavity ring-down spectroscopy. *Scientific Reports*, 12(1):2377, February 2022.

[37] David J. Benirschke, Ningren Han, and David Burghoff. Frequency comb ptychoscopy. *Nature Communications*, 12(1):4244, July 2021.

[38] Edoardo Vicentini, Zhenhai Wang, Kasper Van Gasse, Theodor W. Hänsch, and Nathalie Picqué. Dual-comb hyperspectral digital holography. *Nature Photonics*, 15(12):890–894, December 2021.

[39] Qiang Wang, Zhen Wang, Hui Zhang, Shoulin Jiang, Yingying Wang, Wei Jin, and Wei Ren. Dual-comb photothermal spectroscopy. *Nature Communications*, 13(1):2181, April 2022.

[40] Zebin Zhu and Guanhao Wu. Dual-Comb Ranging. *Engineering*, 4(6):772–778, December 2018.

[41] Haowei Shi, Zaijun Chen, Scott E. Fraser, Mengjie Yu, Zheshen Zhang, and Quntao Zhuang. Entanglement-enhanced dual-comb spectroscopy. *npj Quantum Information*, 9(1):91, September 2023.

[42] Muhammad A. Abbas, Qing Pan, Julien Mandon, Simona M. Cristescu, Frans J. M. Harren, and Amir Khodabakhsh. Time-resolved mid-infrared dual-comb spectroscopy. *Scientific Reports*, 9(1):17247, November 2019. Bandiera_abtest: a Cc_license_type: cc_by Cg_type: Nature Research Journals Number: 1 Primary_atype: Research Publisher: Nature Publishing Group Subject_term: Frequency combs;Infrared spectroscopy;Reaction kinetics and dynamics Subject_term_id: frequency-combs;infrared-spectroscopy;kinetics-and-dynamics.

[43] Nathan R. Newbury, Ian Coddington, and William Swann. Sensitivity of coherent dual-comb spectroscopy. *Optics Express*, 18(8):7929–7945, April 2010. Publisher: Optical Society of America.

[44] Guy Millot, Stéphane Pitois, Ming Yan, Tatevik Hovhannisyan, Abdelkrim Bendahmane, Theodor W. Hänsch, and Nathalie Picqué. Frequency-agile dual-comb spectroscopy. *Nature Photonics*, 10(1):27–30, January 2016. Number: 1 Publisher: Nature Publishing Group.

[45] M. T. Murphy, Th. Udem, R. Holzwarth, A. Sizmann, L. Pasquini, C. Araujo-Hauck, H. Dekker, S. D'Odorico, M. Fischer, T. W. Hänsch, and A. Manescau. High-precision wavelength calibration of astronomical

spectrographs with laser frequency combs. *Monthly Notices of the Royal Astronomical Society*, 380(2):839–847, August 2007.

[46] T. Wilken, C. Lovis, A. Manescau, T. Steinmetz, L. Pasquini, G. Lo Curto, T. W. Hänsch, R. Holzwarth, and Th. Udem. High-precision calibration of spectrographs. *Monthly Notices of the Royal Astronomical Society: Letters*, 405(1):L16–L20, June 2010.

[47] Tobias Wilken, Gaspare Lo Curto, Rafael A. Probst, Tilo Steinmetz, Antonio Manescau, Luca Pasquini, Jonay I. González Hernández, Rafael Rebolo, Theodor W. Hänsch, Thomas Udem, and Ronald Holzwarth. A spectrograph for exoplanet observations calibrated at the centimetre-per-second level. *Nature*, 485(7400):611–614, May 2012.

[48] Richard A. McCracken, Jake M. Charsley, and Derryck T. Reid. A decade of astrocombs: Recent advances in frequency combs for astronomy. *Optics Express*, 25(13):15058–15078, June 2017.

[49] Tobias Herr and Richard A. McCracken. Astrocombs: Recent Advances. *IEEE Photonics Technology Letters*, 31(23):1890–1893, December 2019.

[50] Dinko Milaković, Luca Pasquini, John K Webb, and Gaspare Lo Curto. Precision and consistency of astrocombs. *Monthly Notices of the Royal Astronomical Society*, 493(3):3997–4011, April 2020.

[51] François Wildi, Francesco Pepe, Bruno Chazelas, Gaspare Lo Curto, and Ch Lovis. A Fabry-Perot calibrator of the HARPS radial velocity spectrograph: Performance report. In *Ground-Based and Airborne Instrumentation for Astronomy III*, volume 7735, pages 1853–1863. SPIE, July 2010.

[52] C. Schwab, J. Stürmer, Y. V. Gurevich, T. Führer, S. K. Lamoreaux, T. Walther, and A. Quirrenbach. Stabilizing a Fabry–Perot Etalon Peak to 3 cm s-1 for Spectrograph Calibration. *Publications of the Astronomical Society of the Pacific*, 127(955):880, September 2015.

[53] Sebastian Schäfer and Ansgar Reiners. Two Fabry-Perot interferometers for high precision wavelength calibration in the near-infrared. In *Ground-Based and Airborne Instrumentation for Astronomy IV*, volume 8446, pages 1306–1313. SPIE, September 2012.

[54] A. Reiners, R. K. Banyal, and R. G. Ulbrich. A laser-lock concept to reach cm s-1-precision in Doppler experiments with Fabry-Pérot wavelength calibrators. *Astronomy & Astrophysics*, 569:A77, September 2014.

[55] F. F. Bauer, M. Zechmeister, and A. Reiners. Calibrating echelle spectrographs with Fabry-Pérot etalons. *Astronomy & Astrophysics*, 581:A117, September 2015.

[56] L. B. Kreuzer and C. K. N. Patel. Nitric Oxide Air Pollution: Detection by Optoacoustic Spectroscopy. *Science*, 173(3991):45–47, July 1971.

[57] A. Rosencwaig. Photoacoustic Spectroscopy of Biological Materials. *Science*, 181(4100):657–658, August 1973.

[58] C. K. N. Patel and A. C. Tam. Optoacoustic spectroscopy of liquids. *Applied Physics Letters*, 34(7):467–470, April 1979. Publisher: American Institute of Physics.

[59] Jingsong Li, Weidong Chen, and Benli Yu. Recent Progress on Infrared Photoacoustic Spectroscopy Techniques. *Applied Spectroscopy Reviews*, 46(6):440–471, August 2011.

[60] Johannes W. Cremer, Klemens M. Thaler, Christoph Haisch, and Ruth Signorell. Photoacoustics of single laser-trapped nanodroplets for the direct observation of nanofocusing in aerosol photokinetics. *Nature Communications*, 7(1):1–7, March 2016. Number: 1 Publisher: Nature Publishing Group.

[61] M. M. J. W. van Herpen, A. K. Y. Ngai, S. E. Bisson, J. H. P. Hackstein, E. J. Woltering, and F. J. M. Harren. Optical parametric oscillator-based photoacoustic detection of CO 2 at 4.23 um allows real-time monitoring of the respiration of small insects. *Applied Physics B*, 82(4):665–669, March 2006. Company: Springer Distributor: Springer Institution: Springer Label: Springer Number: 4 Publisher: Springer-Verlag.

[62] Xueding Wang, Yongjiang Pang, Geng Ku, Xueyi Xie, George Stoica, and Lihong V. Wang. Noninvasive laser-induced photoacoustic tomography for structural and functional in vivo imaging of the brain. *Nature Biotechnology*, 21(7):803–806, July 2003. Number: 7 Publisher: Nature Publishing Group.

[63] A. A. Kosterev, Yu A. Bakhirkin, R. F. Curl, and F. K. Tittel. Quartz-enhanced photoacoustic spectroscopy. *Optics Letters*, 27(21):1902–1904, November 2002. Publisher: Optical Society of America.

[64] Pietro Patimisco, Gaetano Scamarcio, Frank K. Tittel, and Vincenzo Spagnolo. Quartz-Enhanced Photoacoustic Spectroscopy: A Review. *Sensors*, 14(4):6165–6206, April 2014. Number: 4 Publisher: Multidisciplinary Digital Publishing Institute.

[65] Hongpeng Wu, Lei Dong, Huadan Zheng, Yajun Yu, Weiguang Ma, Lei Zhang, Wangbao Yin, Liantuan Xiao, Suotang Jia, and Frank K. Tittel. Beat frequency quartz-enhanced photoacoustic spectroscopy for fast and calibration-free continuous trace-gas monitoring. *Nature Communications*, 8(1):1–8, May 2017. Number: 1 Publisher: Nature Publishing Group.

[66] V. Koskinen, J. Fonsen, K. Roth, and J. Kauppinen. Cantilever enhanced photoacoustic detection of carbon dioxide using a tunable diode laser source. *Applied Physics B*, 86(3):451–454, February 2007. Company: Springer Distributor: Springer Institution: Springer Label: Springer Number: 3 Publisher: Springer-Verlag.

[67] Jari Peltola, Markku Vainio, Tuomas Hieta, Juho Uotila, Sauli Sinisalo, Markus Metsälä, Mikael Siltanen, and Lauri Halonen. High sensitivity trace gas detection by cantilever-enhanced photoacoustic spectroscopy using a mid-infrared continuous-wave optical parametric oscillator. *Optics Express*, 21(8):10240–10250, April 2013. Publisher: Optical Society of America.

[68] Vincenzo Spagnolo, Pietro Patimisco, Simone Borri, Gaetano Scamarcio, Bruce E. Bernacki, and Jason Kriesel. Part-per-trillion level SF_6 detection using a quartz enhanced photoacoustic spectroscopy-based sensor with single-mode fiber-coupled quantum cascade laser excitation. *Optics Letters*, 37(21):4461–4463, November 2012. Publisher: Optical Society of America.

[69] Teemu Tomberg, Markku Vainio, Tuomas Hieta, and Lauri Halonen. Sub-parts-per-trillion level sensitivity in trace gas detection by cantilever-enhanced photo-acoustic spectroscopy. *Scientific Reports*, 8(1):1848, December 2018.

[70] G Busse and B Bullemer. Use of the opto-acoustic effect for rapid scan Fourier spectroscopy. *Infrared Physics*, 18:631–634, 1978.

[71] Tommi Mikkonen, Caroline Amiot, Antti Aalto, Kim Patokoski, Goëry Genty, and Juha Toivonen. Broadband cantilever-enhanced photoacoustic spectroscopy in the mid-IR using a supercontinuum. *Optics Letters*, 43(20):5094–5097, October 2018. Publisher: Optical Society of America.

[72] Ibrahim Sadiek, Tommi Mikkonen, Markku Vainio, Juha Toivonen, and Aleksandra Foltynowicz. Optical frequency comb photoacoustic spectroscopy. *Physical Chemistry Chemical Physics*, 20(44):27849–27855, 2018.

[73] Juho Karhu, Teemu Tomberg, Francisco Senna Vieira, Guillaume Genoud, Vesa Hänninen, Markku Vainio, Markus Metsälä, Tuomas Hieta, Steven Bell, and Lauri Halonen. Broadband photoacoustic spectroscopy of 14CH4 with a high-power mid-infrared optical frequency comb. *Optics Letters*, 44(5):1142–1145, March 2019. Publisher: Optical Society of America.

[74] Piotr Maslowski. Surpassing the path-limited resolution of Fourier-transform spectrometry with frequency combs. *Physical Review A*, 93(2):021802, 2016.

[75] Albert Schliesser, Markus Brehm, Fritz Keilmann, and Daniel W. van der Weide. Frequency-comb infrared spectrometer for rapid, remote chemical sensing. *Optics Express*, 13(22):9029–9038, October 2005.

[76] Ian Coddington. Coherent Multiheterodyne Spectroscopy Using Stabilized Optical Frequency Combs. *Physical Review Letters*, 100(1):013902, 2008.

[77] A. M. Zolot, F. R. Giorgetta, E. Baumann, J. W. Nicholson, W. C. Swann, I. Coddington, and N. R. Newbury. Direct-comb molecular spectroscopy with accurate, resolved comb teeth over 43 THz. *Optics Letters*, 37(4):638–640, February 2012. publisher: Optical Society of America.

[78] Takuro Ideguchi, Tasuku Nakamura, Yohei Kobayashi, and Keisuke Goda. Kerr-lens mode-locked bidirectional dual-comb ring laser for broadband dual-comb spectroscopy. *Optica*, 3(7):748–753, July 2016. Publisher: Optical Society of America.

[79] S. Mehravar, R. A. Norwood, N. Peyghambarian, and K. Kieu. Real-time dual-comb spectroscopy with a free-running bidirectionally mode-locked fiber laser. *Applied Physics Letters*, 108(23):231104, June 2016. Publisher: American Institute of Physics.

[80] Xin Zhao, Guoqing Hu, Bofeng Zhao, Cui Li, Yingling Pan, Ya Liu, Takeshi Yasui, and Zheng Zheng. Picometer-resolution dual-comb spectroscopy with a free-running fiber laser. *Optics Express*, 24(19):21833–21845, September 2016. Publisher: Optical Society of America.

[81] S. M. Link, D. J. H. C. Maas, D. Waldburger, and U. Keller. Dual-comb spectroscopy of water vapor with a free-running semiconductor disk laser. *Science*, 356(6343):1164–1168, June 2017. Publisher: American Association for the Advancement of Science Section: Reports.

[82] Nicolas Bourbeau Hébert, David G. Lancaster, Vincent Michaud-Belleau, George Y. Chen, and Jérôme Genest. Highly coherent free-running dual-comb chip platform. *Optics Letters*, 43(8):1814–1817, April 2018. Publisher: Optical Society of America.

[83] Zaijun Chen, Ming Yan, Theodor W. Hänsch, and Nathalie Picqué. A phase-stable dual-comb interferometer. *Nature Communications*, 9(1):1–7, August 2018. Number: 1 Publisher: Nature Publishing Group.

[84] Pedro Martín-Mateos, Borja Jerez, Pedro Largo-Izquierdo, and Pablo Acedo. Frequency accurate coherent electro-optic dual-comb spectroscopy in real-time. *Optics Express*, 26(8):9700–9713, April 2018. Publisher: Optical Society of America.

[85] Chenglin Gu, Zhong Zuo, Daping Luo, Zejiang Deng, Yang Liu, Minglie Hu, and Wenxue Li. Passive coherent dual-comb spectroscopy based on optical-optical modulation with free running lasers. *PhotoniX*, 1(1):7, March 2020.

[86] Gabriel Ycas, Fabrizio R. Giorgetta, Esther Baumann, Ian Coddington, Daniel Herman, Scott A. Diddams, and Nathan R. Newbury. High-coherence mid-infrared dual-comb spectroscopy spanning 2.6 to 5.2 um. *Nature Photonics*, 12(4):202–208, April 2018. Number: 4 Publisher: Nature Publishing Group.

[87] A. V. Muraviev, V. O. Smolski, Z. E. Loparo, and K. L. Vodopyanov. Massively parallel sensing of trace molecules and their isotopologues with broadband subharmonic mid-infrared frequency combs. *Nature Photonics*, 12(4):209–214, April 2018. Number: 4 Publisher: Nature Publishing Group.

[88] M. Imrul Kayes, Nurmemet Abdukerim, Alexandre Rekik, and Martin Rochette. Free-running mode-locked laser based dual-comb spectroscopy. *Optics Letters*, 43(23):5809–5812, December 2018. Publisher: Optical Society of America.

[89] Ruoyu Liao, Youjian Song, Wu Liu, Haosen Shi, Lu Chai, and Minglie Hu. Dual-comb spectroscopy with a single free-running thulium-doped fiber laser. *Optics Express*, 26(8):11046–11054, April 2018. Publisher: Optical Society of America.

[90] Pauli Virtanen, Ralf Gommers, Travis E. Oliphant, Matt Haberland, Tyler Reddy, David Cournapeau, Evgeni Burovski, Pearu Peterson, Warren Weckesser, Jonathan Bright, Stéfan J. van der Walt, Matthew Brett, Joshua Wilson, K. Jarrod Millman, Nikolay Mayorov, Andrew R. J. Nelson, Eric Jones, Robert Kern, Eric Larson, C. J. Carey, İlhan Polat, Yu Feng, Eric W. Moore, Jake VanderPlas, Denis Laxalde, Josef Perktold, Robert Cimrman, Ian Henriksen, E. A. Quintero, Charles R. Harris, Anne M. Archibald, Antônio H. Ribeiro, Fabian Pedregosa, and Paul van Mulbregt. SciPy 1.0: fundamental algorithms for scientific computing in Python. *Nature Methods*, 17(3):261–272, March 2020. Number: 3 Publisher: Nature Publishing Group.

[91] R.V. Kochanov, I.E. Gordon, L.S. Rothman, P. Wcisło, C. Hill, and J.S. Wilzewski. HITRAN Application Programming Interface (HAPI): A comprehensive approach to working with spectroscopic data. *Journal of Quantitative Spectroscopy and Radiative Transfer*, 177:15–30, July 2016.

[92] I.E. Gordon, L.S. Rothman, C. Hill, R.V. Kochanov, Y. Tan, P.F. Bernath, M. Birk, V. Boudon, A. Campargue, K.V. Chance, B.J. Drouin, J.-M. Flaud, R.R. Gamache, J.T. Hodges, D. Jacquemart, V.I. Perevalov, A. Perrin, K.P. Shine, M.-A.H. Smith, J. Tennyson, G.C. Toon, H. Tran, V.G. Tyuterev, A. Barbe, A.G. Császár, V.M. Devi, T. Furtenbacher, J.J. Harrison, J.-M. Hartmann, A. Jolly, T.J. Johnson, T. Karman, I. Kleiner, A.A. Kyuberis, J. Loos, O.M. Lyulin, S.T. Massie, S.N. Mikhailenko, N. Moazzen-Ahmadi, H.S.P. Müller, O.V. Naumenko, A.V. Nikitin, O.L. Polyansky, M. Rey, M. Rotger, S.W. Sharpe, K. Sung, E. Starikova, S.A.

Tashkun, J. Vander Auwera, G. Wagner, J. Wilzewski, P. Wcisło, S. Yu, and E.J. Zak. The HITRAN2016 molecular spectroscopic database. *Journal of Quantitative Spectroscopy and Radiative Transfer*, 203:3–69, December 2017.

[93] Julien Roy, Jean-Daniel Deschênes, Simon Potvin, and Jérôme Genest. Continuous real-time correction and averaging for frequency comb interferometry. *Optics Express*, 20(20):21932–21939, September 2012. Publisher: Optical Society of America.

[94] David Burghoff, Yang Yang, and Qing Hu. Computational multiheterodyne spectroscopy. *Science Advances*, 2(11):e1601227, November 2016. Publisher: American Association for the Advancement of Science Section: Research Article.

[95] Nicolas Bourbeau Hébert, Jérôme Genest, Jean-Daniel Deschênes, Hugo Bergeron, George Y. Chen, Champak Khurmi, and David G. Lancaster. Self-corrected chip-based dual-comb spectrometer. *Optics Express*, 25(7):8168–8179, April 2017. Publisher: Optical Society of America.

[96] Yunhao Zhu, Guan Xu, Jie Yuan, Janggun Jo, Girish Gandikota, Hakan Demirci, Toshitaka Agano, Naoto Sato, Yusuke Shigeta, and Xueding Wang. Light Emitting Diodes based Photoacoustic Imaging and Potential Clinical Applications. *Scientific Reports*, 8(1):1–12, June 2018. Number: 1 Publisher: Nature Publishing Group.

[97] Lukasz A. Sterczewski, Jonas Westberg, and Gerard Wysocki. Computational coherent averaging for free-running dual-comb spectroscopy. *Optics Express*, 27(17):23875–23893, August 2019.

[98] F. G. C. Bijnen, J. Reuss, and F. J. M. Harren. Geometrical optimization of a longitudinal resonant photoacoustic cell for sensitive and fast trace gas detection. *Review of Scientific Instruments*, 67(8):2914–2923, August 1996. Publisher: American Institute of Physics.

[99] Zaijun Chen, Theodor W. Hänsch, and Nathalie Picqué. Upconversion mid-infrared dual-comb spectroscopy. *arXiv:2003.06930 [physics]*, March 2020. arXiv: 2003.06930.

[100] Birgitta Bernhardt, Akira Ozawa, Patrick Jacquet, Marion Jacquey, Yohei Kobayashi, Thomas Udem, Ronald Holzwarth, Guy Guelachvili, Theodor W. Hänsch, and Nathalie Picqué. Cavity-enhanced dual-comb spectroscopy. *Nature Photonics*, 4(1):55–57, January 2010. Number: 1 Publisher: Nature Publishing Group.

[101] Frans J.M. Harren and Simona M. Cristescu. Photoacoustic Spectroscopy in Trace Gas Monitoring. *Encyclopedia of Analytical Chemistry*, pages 1–29, March 2019.

[102] Gustavo Villares, Andreas Hugi, Stéphane Blaser, and Jérôme Faist. Dual-comb spectroscopy based on quantum-cascade-laser frequency combs. *Nature Communications*, 5(1):1–9, October 2014. Number: 1 Publisher: Nature Publishing Group.

[103] Michele Gianella, Akshay Nataraj, Béla Tuzson, Pierre Jouy, Filippos Kapsalidis, Mattias Beck, Markus Mangold, Andreas Hugi, Jérôme Faist, and Lukas Emmenegger. High-resolution and gapless dual comb spectroscopy with current-tuned quantum cascade lasers. *Optics Express*, 28(5):6197–6208, March 2020. Publisher: Optical Society of America.

[104] Amir Rosenthal, Daniel Razansky, and Vasilis Ntziachristos. High-sensitivity compact ultrasonic detector based on a pi-phase-shifted fiber Bragg grating. *Optics Letters*, 36(10):1833–1835, May 2011. Publisher: Optical Society of America.

[105] Debra A. Fischer, Guillem Anglada-Escude, Pamela Arriagada, Roman V. Baluev, Jacob L. Bean, Francois Bouchy, Lars A. Buchhave, Thorsten Carroll, Abhijit Chakraborty, Justin R. Crepp, Rebekah I. Dawson, Scott A. Diddams, Xavier Dumusque, Jason D. Eastman, Michael Endl, Pedro Figueira, Eric B. Ford, Daniel Foreman-Mackey, Paul Fournier, Gabor Fűrész, B. Scott Gaudi, Philip C. Gregory, Frank Grundahl, Artie P. Hatzes, Guillaume Hébrard, Enrique Herrero, David W. Hogg, Andrew W. Howard, John A. Johnson, Paul Jorden, Colby A. Jurgenson, David W. Latham, Greg Laughlin, Thomas J. Loredo, Christophe Lovis, Suvrath Mahadevan, Tyler M. McCracken, Francesco Pepe, Mario Perez, David F. Phillips, Peter P. Plavchan, Lisa Prato, Andreas Quirrenbach, Ansgar Reiners, Paul Robertson, Nuno C. Santos, David Sawyer, Damien Segransan, Alessandro Sozzetti, Tilo Steinmetz, Andrew Szentgyorgyi, Stéphane Udry, Jeff A. Valenti, Sharon X. Wang, Robert A. Wittenmyer, and Jason T. Wright. State of the Field: Extreme Precision Radial Velocities. *Publications of the Astronomical Society of the Pacific*, 128(964):1–43, 2016.

[106] E. Gavartin, P. Verlot, and T. J. Kippenberg. A hybrid on-chip optomechanical transducer for ultrasensitive force measurements. *Nature Nanotechnology*, 7(8):509–514, August 2012. Number: 8 Publisher: Nature Publishing Group.

[107] Birgit Stiller, Paulo Dainese, and Ewold Verhagen. Optoacoustics—Advances in high-frequency optomechanics and Brillouin scattering. *APL Photonics*, 4:110401, May 2019. Publisher: American Institute of Physics.

[108] David Mason, Junxin Chen, Massimiliano Rossi, Yeghishe Tsaturyan, and Albert Schliesser. Continuous force and displacement measurement below the standard quantum limit. *Nature Physics*, 15(8):745–749, August 2019. Number: 8 Publisher: Nature Publishing Group.

[109] T. Herr, V. Brasch, J. D. Jost, C. Y. Wang, N. M. Kondratiev, M. L. Gorodetsky, and T. J. Kippenberg. Temporal solitons in optical microresonators. *Nature Photonics*, 8:145–152, February 2014.

[110] M.-G. Suh, Q.-F. Yang, K. Y. Yang, X. Yi, and K. J. Vahala. Microresonator soliton dual-comb spectroscopy. *Science*, 354:600–603, November 2016.

[111] Tobias J. Kippenberg, Alexander L. Gaeta, Michal Lipson, and Michael L. Gorodetsky. Dissipative Kerr solitons in optical microresonators. *Science*, 361(6402), August 2018. Publisher: American Association for the Advancement of Science Section: Review.

[112] Jacob T. Friedlein, Esther Baumann, Kimberly A. Briggman, Gabriel M. Colacion, Fabrizio R. Giorgetta, Aaron M. Goldfain, Daniel I. Herman, Eli V. Hoenig, Jeeseong Hwang, Nathan R. Newbury, Edgar F. Perez, Christopher S. Yung, Ian Coddington, and Kevin C. Cossel. Dual-comb photoacoustic spectroscopy. *Nature Communications*, 11(1):3152, June 2020.

[113] David Bannon. Cubes and slices. *Nature Photonics*, 3(11):627–629, November 2009. Number: 11 Publisher: Nature Publishing Group.

[114] Alexander F. H. Goetz, Gregg Vane, Jerry E. Solomon, and Barrett N. Rock. Imaging Spectrometry for Earth Remote Sensing. *Science*, 228(4704):1147–1153, June 1985. Publisher: American Association for the Advancement of Science Section: Articles.

[115] Guolan Lu and Baowei Fei. Medical hyperspectral imaging: a review. *Journal of Biomedical Optics*, 19(1):10901, January 2014. tex.ids: lu2014a.

[116] Pedro Martín-Mateos, Farid Ullah Khan, and Oscar Elías Bonilla-Manrique. Direct hyperspectral dual-comb imaging. *Optica*, 7(3):199–202, March 2020.

[117] Farid Ullah Khan, Guillermo Guarnizo, and Pedro Martín-Mateos. Direct hyperspectral dual-comb gas imaging in the mid-infrared. *Optics Letters*, August 2020. Publisher: Optical Society of America.

[118] Yann LeCun, Bernhard E. Boser, John S. Denker, Donnie Henderson, R. E. Howard, Wayne E. Hubbard, and Lawrence D. Jackel. Handwritten digit recognition with a back-propagation network. In D. S. Touretzky, editor, *Advances in neural information processing systems 2*, pages 396–404. Morgan-Kaufmann, 1990.

[119] Yann LeCun, Yoshua Bengio, and Geoffrey Hinton. Deep learning. *Nature*, 521(7553):436–444, May 2015. Number: 7553 Publisher: Nature Publishing Group.

[120] Alex Krizhevsky, Ilya Sutskever, and Geoffrey E. Hinton. ImageNet classification with deep convolutional neural networks. *Communications of the ACM*, 60(6):84–90, May 2017.

[121] Thibault Wildi, Thibault Voumard, Victor Brasch, Gürkan Yilmaz, and Tobias Herr. Photo-acoustic dual-frequency comb spectroscopy. *Nature Communications*, 11(1):4164, August 2020.

[122] Martín Abadi, Ashish Agarwal, Paul Barham, Eugene Brevdo, Zhifeng Chen, Craig Citro, Greg S. Corrado, Andy Davis, Jeffrey Dean, Matthieu Devin, Sanjay Ghemawat, Ian Goodfellow, Andrew Harp, Geoffrey Irving, Michael Isard, Yangqing Jia, Rafal Jozefowicz, Lukasz Kaiser, Manjunath Kudlur, Josh Levenberg, Dan Mane, Rajat Monga, Sherry Moore, Derek Murray, Chris Olah, Mike Schuster, Jonathon Shlens, Benoit Steiner, Ilya Sutskever, Kunal Talwar, Paul Tucker, Vincent Vanhoucke, Vijay Vasudevan, Fernanda Viegas, Oriol Vinyals, Pete Warden, Martin Wattenberg, Martin Wicke, Yuan Yu, and Xiaoqiang Zheng. TensorFlow: Large-Scale Machine Learning on Heterogeneous Distributed Systems. *arXiv:1603.04467 [cs]*, March 2016. arXiv: 1603.04467.

[123] Andrew Lavin and Scott Gray. Fast Algorithms for Convolutional Neural Networks. *arXiv:1509.09308 [cs]*, November 2015. arXiv: 1509.09308.

[124] Zhaowei Cai, Quanfu Fan, Rogerio S. Feris, and Nuno Vasconcelos. A Unified Multi-scale Deep Convolutional Neural Network for Fast Object Detection. *arXiv:1607.07155 [cs]*, July 2016. arXiv: 1607.07155.

[125] Alexander Kozlov, Ivan Lazarevich, Vasily Shamporov, Nikolay Lyalyushkin, and Yury Gorbachev. Neural Network Compression Framework for fast model inference. *arXiv:2002.08679 [cs, eess]*, March 2020. arXiv: 2002.08679.

[126] Hongchao Ji, Hongmei Lu, and Zhimin Zhang. Predicting Molecular Fingerprint from Electron-Ionization Mass Spectrum with Deep Neural Networks. preprint, Bioinformatics, April 2020.

[127] Jinchao Liu, Margarita Osadchy, Lorna Ashton, Michael Foster, Christopher J. Solomon, and Stuart J. Gibson. Deep Convolutional Neural Networks for Raman Spectrum Recognition: A Unified Solution. *The Analyst*, 142(21):4067–4074, 2017. arXiv: 1708.09022.

[128] Jacopo Acquarelli, Twan van Laarhoven, Jan Gerretzen, Thanh Tran, Lutgarde Buydens, and Elena Marchiori. Convolutional neural networks for vibrational spectroscopic data analysis. *Analytica Chimica Acta*, 954, December 2016.

[129] Kunal Ghosh, Annika Stuke, Milica Todorović, Peter Bjørn Jørgensen, Mikkel N. Schmidt, Aki Vehtari, and Patrick Rinke. Deep

Learning Spectroscopy: Neural Networks for Molecular Excitation Spectra. *Advanced Science*, 6(9):1801367, 2019. _eprint: https://onlinelibrary.wiley.com/doi/pdf/10.1002/advs.201801367.

[130] Monika Gniadecka, Peter Alshede Philipsen, Sonja Wessel, Robert Gniadecki, Hans Christian Wulf, Sigurdur Sigurdsson, Ole Faurskov Nielsen, Daniel Højgaard Christensen, Jana Hercogova, Kristian Rossen, Henrik Klem Thomsen, and Lars Kai Hansen. Melanoma Diagnosis by Raman Spectroscopy and Neural Networks: Structure Alterations in Proteins and Lipids in Intact Cancer Tissue. *Journal of Investigative Dermatology*, 122(2):443–449, February 2004.

[131] C. Y. Wang, T. Herr, P. Del'Haye, A. Schliesser, J. Hofer, R. Holzwarth, T. W. Hänsch, N. Picqué, and T. J. Kippenberg. Mid-infrared optical frequency combs at 2.5 um based on crystalline microresonators. *Nature Communications*, 4(1):1–7, January 2013. Number: 1 Publisher: Nature Publishing Group.

[132] Mengjie Yu, Yoshitomo Okawachi, Austin G. Griffith, Nathalie Picqué, Michal Lipson, and Alexander L. Gaeta. Silicon-chip-based mid-infrared dual-comb spectroscopy. *Nature Communications*, 9(1):1–6, May 2018. Number: 1 Publisher: Nature Publishing Group.

[133] Abijith Kowligy, David Carlson, Daniel Hickstein, Henry Timmers, Alex Lind, Peter Schunemann, Scott Papp, and Scott Diddams. Mid-infrared frequency combs at 10 GHz. *arXiv:2005.13049 [physics]*, May 2020. arXiv: 2005.13049.

[134] Xavier Glorot, Antoine Bordes, and Yoshua Bengio. Deep Sparse Rectifier Neural Networks. In *Proceedings of the Fourteenth International Conference on Artificial Intelligence and Statistics*, pages 315–323, June 2011. ISSN: 1938-7228 Section: Machine Learning.

[135] Nitish Srivastava, Geoffrey Hinton, Alex Krizhevsky, Ilya Sutskever, and Ruslan Salakhutdinov. Dropout: A simple way to prevent neural networks from overfitting. *Journal of Machine Learning Research*, 15(56):1929–1958, 2014.

[136] I. Coddington. Coherent dual-comb spectroscopy at high signal-to-noise ratio. *Physical Review A*, 82(4), 2010.

[137] Yoshiaki Nakjima, Yuya Hata, and Kaoru Minoshima. High-coherence ultra-broadband bidirectional dual-comb fiber laser. *Optics Express*, 27(5):5931, March 2019.

[138] Xinyi Ren, Hu Dai, Detian Li, Kun Huang, Mengyun Hu, Tianjian Lv, Ming Yan, and Heping Zeng. Mid-infrared electro-optic dual-comb spectroscopy with feedforward frequency stepping. *Optics Letters*, 45(3):776–779, February 2020. Publisher: Optical Society of America.

[139] Philippe Guay, Jérôme Genest, and Adam J. Fleisher. Precision spectroscopy of $H^{13}CN$ using a free-running, all-fiber dual electro-optic frequency comb system. *Optics Letters*, 43(6):1407–1410, March 2018.

[140] David R. Carlson, Daniel D. Hickstein, and Scott B. Papp. Broadband, electro-optic, dual-comb spectrometer for linear and nonlinear measurements. *Optics Express*, 28(20):29148–29154, September 2020. Publisher: Optical Society of America.

[141] Thibault Voumard, Thibault Wildi, Victor Brasch, Raúl Gutiérrez Álvarez, Germán Vergara Ogando, and Tobias Herr. AI-enabled real-time dual-comb molecular fingerprint imaging. *Optics Letters*, 45(24):6583–6586, December 2020.

[142] I. Hartl, A. Ruehl, R. Thapa, H. A. Mckay, B. K. Thomas, L. Fu, L. Dong, and M. E. Fermann. Rapidly scanning fourier transform spectrometer based on a ghz repetition rate yb-fiber laser pair. In *(2009), paper CPDA6*, page CPDA6. Optical Society of America, May 2009.

[143] Kathrin J. Mohler, Bernhard J. Bohn, Ming Yan, Gwénaëlle Mélen, Theodor W. Hänsch, and Nathalie Picqué. Dual-comb coherent Raman spectroscopy with lasers of 1-GHz pulse repetition frequency. *Optics Letters*, 42(2):318, January 2017.

[144] Nazanin Hoghooghi, Ryan K. Cole, and Gregory B. Rieker. 11-μs time-resolved, continuous dual-comb spectroscopy with spectrally filtered mode-locked frequency combs. *Applied Physics B*, 127(2):17, January 2021.

[145] Yu Zhang, Reagan R. D. Weeks, Caroline Lecaplain, Sivanandan S. Harilal, Jeremy Yeak, Mark C. Phillips, and R. Jason Jones. Burst-mode dual-comb spectroscopy. *Optics Letters*, 46(4):860–863, February 2021.

[146] Kasper Van Gasse et al. An on-chip III-V-semiconductor-on-silicon laser frequency comb for gas-phase molecular spectroscopy in real-time. *arXiv:2006.15113*, 2020.

[147] Kazuki Hashimoto, Venkata Ramaiah Badarla, and Takuro Ideguchi. High-Speed Fourier-Transform Infrared Spectroscopy with Phase-Controlled Delay Line. *Laser & Photonics Reviews*, 15(1):2000374, 2021.

[148] T. Preuschoff, M. Schlosser, and G. Birkl. Digital laser frequency and intensity stabilization based on the STEMlab platform (originally Red Pitaya). *Review of Scientific Instruments*, 91(8):083001, August 2020. Publisher: American Institute of Physics.

[149] L. C. Sinclair, J.-D. Deschênes, L. Sonderhouse, W. C. Swann, I. H. Khader, E. Baumann, N. R. Newbury, and I. Coddington. Invited Article: A compact optically coherent fiber frequency comb. *Review of Scientific*

Instruments, 86(8):081301, August 2015. Publisher: American Institute of Physics.

[150] L. Neuhaus, R. Metzdorff, S. Chua, T. Jacqmin, T. Briant, A. Heidmann, P.-F. Cohadon, and S. Deléglise. Pyrpl (python red pitaya lockbox) — an open-source software package for fpga-controlled quantum optics experiments. In *2017 (CLEO/Europe-EQEC)*, pages 1–1, June 2017.

[151] Daniel M. B. Lesko et al. Fully phase-stabilized 1 GHz turnkey frequency comb at 1.56 μm. *OSA Continuum*, 3(8):2070–2077, August 2020. Publisher: Optical Society of America.

[152] Jenna Bergevin, Tsung-Han Wu, Jeremy Yeak, Brian E. Brumfield, Sivanandan S. Harilal, Mark C. Phillips, and R. Jason Jones. Dual-comb spectroscopy of laser-induced plasmas. *Nature Communications*, 9(1):1273, March 2018.

[153] Shuai Wang, Xinyu Fan, Bingxin Xu, and Zuyuan He. Fast MHz spectral-resolution dual-comb spectroscopy with electro-optic modulators. *Optics Letters*, 44(1):65–68, January 2019. Publisher: Optical Society of America.

[154] Pei-Ling Luo, Er-Chien Horng, and Yu-Chan Guan. Fast molecular fingerprinting with a coherent, rapidly tunable dual-comb spectrometer near 3 μm. *Physical Chemistry Chemical Physics*, 21(33):18400–18405, August 2019. Publisher: The Royal Society of Chemistry.

[155] Risako Kameyama, Sigekazu Takizawa, K. Hiramatsu, and K. Goda. Fast, sensitive dual-comb CARS spectroscopy with a quasi-dual-comb laser. In *BiOS*, 2021.

[156] A. Baranne, D. Queloz, M. Mayor, G. Adrianzyk, G. Knispel, D. Kohler, D. Lacroix, J.-P. Meunier, G. Rimbaud, and A. Vin. ELODIE: A spectrograph for accurate radial velocity measurements. *Astronomy and Astrophysics Supplement Series*, 119(2):373–390, October 1996.

[157] Allan Sandage, Philippe Véron, and John D. Wyndham. Optical Identification of New Quasi-Stellar Radio Sources. *The Astrophysical Journal*, 142:1307–1311, October 1965.

[158] John K. Webb, Victor V. Flambaum, Christopher W. Churchill, Michael J. Drinkwater, and John D. Barrow. Search for Time Variation of the Fine Structure Constant. *Physical Review Letters*, 82(5):884–887, February 1999.

[159] J. Liske, A. Grazian, E. Vanzella, M. Dessauges, M. Viel, L. Pasquini, M. Haehnelt, S. Cristiani, F. Pepe, G. Avila, P. Bonifacio, F. Bouchy, H. Dekker, B. Delabre, S. D'Odorico, V. D'Odorico, S. Levshakov, C. Lovis, M. Mayor, P. Molaro, L. Moscardini, M. T. Murphy, D. Queloz, P. Shaver, S. Udry, T. Wiklind, and S. Zucker. Cosmic dynamics in the

era of Extremely Large Telescopes. *Monthly Notices of the Royal Astronomical Society*, 386(3):1192–1218, May 2008.

[160] Alessandro Marconi, M. Abreu, V. Adibekyan, V. Alberti, S. Albrecht, J. Alcaniz, M. Aliverti, C. Allende Prieto, J. D. Alvarado Gómez, P. J. Amado, M. Amate, M. I. Andersen, E. Artigau, C. Baker, V. Baldini, A. Balestra, S. A. Barnes, F. Baron, S. C. C. Barros, S. M. Bauer, M. Beaulieu, O. Bellido-Tirado, B. Benneke, T. Bensby, E. A. Bergin, K. Biazzo, A. Bik, J. Birkby, N. Blind, I. Boisse, E. Bolmont, M. Bonaglia, X. Bonfils, F. Borsa, A. Brandeker, W. Brandner, C. H. Broeg, M. Brogi, D. Brousseau, A. Brucalassi, J. Brynnel, L. A. Buchhave, D. F. Buscher, A. Cabral, G. Calderone, R. Calvo-Ortega, B. L. Canto Martins, F. Cantalloube, L. Carbonaro, G. Chauvin, B. Chazelas, A.-L. Cheffot, Y. S. Cheng, A. Chiavassa, L. Christensen, R. Cirami, N. J. Cook, R. J. Cooke, I. Coretti, S. Covino, N. Cowan, G. Cresci, S. Cristiani, V. Cunha Parro, G. Cupani, V. D'Odorico, I. De Castro Leão, A. De Cia, J. R. De Medeiros, F. Debras, M. Debus, O. Demangeon, M. Dessauges-Zavadsky, P. Di Marcantonio, F. Dionies, R. Doyon, J. Dunn, D. Ehrenreich, J. P. Faria, C. Feruglio, M. Fisher, A. Fontana, M. Fumagalli, T. Fusco, J. Fynbo, O. Gabella, W. Gaessler, E. Gallo, X. Gao, L. Genolet, M. Genoni, P. Giacobbe, E. Giro, R. S. Gonçalves, O. Gonzalez, J. I. González Hernández, F. Gracia Témich, M. G. Haehnelt, C. Haniff, A. Hatzes, R. Helled, H.J. Hoeijmakers, P. Huke, S. Järvinen, A. Järvinen, A. Kaminski, A. Korn, D. Kouach, Grzegorz Kowzan, L. Kreidberg, M. Landoni, A. Lanotte, A. Lavail, J. Li, J. Liske, C. Lovis, S. Lucatello, D. Lunney, M. MacIntosh, N. Madhusudhan, L. Magrini, R. Maiolino, L. Malo, A. Man, T. Marquart, E. L. Marques, A. M. Martins, C. J. A. P. Martins, P. Maslowski, C. Mason, E. Mason, R. A. McCracken, P. Mergo, G. Micela, T. Mitchell, P. Mollière, M. Monteiro, D. Montgomery, C. Mordasini, J. Morin, A. Mucciarelli, M. T. Murphy, M. N'Diaye, B. Neichel, A. T. Niedzielski, E. Niemczura, L. Nortmann, P. Noterdaeme, N. Nunes, L. Oggioni, E. Oliva, H. Önel, L. Origlia, G. Östlin, E. Palle, P. Papaderos, G. Pariani, J. Peñate Castro, F. Pepe, L. Perreault Levasseur, P. Petit, L. Pino, J. Piqueras, A. Pollo, K. Poppenhaeger, A. Quirrenbach, E. Rauscher, R. Rebolo, E. M. A. Redaelli, S. Reffert, D. T. Reid, A. Reiners, P. Richter, M. Riva, S. Rivoire, C. Rodríguez-López, I. U. Roederer, D. Romano, Sylvain Rousseau, J. Rowe, S. Salvadori, N. Santos, P. Santos Diaz, J. Sanz-Forcada, Mirsad Sarajlic, J.-F. Sauvage, S. Schäfer, R. P. Schiavon, T. M. Schmidt, C. Selmi, S. Sivanandam, M. Sordet, R. Sordo, F. Sortino, D. Sosnowska, S. G. Sousa, E. Stempels, K. G. Strassmeier, A. Suárez Mascareño, A. Sulich, X. Sun, N.R. Tanvir, F. Tenegi-Sanginés, S. Thibault, S. J. Thompson, A. Tozzi, M. Turbet, P. Vallée, R. Varas, K. Venn, J.-P. Véran, A. Verma, M. Viel, G. Wade, C. Waring, M. Weber, J. Weder, B. Wehbe, J. Weingrill, M. Woche, M. Xompero, E. Zackrisson, A. Zanutta, M. R. Zapatero Osorio, M. Zechmeister, and J. Zimara. ANDES, the high resolution spectrograph for the ELT: Science case, baseline

design and path to construction. In Christopher J. Evans, Julia J. Bryant, and Kentaro Motohara, editors, *Ground-Based and Airborne Instrumentation for Astronomy IX*, page 75, Montréal, Canada, August 2022. SPIE.

[161] Michael T. Murphy, Paolo Molaro, Ana C. O. Leite, Guido Cupani, Stefano Cristiani, Valentina D'Odorico, Ricardo Génova Santos, Carlos J. A. P. Martins, Dinko Milaković, Nelson J. Nunes, Tobias M. Schmidt, Francesco A. Pepe, Rafael Rebolo, Nuno C. Santos, Sérgio G. Sousa, Maria-Rosa Zapatero Osorio, Manuel Amate, Vardan Adibekyan, Yann Alibert, Carlos Allende Prieto, Veronica Baldini, Willy Benz, François Bouchy, Alexandre Cabral, Hans Dekker, Paolo Di Marcantonio, David Ehrenreich, Pedro Figueira, Jonay I. González Hernández, Marco Landoni, Christophe Lovis, Gaspare Lo Curto, Antonio Manescau, Denis Mégevand, Andrea Mehner, Giuseppina Micela, Luca Pasquini, Ennio Poretti, Marco Riva, Alessandro Sozzetti, Alejandro Suárez Mascareño, Stéphane Udry, and Filippo Zerbi. Fundamental physics with ESPRESSO: Precise limit on variations in the fine-structure constant towards the bright quasar HE 0515-4414. *Astronomy & Astrophysics*, 658:A123, February 2022.

[162] Francois Wildi, Francesco Pepe, Bruno Chazelas, Gaspare Lo Curto, and Christophe Lovis. The performance of the new Fabry-Perot calibration system of the radial velocity spectrograph HARPS. In Stuart Shaklan, editor, *SPIE Optical Engineering + Applications*, page 81511F, San Diego, California, USA, September 2011.

[163] Tobias M. Schmidt, Paolo Molaro, Michael T. Murphy, Christophe Lovis, Guido Cupani, Stefano Cristiani, Francesco A. Pepe, Rafael Rebolo, Nuno C. Santos, Manuel Abreu, Vardan Adibekyan, Yann Alibert, Matteo Aliverti, Romain Allart, Carlos Allende Prieto, David Alves, Veronica Baldini, Christopher Broeg, Alexandre Cabral, Giorgio Calderone, Roberto Cirami, João Coelho, Igor Coretti, Valentina D'Odorico, Paolo Di Marcantonio, David Ehrenreich, Pedro Figueira, Matteo Genoni, Ricardo Génova Santos, Jonay I. González Hernández, Florian Kerber, Marco Landoni, Ana C. O. Leite, Jean-Louis Lizon, Gaspare Lo Curto, Antonio Manescau, Carlos J. A. P. Martins, Denis Megévand, Andrea Mehner, Giuseppina Micela, Andrea Modigliani, Manuel Monteiro, Mario J. P. F. G. Monteiro, Eric Mueller, Nelson J. Nunes, Luca Oggioni, António Oliveira, Giorgio Pariani, Luca Pasquini, Edoardo Redaelli, Marco Riva, Pedro Santos, Danuta Sosnowska, Sérgio G. Sousa, Alessandro Sozzetti, Alejandro Suárez Mascareño, Stéphane Udry, Maria-Rosa Zapatero Osorio, and Filippo Zerbi. Fundamental physics with ESPRESSO: Towards an accurate wavelength calibration for a precision test of the fine-structure constant. *Astronomy & Astrophysics*, 646:A144, February 2021.

[164] M. J. Hobson, F. Bouchy, N. J. Cook, E. Artigau, C. Moutou, I. Boisse, C. Lovis, A. Carmona, X. Delfosse, and J.-F. Donati. The SPIRou wavelength calibration for precise radial velocities in the near infrared. *Astronomy & Astrophysics*, 648:A48, April 2021.

[165] F. Cersullo, A. Coffinet, B. Chazelas, C. Lovis, and F. Pepe. New wavelength calibration for echelle spectrographs using Fabry-Pérot etalons. *Astronomy & Astrophysics*, 624:A122, April 2019.

[166] Christian Schwab, Tobias Feger, Julian Stürmer, Andreas Seifahrt, Yulia V. Gurevich, Dmytro Rogozin, Thorsten Führer, Samuel P. Halverson, Ryan C. Terrien, Thomas Legero, David W. Coutts, Gert Raskin, Thomas Walther, Jacob L. Bean, and Andreas Quirrenbach. Rubidium traced etalon wavelength calibrators: Towards deployment at observatories. In *Ground-Based and Airborne Instrumentation for Astronomy VII*, volume 10702, pages 2102–2108. SPIE, July 2018.

[167] Julian Stürmer, Andreas Seifahrt, Christian Schwab, and Jacob L. Bean. A rubidium traced white-light etalon calibrator for MAROON-X. In *Advances in Optical and Mechanical Technologies for Telescopes and Instrumentation II*, volume 9912, pages 777–785. SPIE, July 2016.

[168] Julian Stürmer, Andreas Seifahrt, Christian Schwab, and Jacob L. Bean. Rubidium-traced white-light etalon calibrator for radial velocity measurements at the cm s-1 level. *Journal of Astronomical Telescopes, Instruments, and Systems*, 3(2):025003, June 2017.

[169] T. M. McCracken, C. A. Jurgenson, D. A. Fischer, R. A. Stoll, A. E. Szymkowiak, J. Bradford, and W. Rutter. Single-lock: A stable Fabry-Perot based wavelength calibrator. In *Ground-Based and Airborne Instrumentation for Astronomy V*, volume 9147, pages 1190–1198. SPIE, July 2014.

[170] R. K. Banyal and A. Reiners. A Dual Cavity Fabry–Perot Device for High Precision Doppler Measurements in Astronomy. *Journal of Astronomical Instrumentation*, 06(01):1750001, March 2017.

[171] Jeff Jennings, Ryan Terrien, Connor Fredrick, Michael Grisham, Mark Notcutt, Samuel Halverson, Suvrath Mahadevan, and Scott A. Diddams. Frequency stability of the mode spectrum of broad bandwidth Fabry-Pérot interferometers. *OSA Continuum*, 3(5):1177–1193, May 2020.

[172] Tobias M. Schmidt, Bruno Chazelas, Christophe Lovis, Xavier Dumusque, François Bouchy, Francesco Pepe, Pedro Figueira, and Danuta Sosnowska. Chromatic drift of the Espresso Fabry-Pérot etalon. *Astronomy & Astrophysics*, 664:A191, August 2022.

[173] David F. Phillips, Alexander G. Glenday, Chih-Hao Li, Claire Cramer, Gabor Furesz, Guoqing Chang, Andrew J. Benedick, Li-Jin Chen, Franz X. Kärtner, Sylvain Korzennik, Dimitar Sasselov, Andrew Szentgyorgyi, and Ronald L. Walsworth. Calibration of an astrophysical spectrograph below 1 m/s using a laser frequency comb. *Optics Express*, 20(13):13711–13726, June 2012.

[174] Richard A. McCracken, Éric Depagne, Rudolf B. Kuhn, Nicolas Erasmus, Lisa A. Crause, and Derryck T. Reid. Wavelength calibration of a high resolution spectrograph with a partially stabilized 15-GHz astrocomb from 550 to 890 nm. *Optics Express*, 25(6):6450–6460, March 2017.

[175] Nemanja Jovanovic, Pradip Gatkine, Narsireddy Anugu, Rodrigo Amezcua-Correa, Ritoban Basu Thakur, Charles Beichman, Chad Bender, Jean-Philippe Berger, Azzurra Bigioli, Joss Bland-Hawthorn, Guillaume Bourdarot, Charles M. Bradford, Ronald Broeke, Julia Bryant, Kevin Bundy, Ross Cheriton, Nick Cvetojevic, Momen Diab, Scott A. Diddams, Aline N. Dinkelaker, Jeroen Duis, Stephen Eikenberry, Simon Ellis, Akira Endo, Donald F. Figer, Michael Fitzgerald, Itandehui Gris-Sanchez, Simon Gross, Ludovic Grossard, Olivier Guyon, Sebastiaan Y. Haffert, Samuel Halverson, Robert J. Harris, Jinping He, Tobias Herr, Philipp Hottinger, Elsa Huby, Michael Ireland, Rebecca Jenson-Clem, Jeffrey Jewell, Laurent Jocou, Stefan Kraus, Lucas Labadie, Sylvestre Lacour, Romain Laugier, Katarzyna Ławniczuk, Jonathan Lin, Stephanie Leifer, Sergio Leon-Saval, Guillermo Martin, Frantz Martinache, Marc-Antoine Martinod, Ben Mazin, Stefano Minardi, John D Monnier, Reinan Moreira, Denis Mourard, Abani Shankar Shankar Nayak, Barnaby Norris, Ewelina Obrzud, Karine Perraut, François Reynaud, Steph Sallum, David Schiminovich, Christian Schwab, Eugene Serbayn, Sherif Soliman, Andreas Stoll, Liang Tang, Peter Tuthill, Kerry Vahala, Gautam Vasisht, Sylvain Veilleux, Alexander B. Walter, Edward J Wollack, Yinzi Xin, Zongyin Yang, Stephanos Yerolatsitis, Yang Zhang, and Chang-Ling Zou. 2023 Astrophotonics Roadmap: Pathways to realizing multi-functional integrated astrophotonic instruments. *Journal of Physics: Photonics*, 2023.

[176] Tilo Steinmetz, Tobias Wilken, Constanza Araujo-Hauck, Ronald Holzwarth, Theodor W. Hänsch, Luca Pasquini, Antonio Manescau, Sandro D'Odorico, Michael T. Murphy, Thomas Kentischer, Wolfgang Schmidt, and Thomas Udem. Laser Frequency Combs for Astronomical Observations. *Science*, 321(5894):1335–1337, September 2008.

[177] Chih-Hao Li, Andrew J. Benedick, Peter Fendel, Alexander G. Glenday, Franz X. Kärtner, David F. Phillips, Dimitar Sasselov, Andrew Szentgyorgyi, and Ronald L. Walsworth. A laser frequency comb that enables radial velocity measurements with a precision of 1 cm s-1. *Nature*, 452(7187):610–612, April 2008.

[178] D. A. Braje, M. S. Kirchner, S. Osterman, T. Fortier, and S. A. Diddams. Astronomical spectrograph calibration with broad-spectrum frequency combs. *The European Physical Journal D*, 48(1):57–66, June 2008.

[179] Andrew J. Benedick, Guoqing Chang, Jonathan R. Birge, Li-Jin Chen, Alexander G. Glenday, Chih-Hao Li, David F. Phillips, Andrew Szentgyorgyi, Sylvain Korzennik, Gabor Furesz, Ronald L. Walsworth, and Franz X.

144

Kärtner. Visible wavelength astro-comb. *Optics Express*, 18(18):19175–19184, August 2010.

[180] Alexander G. Glenday, Chih-Hao Li, Nicholas Langellier, Guoqing Chang, Li-Jin Chen, Gabor Furesz, Alexander A. Zibrov, Franz Kärtner, David F. Phillips, Dimitar Sasselov, Andrew Szentgyorgyi, and Ronald L. Walsworth. Operation of a broadband visible-wavelength astro-comb with a high-resolution astrophysical spectrograph. *Optica*, 2(3):250–254, March 2015.

[181] Yuanjie Wu, Zinan Huang, Tilo Steinmetz, Mark Yeo, Klaus Stockwald, and Ronald Holzwarth. 20 GHz astronomical laser frequency comb with super-broadband spectral coverage. In Christopher J. Evans, Julia J. Bryant, and Kentaro Motohara, editors, *Ground-Based and Airborne Instrumentation for Astronomy IX*, page 53, Montréal, Canada, August 2022. SPIE.

[182] Ken Kashiwagi, Takashi Kurokawa, Yasushi Okuyama, Takahiro Mori, Yosuke Tanaka, Yoshinori Yamamoto, and Masaaki Hirano. Direct generation of 12.5-GHz-spaced optical frequency comb with ultrabroad coverage in near-infrared region by cascaded fiber configuration. *Optics Express*, 24(8):8120–8131, April 2016.

[183] X. Yi, K. Vahala, J. Li, S. Diddams, G. Ycas, P. Plavchan, S. Leifer, J. Sandhu, G. Vasisht, P. Chen, P. Gao, J. Gagne, E. Furlan, M. Bottom, E. C. Martin, M. P. Fitzgerald, G. Doppmann, and C. Beichman. Demonstration of a near-IR line-referenced electro-optical laser frequency comb for precision radial velocity measurements in astronomy. *Nature Communications*, 7(1):10436, January 2016.

[184] E. Obrzud, M. Rainer, A. Harutyunyan, B. Chazelas, M. Cecconi, A. Ghedina, E. Molinari, S. Kundermann, S. Lecomte, F. Pepe, F. Wildi, F. Bouchy, and T. Herr. Broadband near-infrared astronomical spectrometer calibration and on-sky validation with an electro-optic laser frequency comb. *Optics Express*, 26(26):34830–34841, December 2018.

[185] Andrew J. Metcalf, Connor D. Fredrick, Ryan C. Terrien, Scott B. Papp, and Scott A. Diddams. 30 GHz electro-optic frequency comb spanning 300 THz in the near infrared and visible. *Optics Letters*, 44(11):2673–2676, June 2019.

[186] Andrew J. Metcalf, Tyler Anderson, Chad F. Bender, Scott Blakeslee, Wesley Brand, David R. Carlson, William D. Cochran, Scott A. Diddams, Michael Endl, Connor Fredrick, Sam Halverson, Daniel D. Hickstein, Fred Hearty, Jeff Jennings, Shubham Kanodia, Kyle F. Kaplan, Eric Levi, Emily Lubar, Suvrath Mahadevan, Andrew Monson, Joe P. Ninan, Colin Nitroy, Steve Osterman, Scott B. Papp, Franklyn Quinlan, Larry Ramsey, Paul Robertson, Arpita Roy, Christian Schwab, Steinn

Sigurdsson, Kartik Srinivasan, Gudmundur Stefansson, David A. Sterner, Ryan Terrien, Alex Wolszczan, Jason T. Wright, and Gabriel Ycas. Stellar spectroscopy in the near-infrared with a laser frequency comb. *Optica*, 6(2):233–239, February 2019.

[187] Markus Ludwig, Furkan Ayhan, Tobias M. Schmidt, Thibault Wildi, Thibault Voumard, Roman Blum, Zhichao Ye, Fuchuan Lei, François Wildi, Francesco Pepe, Mahmoud A. Gaafar, Ewelina Obrzud, Davide Grassani, François Moreau, Bruno Chazelas, Rico Sottile, Victor Torres-Company, Victor Brasch, Luis G. Villanueva, François Bouchy, and Tobias Herr. Ultraviolet astronomical spectrograph calibration with laser frequency combs from nanophotonic waveguides, June 2023.

[188] Ewelina Obrzud, Monica Rainer, Avet Harutyunyan, Miles H. Anderson, Junqiu Liu, Michael Geiselmann, Bruno Chazelas, Stefan Kundermann, Steve Lecomte, Massimo Cecconi, Adriano Ghedina, Emilio Molinari, Francesco Pepe, François Wildi, François Bouchy, Tobias J. Kippenberg, and Tobias Herr. A microphotonic astrocomb. *Nature Photonics*, 13(1):31–35, January 2019.

[189] Myoung-Gyun Suh, Xu Yi, Yu-Hung Lai, S. Leifer, Ivan S. Grudinin, G. Vasisht, Emily C. Martin, Michael P. Fitzgerald, G. Doppmann, J. Wang, D. Mawet, Scott B. Papp, Scott A. Diddams, C. Beichman, and Kerry Vahala. Searching for exoplanets using a microresonator astrocomb. *Nature Photonics*, 13(1):25–30, January 2019.

[190] T. Voumard, J. Darvill, T. Wildi, M. Ludwig, C. Mohr, I. Hartl, and T. Herr. 1-GHz dual-comb spectrometer with high mutual coherence for fast and broadband measurements. *Optics Letters*, 47(6):1379–1382, March 2022.

[191] P. Del'Haye, O. Arcizet, M. L. Gorodetsky, R. Holzwarth, and T. J. Kippenberg. Frequency comb assisted diode laser spectroscopy for measurement of microcavity dispersion. *Nature Photonics*, 3(9):529–533, September 2009.

[192] John M. Dudley, Goëry Genty, and Stéphane Coen. Supercontinuum generation in photonic crystal fiber. *Reviews of Modern Physics*, 78(4):1135–1184, October 2006.

[193] T. Sylvestre, E. Genier, E. Genier, A. N. Ghosh, A. N. Ghosh, P. Bowen, G. Genty, J. Troles, A. Mussot, A. C. Peacock, M. Klimczak, A. M. Heidt, J. C. Travers, O. Bang, O. Bang, and J. M. Dudley. Recent advances in supercontinuum generation in specialty optical fibers [Invited]. *JOSA B*, 38(12):F90–F103, December 2021.

[194] Michael R. E. Lamont, Barry Luther-Davies, Duk-Yong Choi, Steve Madden, and Benjamin J. Eggleton. Supercontinuum generation in dispersion

engineered highly nonlinear ($\gamma = 10$ /W/m) As_2S_3 chalcogenide planar waveguide. *Optics Express*, 16(19):14938–14944, September 2008.

[195] Prakash Koonath, Daniel R. Solli, and Bahram Jalali. Limiting nature of continuum generation in silicon. *Applied Physics Letters*, 93(9):091114, September 2008.

[196] David Duchesne, Marco Peccianti, Michael R. E. Lamont, Marcello Ferrera, Luca Razzari, Francois Légaré, Roberto Morandotti, Sai Chu, Brent E. Little, and David J. Moss. Supercontinuum generation in a high index doped silica glass spiral waveguide. *Optics Express*, 18(2):923–930, January 2010.

[197] Bart Kuyken, Xiaoping Liu, Richard M. Osgood, Roel Baets, Günther Roelkens, and William M. J. Green. Mid-infrared to telecom-band supercontinuum generation in highly nonlinear silicon-on-insulator wire waveguides. *Optics Express*, 19(21):20172–20181, October 2011.

[198] R. Halir, Y. Okawachi, J. S. Levy, M. A. Foster, M. Lipson, and A. L. Gaeta. Ultrabroadband supercontinuum generation in a CMOS-compatible platform. *Optics Letters*, 37(10):1685–1687, May 2012.

[199] Adrea R. Johnson, Aline S. Mayer, Alexander Klenner, Kevin Luke, Erin S. Lamb, Michael R. E. Lamont, Chaitanya Joshi, Yoshitomo Okawachi, Frank W. Wise, Michal Lipson, Ursula Keller, and Alexander L. Gaeta. Octave-spanning coherent supercontinuum generation in a silicon nitride waveguide. *Optics Letters*, 40(21):5117–5120, November 2015.

[200] Hairun Guo, Clemens Herkommer, Adrien Billat, Davide Grassani, Chuankun Zhang, Martin H. P. Pfeiffer, Wenle Weng, Camille-Sophie Brès, and Tobias J. Kippenberg. Mid-infrared frequency comb via coherent dispersive wave generation in silicon nitride nanophotonic waveguides. *Nature Photonics*, 12(6):330–335, June 2018.

[201] Mengjie Yu, Boris Desiatov, Yoshitomo Okawachi, Alexander L. Gaeta, and Marko Lončar. Coherent two-octave-spanning supercontinuum generation in lithium-niobate waveguides. *Optics Letters*, 44(5):1222–1225, March 2019.

[202] Yoshitomo Okawachi, Mengjie Yu, Boris Desiatov, Bok Young Kim, Tobias Hansson, Marko Lončar, Alexander L. Gaeta, Alexander L. Gaeta, and Alexander L. Gaeta. Chip-based self-referencing using integrated lithium niobate waveguides. *Optica*, 7(6):702–707, June 2020.

[203] Jay Rutledge, Anthony Catanese, Daniel D. Hickstein, Daniel D. Hickstein, Scott A. Diddams, Scott A. Diddams, Scott A. Diddams, Thomas K. Allison, Thomas K. Allison, Abijith S. Kowligy, and Abijith S. Kowligy. Broadband ultraviolet-visible frequency combs from cascaded

high-harmonic generation in quasi-phase-matched waveguides. *JOSA B*, 38(8):2252–2260, August 2021.

[204] Ewelina Obrzud, Victor Brasch, Thibault Voumard, Anton Stroganov, Michael Geiselmann, François Wildi, Francesco Pepe, Steve Lecomte, and Tobias Herr. Visible blue-to-red 10 GHz frequency comb via on-chip triple-sum-frequency generation. *Optics Letters*, 44(21):5290–5293, November 2019.

[205] S. Wabnitz and V. V. Kozlov. Harmonic and supercontinuum generation in quadratic and cubic nonlinear optical media. *JOSA B*, 27(9):1707–1711, September 2010.

[206] Fabio Baronio, Matteo Conforti, Costantino De Angelis, Daniele Modotto, Stefan Wabnitz, Marco Andreana, Alessandro Tonello, Philippe Leproux, and Vincent Couderc. Second and third order susceptibilities mixing for supercontinuum generation and shaping. *Optical Fiber Technology*, 18(5):283–289, September 2012.

[207] Daniel D. Hickstein, David R. Carlson, Abijith Kowligy, Matt Kirchner, Scott R. Domingue, Nima Nader, Henry Timmers, Alex Lind, Gabriel G. Ycas, Margaret M. Murnane, Henry C. Kapteyn, Scott B. Papp, and Scott A. Diddams. High-harmonic generation in periodically poled waveguides. *Optica*, 4(12):1538–1544, December 2017.

[208] Xiyuan Lu, Gregory Moille, Ashutosh Rao, Daron A. Westly, and Kartik Srinivasan. Efficient photoinduced second-harmonic generation in silicon nitride photonics. *Nature Photonics*, pages 1–6, November 2020.

[209] Edgars Nitiss, Jianqi Hu, Anton Stroganov, and Camille-Sophie Brès. Optically reconfigurable quasi-phase-matching in silicon nitride microresonators. *Nature Photonics*, 16(2):134–141, February 2022.

[210] P. V. Mamyshev and S. V. Chernikov. Ultrashort-pulse propagation in optical fibers. *Optics Letters*, 15(19):1076–1078, October 1990.

[211] Thomas Brabec and Ferenc Krausz. Nonlinear Optical Pulse Propagation in the Single-Cycle Regime. *Physical Review Letters*, 78(17):3282–3285, April 1997.

[212] M. Kolesik, J. V. Moloney, and M. Mlejnek. Unidirectional Optical Pulse Propagation Equation. *Physical Review Letters*, 89(28):283902, December 2002.

[213] M. Kolesik and J. V. Moloney. Nonlinear optical pulse propagation simulation: From Maxwell's to unidirectional equations. *Physical Review E*, 70(3):036604, September 2004.

[214] G. Genty, P. Kinsler, B. Kibler, and J. M. Dudley. Nonlinear envelope equation modeling of sub-cycle dynamics and harmonic generation in nonlinear waveguides. *Optics Express*, 15(9):5382–5387, April 2007.

[215] Matteo Conforti, Fabio Baronio, and Costantino De Angelis. Nonlinear envelope equation for broadband optical pulses in quadratic media. *Physical Review A*, 81(5):053841, May 2010.

[216] M. Conforti, F. Baronio, and C. De Angelis. Ultrabroadband Optical Phenomena in Quadratic Nonlinear Media. *IEEE Photonics Journal*, 2(4):600–610, August 2010.

[217] C. R. Phillips, Carsten Langrock, J. S. Pelc, M. M. Fejer, I. Hartl, and Martin E. Fermann. Supercontinuum generation in quasi-phasematched waveguides. *Optics Express*, 19(20):18754–18773, September 2011.

[218] Matteo Conforti, Andrea Marini, Truong X. Tran, Daniele Faccio, and Fabio Biancalana. Interaction between optical fields and their conjugates in nonlinear media. *Optics Express*, 21(25):31239, December 2013.

[219] Morten Bache. The Nonlinear Analytical Envelope Equation in quadratic nonlinear crystals. *arXiv:1603.00188 [physics]*, March 2016.

[220] Oliver Melchert and Ayhan Demircan. A python package for ultrashort optical pulse propagation in terms of forward models for the analytic signal, April 2021.

[221] pyNLO. pyNLO: Nonlinear optics modeling for Python, October 2022.

[222] K.J. Blow and D. Wood. Theoretical description of transient stimulated Raman scattering in optical fibers. *IEEE Journal of Quantum Electronics*, 25(12):2665–2673, December 1989.

[223] R. H. Stolen, J. P. Gordon, W. J. Tomlinson, and H. A. Haus. Raman response function of silica-core fibers. *JOSA B*, 6(6):1159–1166, June 1989.

[224] Steven A. Orszag. On the Elimination of Aliasing in Finite-Difference Schemes by Filtering High-Wavenumber Components. *Journal of the Atmospheric Sciences*, 28(6):1074–1074, September 1971.

[225] S. Derevyanko. The $(n+1)/2$ Rule for Dealiasing in the Split-Step Fourier Methods for n-Wave Interactions. *IEEE Photonics Technology Letters*, 20(23):1929–1931, December 2008.

[226] Johan Hult. A Fourth-Order Runge–Kutta in the Interaction Picture Method for Simulating Supercontinuum Generation in Optical Fibers. *Journal of Lightwave Technology*, 25(12):3770–3775, December 2007.

[227] O.V. Sinkin, R. Holzlohner, J. Zweck, and C.R. Menyuk. Optimization of the split-step Fourier method in modeling optical-fiber communications systems. *Journal of Lightwave Technology*, 21(1):61–68, January 2003.

[228] Alexander M. Heidt. Efficient Adaptive Step Size Method for the Simulation of Supercontinuum Generation in Optical Fibers. *Journal of Lightwave Technology*, 27(18):3984–3991, September 2009.

[229] Stéphane Balac and Arnaud Fernandez. Comparison of adaptive step-size control strategies for solving the Generalised Non-Linear Schrodinger Equation in optics by the Interaction Picture method. *HAL*, October 2012.

[230] J. R. Dormand and P. J. Prince. A family of embedded Runge-Kutta formulae. *Journal of Computational and Applied Mathematics*, 6(1):19–26, March 1980.

[231] https://github.com/pychi-code/pychi.

[232] Robert W. Boyd. *Nonlinear Optics, Third Edition*. Academic Press, Inc., USA, 3rd edition, 2008.

[233] Xinyi Ren, Ming Yan, Zhaoyang Wen, Hui Ma, Ran Li, Kun Huang, and Heping Zeng. Dual-comb quartz-enhanced photoacoustic spectroscopy. *Photoacoustics*, 28:100403, December 2022.

[234] Marta Ruiz-Llata, Yuliy M. Sanoyan, Oscar E. Bonilla-Manrique, Pablo Acedo, and Pedro Martín-Mateos. Dual-comb photoacoustic spectroscopy with electro-optic generation for the analysis of gaseous samples, February 2023.

[235] Xiaoxiang Gao, Xiangjun Chen, Hongjie Hu, Xinyu Wang, Wentong Yue, Jing Mu, Zhiyuan Lou, Ruiqi Zhang, Keren Shi, Xue Chen, Muyang Lin, Baiyan Qi, Sai Zhou, Chengchangfeng Lu, Yue Gu, Xinyi Yang, Hong Ding, Yangzhi Zhu, Hao Huang, Yuxiang Ma, Mohan Li, Aditya Mishra, Joseph Wang, and Sheng Xu. A photoacoustic patch for three-dimensional imaging of hemoglobin and core temperature. *Nature Communications*, 13(1):7757, December 2022.

[236] Xinyi Ren, Jin Pan, Ming Yan, Jiteng Sheng, Cheng Yang, Qiankun Zhang, Hui Ma, Zhaoyang Wen, Kun Huang, Haibin Wu, and Heping Zeng. Dual-comb optomechanical spectroscopy. *Nature Communications*, 14(1):5037, August 2023.

[237] Edoardo Vicentini, Zaijun Chen, Jeong Hyun Huh, Gianluca Galzerano, Theodor W. Hänsch, and Nathalie Picqué. High-Spectral-Resolution Imaging Spectroscopy with a Dual-Comb Interferometer. In *Frontiers in Optics / Laser Science (2020), paper LTu2F.3*, page LTu2F.3. Optica Publishing Group, September 2020.

[238] Peter Chang, Nazanin Hoghooghi, Scott Egbert, Sida Xing, Daniel Lesko, Alexander Lind, Gregory Rieker, and Scott Diddams. 1 GHz mid-infrared dual-comb spectrometer spanning more than 30 THz. In *Conference on*

Lasers and Electro-Optics (2022), Paper SF4O.4, page SF4O.4. Optica Publishing Group, May 2022.

[239] Markus Ludwig, Furkan Ayhan, Tobias M. Schmidt, Thibault Wildi, Thibault Voumard, Roman Blum, Zhichao Ye, Fuchuan Lei, François Wildi, Francesco Pepe, Mahmoud A. Gaafar, Ewelina Obrzud, Davide Grassani, François Moreau, Bruno Chazelas, Rico Sottile, Victor Torres-Company, Victor Brasch, Luis G. Villanueva, François Bouchy, and Tobias Herr. Ultraviolet astronomical spectrograph calibration with laser frequency combs from nanophotonic waveguides, June 2023.

[240] David Burghoff, Ningren Han, and Jae Ho Shin. Generalized method for the computational phase correction of arbitrary dual comb signals. *Optics Letters*, 44(12):2966–2969, June 2019.